

Single atom interferometers and Bloch oscillations in quantum walks

Dissertation

zur
Erlangung des Doktorgrades (Dr. rer. nat.)
der
Mathematisch-Naturwissenschaftlichen Fakultät
der
Rheinischen Friedrich-Wilhelms-Universität Bonn

vorgelegt von

Andreas Steffen

aus
Düren

Bonn 2012

Angefertigt mit Genehmigung
der Mathematisch-Naturwissenschaftlichen Fakultät
der Rheinischen Friedrich-Wilhelms-Universität Bonn

1. Gutachter: Prof. Dr. Dieter Meschede
2. Gutachter: Prof. Dr. Martin Weitz

Tag der Promotion: 19.04.2013

Erscheinungsjahr: 2013

Diese Dissertation ist auf dem Hochschulschriftenserver der ULB Bonn
http://hss.ulb.uni-bonn.de/diss_online elektronisch publiziert

Contents

1	Introduction	1
2	Experimental apparatus	3
2.1	Overview	3
2.1.1	Atom cooling and trapping	3
2.1.2	Experimental sequence	7
2.1.3	Digital atom operations	7
2.1.4	Atom imaging	9
2.2	Optical lattice	11
2.2.1	State-dependent shifting	11
2.2.2	Electro-optic modulator	13
2.2.3	Two-arm setup for quantum walks	13
2.2.4	Coherence in the lattice	19
2.3	Special alignment procedures	22
2.3.1	Aligning the EOM	22
2.3.2	Axial ground state cooling	26
2.3.3	Tuning transport parameters	27
2.3.4	Measuring vacuum window birefringence	29
3	Single Atom Interferometer	32
3.1	Theory	32
3.2	Measuring potential gradients	36
3.2.1	Phase detection and noise	36
3.2.2	Light shift gradient	40
3.2.3	External acceleration	44
3.3	Measuring contrast	47
3.3.1	Contrast decrease from shifting	47
3.3.2	Contrast decrease from separation	48
3.3.3	Data analysis	49
4	Quantum walks	53
4.1	Introduction	53
4.2	Theory	54
4.2.1	Spreading	54
4.2.2	Quantum walks in the Brillouin zone	56
4.2.3	Decoherence by projection	58
4.2.4	Dephasing and paths	60
4.2.5	Acceleration	61
4.3	Experiment	65
4.3.1	Procedure	65
4.3.2	Results from non-electric quantum walks	68

4.3.3 Results from electric quantum walks	74
4.4 Proposal for k -state selection	79
5 Conclusion	83

Summary

This thesis deals with the digital manipulation of the position and spin of neutral Caesium atoms in an optical lattice. I investigate coherent phenomena based on interferences between the trajectories of a single atom. Individual atoms are split by making use of our state-dependent lattice to shift different spin states in opposite directions, leading to coherent superpositions of spin and position state. This offers many possibilities; in this work, we chose to investigate atom interferometry and quantum walks in potential gradients.

Chapter 1 is a brief introduction to the importance of phase in quantum mechanics.

In chapter 2, I provide an introduction to our experimental apparatus with particular focus on state-dependent shifting and correct alignment procedures. Our model for decoherence in the lattice is also presented, with emphasis on the polarization state of the lattice lasers.

Chapter 3 presents the first of two measurement campaigns, which employs a single atom interferometer with a flexible geometry. We investigate a laser intensity gradient present in the system and demonstrate how several interferometer geometries can be compared to glean extra information about the symmetries of a potential gradient, such as its spin state dependence. A deliberately applied inertial force serves as a proof-of-principle for accelerometry and is correctly measured.

Chapter 4 contains the results of the second measurement campaign, which focussed on quantum walks. Quantum walks are a quantum analog to classical random walks and possess remarkable spreading properties. A theoretical model is presented, including a band structure picture of the walk. Unlike previous experiments, the walk can now be performed in a potential gradient, giving rise to new physics, in particular Bloch oscillations, which manifest as oscillations of the distribution width. Experimental results first confirm the predictions made by our model and show quantum walks of up to 100 steps with coherent behaviour. Walks in potential gradients are measured and indeed show clear signatures of Bloch oscillations. This is particularly remarkable because the quantum walk is effectively mimicking an electron in a solid, forming a basic quantum simulator.

Chapter 5 is a conclusion and a preview on ongoing technical improvements that stand to significantly extend the experimental capabilities.

Parts of this thesis have been published in the following papers:

- A. Steffen, A. Alberti, W. Alt, N. Belmehri, S. Hild, M. Karski, A. Widera and D. Meschede: "A digital atom interferometer with single particle control on a discretized spacetime geometry", *PNAS* **109**, 9770 (2012)
- Genske, Maximilian and Alt, Wolfgang and Steffen, Andreas and Werner, Albert H. and Werner, Reinhard F. and Meschede, Dieter and Alberti,

Andrea: "Electric Quantum Walks with Individual Atoms", *Phys. Rev. Lett.* **110**, pp. 190601 (2013)

Acknowledgements

I would like to acknowledge for their support in this work:

Dieter Meschede for his supervision, guidance on publications and tireless battle for funding.

Artur Widera and Andrea Alberti for close supervision, cooperation and setting of topics.

Wolfgang Alt for knowing "only very little" but always what helps.

My predecessors Michal and Leonid for introducing me to the experiment.

My colleagues for advice and motivational aid.

My family for support and interest.

My girlfriend for motivation, support and understanding that labs sometimes take longer.

1 Introduction

Quantum mechanics is a science of phase. Many of the best known quantum effects, such as entanglement, double slit phenomena or lasing are all phenomena arising from interplay between the phases of different quantum states. A good understanding and control of phase is therefore a major interest in current research and a necessity for the realization of quantum computers. The challenges are many, because phase is extremely volatile, reacting to any changes in the system or its environment.

Experiments can deal with phase differently depending on their goal. Precision experiments like atomic clocks [1] or atom interferometers [2, 3], are designed to maximize the phase's sensitivity to the targeted variable, so as to measure it more keenly, at the cost of high requirements for the control of external fluctuations. Quantum logic devices (e.g., [4]) go the opposite route and employ quantum states as digitized binary information. They do not require high phase sensitivity, but rather seek a robustness that allows high-fidelity operations between many involved qubits.

Most experiments operate in between, looking for a middle ground in the control of phase that suits their purpose. One growing category of experiments are quantum simulators [5], which aim to recreate a given Hamiltonian and observe the system's evolution, in order to study another more complicated system. A full simulator does not exist yet, but should be a multi-component system with tunable coupling between several qubits [6]. The phases between the qubits are the key component of the simulation and must evolve with reasonable accuracy and precision to mimic the simulated system. Many quantum phenomena that are candidates for simulation attempts revolve around the interchange of phase between qubits and collective effects. Our experiment is aimed to develop techniques that can benefit quantum simulation and precision measurement alike, researching operations on individual atoms and their effect on phase.

Quantum behaviour is studied in many different systems; ultracold atoms in optical traps are the most accessible and versatile one [7]. Their high degree of isolation from the environment combined with the many available schemes for controlling their state make them the workhorse of quantum technology research, as well as precision measurement. Our experiment focusses on the single atom scale: A handful of Caesium atoms is picked from an ultracold cloud and stored in a one-dimensional optical lattice, with no more than one atom per site. Unlike ensemble experiments with cold clouds or condensates, we intend to remove all multi-atom effects to gain access to purely single particle physics. In the future, controlled cold collisions [8] will allow us to reintroduce atom-atom interactions in order to study two- or three-atom effects with complete control over the atom number.

We have several tools available to manipulate and interrogate the atoms:

microwave radiation can be used to coherently control the hyperfine state of the atoms and fluorescence imaging allows detection of the atomic spin state and position in the lattice. Nonetheless, the pivotal tool for our experiment is the optical lattice. The two hyperfine states used each have a strongly selective coupling to one of the circular polarizations in the lattice laser. By displacing one chirality's lattice from the other one's, the hyperfine states can be coherently moved, separated and recombined. A high-speed optical modulator can shift the chiralities faster than the decoherence time in our setup, allowing coherent splitting and recombination of atoms. This permits a deterministic control of position.

The position of atoms is discretized by the optical lattice and we program the experimental sequence by combining a small number of primitive operations. The experiment is therefore digital in atom position and operation, and benefits from this in reproducability and flexibility.

The first set of experiments presented centers on atom interferometry: the spatial separation and recombination of one atom forms a microscale interferometer, whose phase can be read out by detecting the phase difference between the two parts of the atomic wavepacket. Highly sensitive experiments can be performed to measure the local shape of our optical trap, or an acceleration applied to the lattice. These experiments are described in detail in chapter 3.

A second set of experiments concentrates on quantum walks, which are quantum analogues of the classical random walk[9], and derive their properties from multi-path interference. Quantum walks can be reformulated as a particle in Bloch bands, forming a one-qubit quantum simulator for certain solid state systems (see chapter 4).

2 Experimental apparatus

2.1 Overview

2.1.1 Atom cooling and trapping

To perform quantum operations, we first need a controllable quantum system. Ultracold individual Caesium atoms gathered from a magneto-optical trap (MOT) are our system of choice. The setup I use to trap atoms and control their hyperfine state has been described in detail in the past [10, 11] and will be summarized briefly here.

The apparatus is centered around a glass cell containing Caesium vapour at ultra-high vacuum pressures. Experiments are performed inside an region of about $200 \mu\text{m}$ size, in which several optical paths intersect (see fig. 2.1):

- A MOT laser system of six beams for gathering the initial cold cloud
- An optical 1D lattice for confining and transporting the atoms
- Optical pumping beams for preparing all atoms in the hyperfine $|F = 4, m_F = 4\rangle$ state
- A microwave waveguide allowing irradiation with resonant microwaves for spin-state operation

MOT operation The MOT cloud is gathered by the cooling laser, which is frequency shifted close to the $|F = 4\rangle \rightarrow |F' = 5\rangle$ transition by an acousto-optic modulator (AOM). The laser light arrives from six directions at $200 \mu\text{W}$ per beam and a detuning of $2\text{-}3\Gamma$ and forms an optical molasses. A $3 \mu\text{W}$ repumper is added from the top and drives the $|F = 3\rangle \rightarrow |F' = 4\rangle$ transition to return atoms that have undergone an off-resonant $|F = 4\rangle \rightarrow |F' = 4\rangle$ transition and decayed to $|F = 3, m_F = 3\rangle$ to the main cooling cycle. Ramping down the molasses intensity to $60 \mu\text{W}$ per beam and increasing the detuning to 6Γ allows the atoms to settle into the optical lattice. The fluorescence they emit is imaged onto the EMCCD camera for atom counting and position detection (see 2.1.4). After imaging, another reduction in intensity and increase in detuning (to about 7Γ) is performed and the atoms irradiated for 10-20 ms to achieve further molasses cooling, with the cooling settings optimized to retain the largest fraction of atoms after a release-recapture temperature measurement [12].

The laser light arrives on the main table via three optical fibers coming from the laser table. These directly provide three of the six MOT beams; the remaining three are backreflections using mirrors. We tune the beams' convergence angle to reach a balanced intensity from both directions despite

optical losses on interfaces, which arise mostly from the uncoated inner wall of the glass cell. To enhance the homogeneity of the optical molasses, the back-reflection mirrors are mounted on piezo stacks that are modulated at incommensurate frequencies (300, 400, 550 Hz) to average out the interference patterns that would normally arise between the six beams. The MOT beams are also used for state-selective detection: when the beam from the top is activated without back-reflection for 150 μ s at very low detuning, it removes all atoms in the $|F = 4, m_F = 4\rangle$ state from the lattice.

The magnetic field gradient for the MOT is generated with a set of coils in anti-Helmholtz configuration and normally 10-20 G/cm. Another set of six coils is mounted in a 3D-Helmholtz configuration for the application of an homogeneous background field. This can be used to move the MOT into best overlap with the optical lattice for loading, but also to cancel external magnetic fields for quantum operations.

Optical lattice The attractive optical lattice is formed by light from a Titanium:Sapphire laser (Coherent MBR-110, Ti:Sa in the following), whose beam passes through the vacuum chamber and is then back-reflected. It is actively power-stabilized with a proportional-integral servo circuit acting on the laser power via an acousto-optic modulator. The circuit can achieve powers between 300 μ W and 200 mW in closed-loop. The reduction in power from the 2-3 W Ti:Sa output is mostly due to fiber coupling. At the atoms, this power is focussed to a beam waist of about 60 μ m diameter, creating a trap with up to 60 MHz depth (or 30,000 recoil energies E_R). Imaging is performed at 10 MHz (5000 E_R) depth, equal to 120 mW of power and quantum operations normally proceed at 1.6 MHz (800 E_R) depth, or 20 mW of power. At the latter depth, trap frequencies are 120 kHz along the lattice axis and about 1 kHz radial to it.

As mentioned in the introduction, the principal feature of the trap is its ability to perform state-dependent transport by shifting atoms left or right depending on their qubit state. As the key operation of our experiment, state-dependent transport will be elaborated further in 2.2.1. In the transition to the two-arm setup (see 2.2.3), some of the numbers given above changed: the beam waist shrank to 36 μ m diameter and the power for quantum operations was reduced to 6 mW, while the imaging power was changed to 30 mW, resulting in trap depths of 1.3 MHz for quantum operations and 7.5 MHz for imaging.

Optical pumping The two optical pumping beams initialize atoms in the $|F = 4, m_F = 4\rangle$ hyperfine state. One beam comes from the MOT cooling laser locked to the $|F = 4\rangle \rightarrow |F' = 4\rangle$ transition (and is not frequency-shifted by an AOM, unlike the optical molasses), while the other comes from the repumping laser. Both beams impinge on the atoms in high-quality circular polarization to drive only σ_+ transitions. We achieve optical pumping to the target state for at least 98% of the atoms by carefully ensuring correct polarization. Back-reflection of the optical pumping beam from the lattice back-reflection mirror must be prevented lest it drive σ_- transitions; to this end, we align

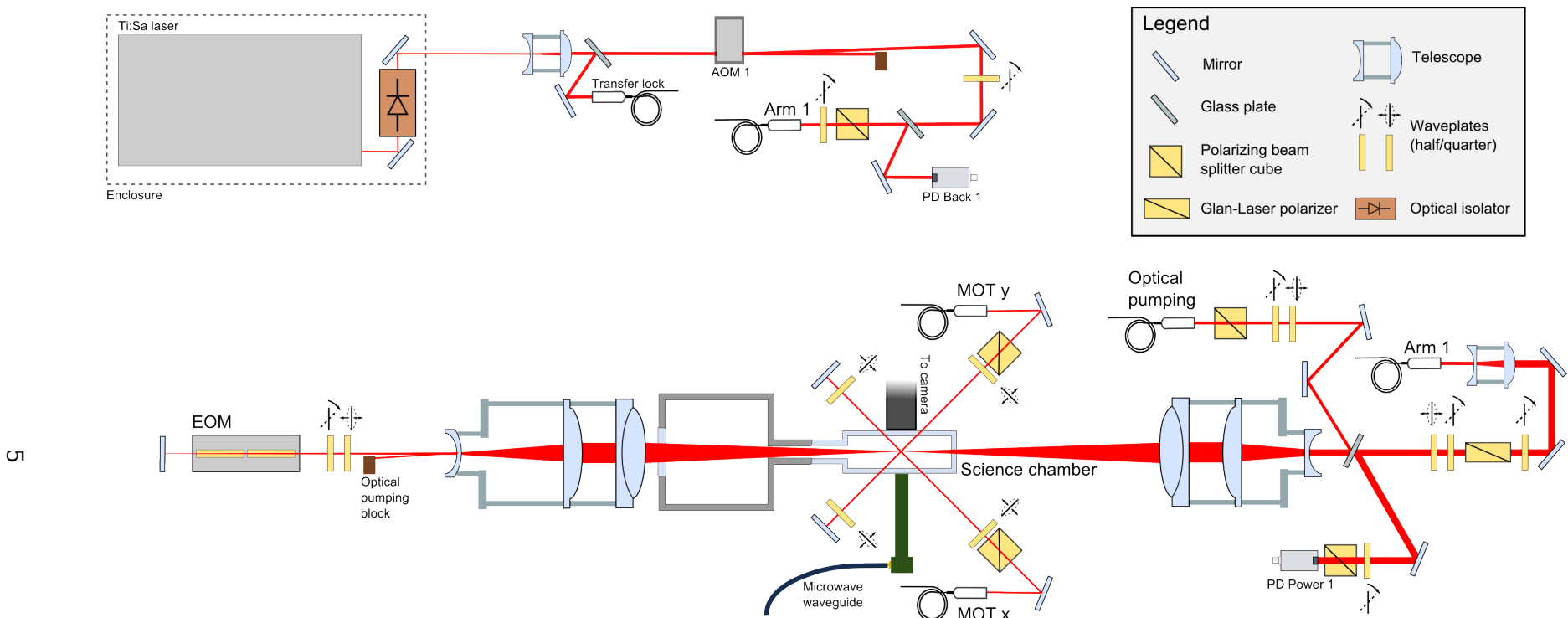


Figure 2.1: Schematic of the setup with back-reflected dipole trap as for atom interferometer measurements. Six MOT laser beams cross with circular polarization to create the optical molasses. The lattice laser is produced by the Ti:Sa laser in the top-left and coupled into a fiber through an AOM. The beam coming from the other fiber end is focussed onto the atoms and back-reflected after passing through the EOM to create the standing wave. The two photodiodes shown are for power stabilization and mode matching of the backcoupled beam. A fraction of the laser light goes to a transfer cavity for indirect locking to an atomic resonance. The first duo of waveplates in the lattice laser serves to compensate birefringences in the vacuum windows; the second duo has the function of translating between circular basis and a linear basis matched to the EOM crystal axes. An optical pumping prepares the initial spin state 4,4, but is not back-reflected. Microwave waveguide and camera objective are also indicated. Not shown is the magnetic coil system.

the optical pumping at an angle to the lattice and place a beam blocker behind the vacuum cell. In the latter two-arm setup, the optical pumping beam can simply be aligned colinear with the lattice. During microwave sideband cooling (see 2.3.2), the repumper serves as part of the cooling cycle, and its intensity must be low to prevent excessive heating [11]. Standard powers are 30 nW (cooler) and 10 nW (repumper).

Microwaves Resonant microwaves are the dominant method for qubit operations in this work, due to their low maintenance requirements and ease of use. The microwaves are directed to the atoms by a metallic waveguide ending close to the vacuum cell, so that the atoms are about one wavelength away from the outlet. They are generated by a setup consisting of two vector generators to produce a 160 MHz radio-frequency (RF) signal, a 9.04 GHz local oscillator, a mixer, a PIN diode attenuator and a power amplifier [10]. The vector generators output an initial signal that can be phase or frequency modulated and precisely pulsed. Because each generator can only be configured to modulate phase *or* frequency, we have two and a signal combiner to have both capabilities available at the same time. The mixer combines the generator output with the 9.04 GHz signal, resulting in the final frequency around 9.2 GHz, which matches the Zeeman-shifted qubit transition. A PIN diode provides variable attenuation and envelope-shaping for e.g., gaussian pulses, and the final amplifier can lift the signal power to 41 dBm. The actual power of microwaves at the atoms is uncertain due to standing waves inside the metallic structures surrounding the glass cell, but the maximum Rabi frequency reachable on the $|F = 4, m_F = 4\rangle$ to $|F = 3, m_F = 3\rangle$ qubit transition is 60 kHz [10]. Our normal operations occur at 50 kHz because the PIN diode is more reliable away from minimum attenuation.

For coherent operations, the compensation coils mentioned before are used to apply a 3 G quantization field parallel to the lattice axis in order to split the m_F manifold and shift the transitions between the levels to individually addressable frequencies. The other two field directions are set to the null value, which is determined experimentally by minimizing the Zeeman splitting - this procedure also cancels external fields. We can then consider the hyperfine states $|F = 4, m_F = 4\rangle$ and $|F = 3, m_F = 3\rangle$ sufficiently separated from the remaining manifold to treat them as a two-level pseudo-spin one-half system, with $|\uparrow\rangle = |F = 4, m_F = 4\rangle$ and $|\downarrow\rangle = |F = 3, m_F = 3\rangle$. Microwaves can drive transitions of the two-level system if they are resonant with the level splitting. The polarization of the microwave field emitted from the waveguide is linear and can thus be rotated along with the waveguide be set orthogonal to the quantization field (driving σ^+ and σ^- transition) or parallel to it (driving π transitions). We select the orthogonal polarization case to make the transition between our two qubit states available.

By controlling the duration, power and phase of the microwave pulse irradiating the atoms, a class of coherent rotations can be performed on the two-level system:

$$\hat{C}_{\theta,\phi} = \frac{1}{\sqrt{2}} \begin{pmatrix} \cos(\theta/2) & i \sin(\theta/2)e^{i\phi} \\ i \sin(\theta/2)e^{-i\phi} & \cos(\theta/2) \end{pmatrix}. \quad (2.1)$$

This is the general operator involving the microwave phase ϕ and the microwave rotation angle θ ; missing for a fully general rotation is the ability to rotate around the z-axis of the Bloch sphere. The primary uses of microwave pulses use $\theta \in \{\pi/2, \pi\}$. The $\pi/2$ pulse creates superpositions from pure states and the other way around, while the π pulse can exchange the spin state of a pure state or implement spin echo (see 2.2.4) on a superposition. These microwaves are our main tool to create and analyze coherent phenomena.

2.1.2 Experimental sequence

All experiments I describe in this thesis follow a common sequence; at the core of it lies a brief time span used for coherent operations that are described in 2.1.3. The surrounding experimental steps take up the bulk of the sequence time and provide cold atoms, state preparation and detection.

Any experiment begins by loading a MOT cloud, then compacting it by raising the gradient and shifting molasses parameters to make the atoms drop into the optical lattice. As the lattice is conservative, the molasses must cool the atoms into the lattice. The magnetic field gradient is deactivated and atoms are imaged in a strong lattice. This first image establishes the total number of atoms and, if desired, their position in the lattice. Additional molasses cooling is performed afterwards to decrease atom temperature further; then, a quantization field is ramped up to separate the two qubit states from the rest of the manifold and the lattice depth is decreased to reduce light shift-induced decoherence (see 2.2.4). The atoms are pumped to the $|F = 4, m_F = 4\rangle$ state using the resonant optical pumping beams for 20 ms.

The window for coherent operations begins once the optical pumping beam is fully shuttered off; otherwise, the optical pumping light will re-initialize the state populations during the coherent sequence. The windows' length is given by coherence times and the desired operations, but is rarely longer than 2 ms. Afterwards, the push-out beam may be activated to remove all atoms in $|F = 4, m_F = 4\rangle$ state from the lattice for state population detection. The lattice depth is increased to the original value and a second image is taken. For state population detection, the number of atoms before and after the sequence are compared. For position detection, no push-out is used, but the relative distance between atoms in the two pictures is extracted to show movement. Position detection is only reliable if the signal-to-noise ratio of the image is improved by raising exposure time above 600 ms, and if the atoms do not cluster too much (two neighboring atoms are all right, more decrease the reliability). Details on these experimental steps can be found in [10].

2.1.3 Digital atom operations

The word digital usually refers to the quantization of a time series in value or time. Because of the standardization of the input/output, digital circuits are more robust and can be more easily combined and altered. They are also naturally suited to implement logical operations and decisions. More

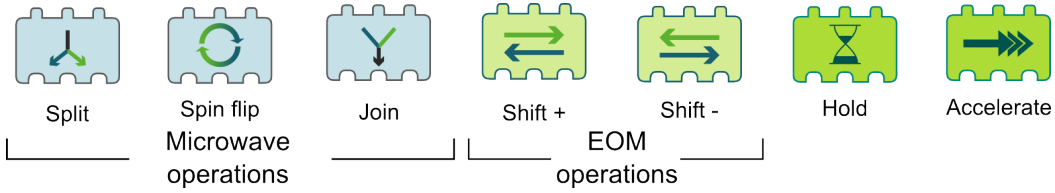


Figure 2.2: The available primitive operations. All coherence experiments in this thesis are composed by chaining these basic instructions together.

complex digital processors operate by executing a programmed sequence of primitive operations, drawn from the instruction set of the chip.

Our experiments are digital because our sequences are composed of primitive operations, and also because the operations we perform are quantized in time and value. When we perform an experiment, we are executing a "program" composed from only six different operations (see fig. 2.2). These operations can be aligned and calibrated separately and the final sequence can be put together and adapted at will.

Our sequences are digitized in time: each operation always takes the same amount of time and operates with the same parameters. Furthermore, the lattice traps the atoms at spacings of $\lambda/2$ and our shift operations translate atoms to the next lattice site, digitizing space. The spin state of the atoms is used as an analog space in our experiment.

The general advantages of digitization are a reduction in implementation complexity and an increase in robustness and flexibility. We profit the most from having a set of primitive operations available that can be freely chained together to perform different experiments on the atoms. Our alignment procedure concentrates on improving the performance of the individual blocks; whether the intended sequence is an interferometer or a quantum walk is unimportant, the required adaptations for this are merely how many atoms to load and how to image them. Underneath is a listing of the operations used in the coherent measurements of this thesis.

Split: A microwave $\pi/2$ pulse creates a superposition of spin states from a pure state:

$$|\uparrow\rangle \rightarrow \frac{1}{\sqrt{2}}(|\uparrow\rangle + |\downarrow\rangle).$$

This splits one quantum trajectory into two.

Join: A microwave $\pi/2$ pulse of variable phase ϕ_{MW} maps the phase of a superposition to the two pure state populations:

$$\frac{1}{\sqrt{2}}(|\uparrow\rangle + e^{i\phi}|\downarrow\rangle) \rightarrow a(\phi_{\text{MW}} - \phi)|\uparrow\rangle + b(\phi_{\text{MW}} - \phi)|\downarrow\rangle.$$

This joins two quantum trajectories and prepares the phase between them for readout using state detection.

Spin flip: A microwave π pulse inverts the qubit state:

$$|\uparrow\rangle \rightarrow |\downarrow\rangle.$$

This is essential for state-dependent shifts over more than one lattice site. It is also used in spin echoes to reduce dephasing.

Shift: The atoms are coherently shifted in position by $\pm\lambda/4$ depending on their spin state, e.g., turning a superposition of spin states into a superposition of spin and position state (see 2.2.1):

$$\frac{1}{\sqrt{2}}(|\uparrow, x\rangle + |\downarrow, x\rangle) \rightarrow \frac{1}{\sqrt{2}}(|\uparrow, x+1\rangle + |\downarrow, x-1\rangle).$$

Due to technical limitations, the sign of shifts must alternate.

Hold: This block is a time delay, allowing the state to evolve naturally. Normally this means accumulating phase, e.g., from external forces. A delay is worth mentioning because experiments with atoms in free fall cannot implement it. The main benefit lies in keeping the atom stationary at a location of interest.

Acceleration: Acceleration causes a linear, state-independent potential gradient. The phase accumulated is thus proportional to the distance between two states:

$$\frac{1}{\sqrt{2}}(|x\rangle + |x+n\rangle) \rightarrow \frac{1}{\sqrt{2}}(|x\rangle + e^{in\phi} |x+n\rangle).$$

Different means of creating acceleration are applied in this thesis, namely moving the back-reflection mirror in the one-arm lattice setup and using an optical conveyor belt technique(see 2.2.3). These blocks can be stacked as desired, except that the sign of the shifts must alternate. The majority of sequences for coherent measurement begin with a split to create multiple quantum paths and conclude within the coherence time.

2.1.4 Atom imaging

Detection is carried out by fluorescence imaging of the atoms using an EM-CCD camera (Andor iXon DV-887CS-FI) which uses a cooled CCD chip with an electron-multiplying amplification register. Low-light imaging is enhanced both by cooling the chip to reduce thermal excitations and by using an avalanche effect in the EM register to increase the number of signal electrons before analog-to-digital conversion. The camera performance allows for counting atoms and detecting their position with single lattice site precision, provided the atoms are not packed too densely. Fluorescence is induced using the MOT's optical molasses while the atoms are trapped in the lattice. The emitted light is collected by an in-house developed objective system [13] that images the optical lattice from the side onto the camera chip with a magnification of x55.

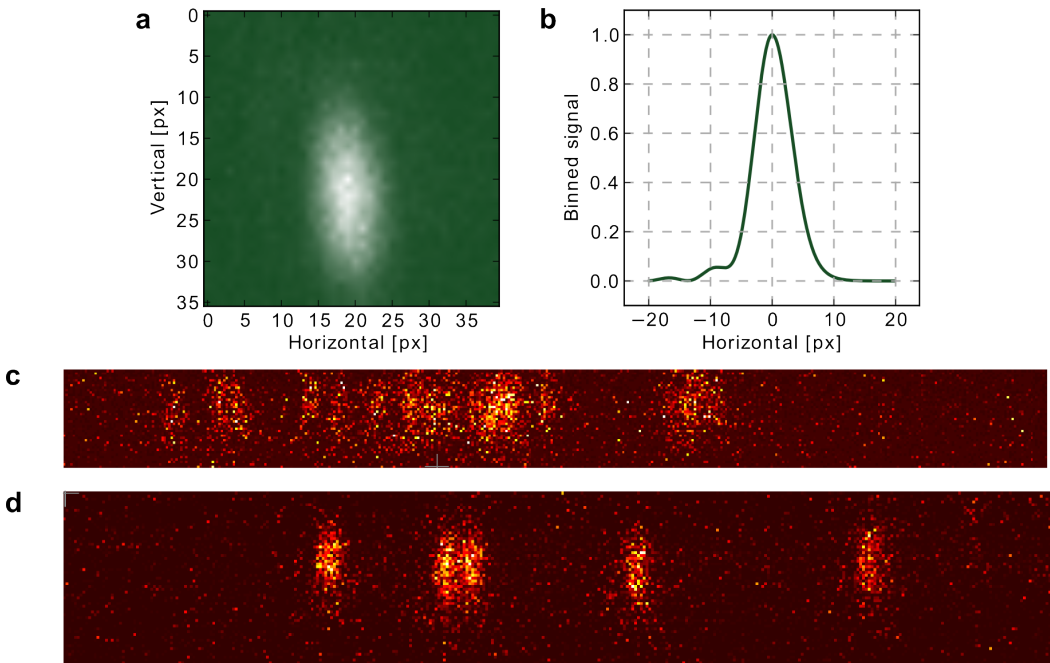


Figure 2.3: **a** Appearance of a single atom in our lattice, achieved by averaging many long-exposure pictures of single atoms. The shape is almost a 2D gaussian function. **b** Analytical line spread function of our optics for vertical binning, determined from the same data set by fitting with a model[10]. The asymmetric shoulder indicates slight coma aberration. **c** Example image from interferometry measurements: we image many atoms with a comparatively short and thus noisy exposure to gain high data rate. Miscounts can occur, but the benefit of averaging over many atoms outweighs them. **d** Example image from quantum walks: position detection is a must, so long exposures with isolated atoms are preferred. The image height is wider to avoid clipping if the lattice position drifts a little.

Stray light is reduced in several ways: a narrow-band interference filter (initially 82% transmission, replaced with Semrock filter of 95% transmission during electric walks measurements) suppresses light from the lattice laser, and apertures placed in the objective tunnel implement spatial filtering to block stray light from the MOT beams.

The recorded images are binned perpendicular to the lattice to produce 1D data traces. Our software looks for continuous regions above a noise threshold and marks them as regions of interest. The number of atoms therein is calculated by summing the counts above the baseline and dividing by a manually determined value for the counts per atom, usually about 60,000/s (CCD chip @ -70°) to 110,000/s (CCD chip @ -80°). Brief exposures (200-400 ms) experience counting errors due to the fluorescence noise as well as the spatially-varying sensitivity of the camera chip. Longer exposure can reduce this, but not eliminate it, particularly for large clusters of atom, partly due to photon shot noise and partly due to signal-proportional technical noise [10]. For state detection without position information, fast

images with many atoms deliver a much higher data rate, leading to a higher overall precision.

Position detection is a separate algorithm from counting [10], performed on high-quality images with 600 ms to 1 s exposure. The algorithm has knowledge of the imaging system's line-spread function (LSF), which is characterized to sub-pixel accuracy by overlapping many one-atom images (see fig. 2.3). Each atom appears as a Gaussian spot with 8 px horizontal standard deviation and 20 px vertical standard deviation, with an asymmetric feature on the shoulder indicating a slight comatic aberration. The algorithm applies a trigonometric moments method [14] to find the starting conditions for a least-squares fit, which is then executed by the standard Levenberg-Marquardt method [15]. The relative movement of atoms between two pictures can be calculated from the before/after positions; if two atoms could have crossed paths and thus their movements cannot be individually identified, both are excluded.

I have investigated the relation between photons and EMCCD signal in more detail. A photon impacting a pixel has a 40% chance of creating a photoelectron (quantum efficiency at 852 nm), which is then sent through the electron-multiplying register of 536 steps, each of which has a certain chance to create additional electrons. The manufacturer lists the total gain of the register as about 4000 at -80°C [16], resulting in a chance per step of 1.5% per input electron (note that EM gain is highly temperature dependent). At last, the EM-amplified signal is digitized in an ADC with a specified ratio of 60 electrons per count. The numbers above combine to give a relation of 67 CCD counts per photoelectron. An independent analysis performed based on the shotnoise scaling with signal intensity results in about 60 counts per photoelectron[17].

The ADC also has 98 counts offset and about 10 counts standard deviation in noise, which is why the CCD signal should be amplified before digitization. Inverting the previous calculation and taking the objective's solid angle (numerical aperture 0.29) into account, we find that each atom seems to scatter about 5000 photons per second in total, a third of the scattering rate in saturation. The result is credible seeing that we are not illuminating at the maximum power to avoid heating; also, most atom experiments stay a factor two or so below the theoretical photon number. Taking our optical spreading into account , this leads to a maximum of 70 photons per second on the brightest pixel.

Our detection has also been further analyzed in the thesis of Jonathan Zopes[18].

2.2 Optical lattice

2.2.1 State-dependent shifting

The heartpiece of our experiment is the wavelength and polarization of the optical lattice that allows selectively trapping states in light driving σ^\pm transitions. At the magical wavelength of 865.9 nm, the $|F = 4, m_F = 4\rangle$ state is

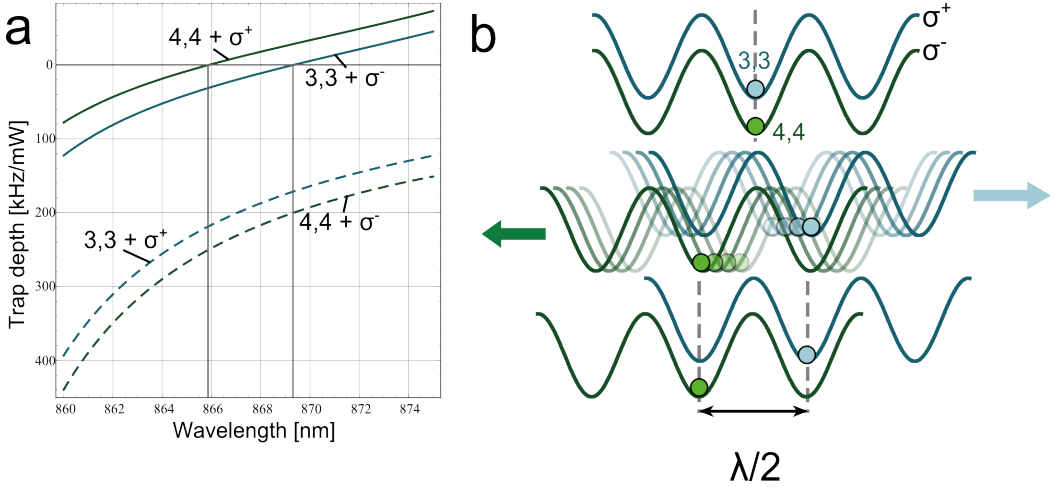


Figure 2.4: **a** Plot showing the calculated dipole trap coupling between the two qubit states and circular polarized light. Lines mark the two possible magic wavelengths that completely eliminate one of the couplings. We have selected 865.9 nm to zero one of the couplings for $|F = 4, m_F = 4\rangle$. **b** Schematic of the state-dependent shifting. The two chiral sublattices are precisely overlapped and trap their respective spin state. Ramping the phase between the chiralities shifts the lattices apart until they again overlap after each has travelled $\lambda/4$. The $|F = 3, m_F = 3\rangle$ state feels the other lattice slightly, making its trap depth change during shifting.

trapped exclusively by light driving a σ^- transition, whereas the $|F = 3, m_F = 3\rangle$ state is trapped seven times more by σ^+ transitions than by σ^- [10]. The non-trapping polarizations have in common that they create repulsive coupling to the D1 line and attractive coupling to the D2 line. The influence of these two couplings cancels at a certain wavelength between the two lines, as shown in fig. 2.4a (full calculation see [19]).

For the quantization axis parallel to the lattice axis, the required σ transitions are driven by left- and right-hand circularly polarized light. The overall lattice is a lin- ϑ -lin configuration composed of two beams of linear polarization at a variable angle ϑ . This is equivalent to $\odot -\varphi - \odot$, which signifies two standing waves of circular polarization that are phase-shifted from each other by a phase $\varphi = 2\vartheta$. Each qubit state is trapped in one of the two standing waves and moves if φ is varied (see fig. 2.4b). Most importantly, a coherent superposition of both qubit states can be spatially separated and recombined. The $|F = 3, m_F = 3\rangle$ state experiences a modulation of its well depth as a result of the $1/8$ coupling to the other chirality:

$$U_0^{|3,3\rangle}(\varphi) = \frac{7}{8}U_0 + \frac{1}{8}U_0 \cos \varphi. \quad (2.2)$$

. For the same reason, the position of the potential minimum for the $|F = 3, m_F = 3\rangle$ state position is not evolving in a completely linear manner vs. φ (see [10] ch. 4 for details), but this is much less important.

2.2.2 Electro-optic modulator

We vary the phase between the chiralities φ using an electro-optic modulator (EOM) in one of the lattice beams.

Electro-optic modulators are crystal devices based on the Pockels effect that are normally used to produce switchable birefringence, e.g., for q-switching or intensity modulation. The laser beam passes through a crystal subjected to a homogeneous electric field. Our experiment contains EOMs holding two KD*P crystals (deuterated potassium dihydrogen phosphate) from Conoptics Inc. (models 350-80BK for one-arm lattice and 350-105BK for two-arm), in which the field is applied in transversal direction by a high-voltage driver (Conoptics 302 RM) (see fig. 2.5a,b). The two rectangular crystals are mounted at 90° rotation to cancel the natural birefringence of KD*P and provide a birefringence that is linearly dependent on the applied voltage. It is vital for the cancellation that the crystals be of equal length, so they are polished side-by-side. The crystals are placed between electrodes, glued into a groove in brass (see fig. 2.5c) and mounted inside an aluminum cylinder filled with a liquid that serves to reduce reflections from the crystal end faces and prevents water from reaching the hygroscopic crystals.

The EOM is used as a voltage-variable birefringence, i.e. a phase shifter in linear basis. A subsequent $\lambda/4$ plate converts linear phase shift into a circular basis phase shift (see fig. 2.5d). State-dependent shifting by one lattice site occurs when the control voltage is ramped from 0 to the voltage $V_{2\pi}$, which is defined as the voltage that causes the EOM to produce a phase shift of 2π between the chiralities. At this phase shift, the two chiral sublattices are again fully overlapped, albeit with each atom displaced by half a site. To transport atoms multiple sites, one cannot simply drive the EOM to $2 \cdot V_{2\pi}$, due to voltage limitations. Instead, a microwave π pulse can switch the qubit state while the EOM remains at $V_{2\pi}$, and the atom continues its movement in the original direction when the EOM is ramped back to zero voltage.

The driver applies about 770 V to both electrodes of a crystal and the polarization is modulated by increasing one voltage and decreasing the other, up to a maximum difference of 750 V. The voltage can be modulated with a bandwidth of 200 kHz, presumably limited by the capacitative load of EOM and cables.

Temperature can affect the value of $V_{2\pi}$, as the Pockels coefficient decreases for higher temperatures by 1.4% per degree[20]. We have found it necessary to actively stabilize the temperature, not only because of the Pockels coefficient but also because of mechanical drifts that affect the polarization even when no voltage is applied. The optical alignment procedure for the EOM is discussed in 2.3.1.

2.2.3 Two-arm setup for quantum walks

The quantum walks measurements of chapter 4 depend on being able to accelerate the atoms using an optical conveyor belt technique [21, 22]. This method uses a lattice composed of two counter-propagating laser beams

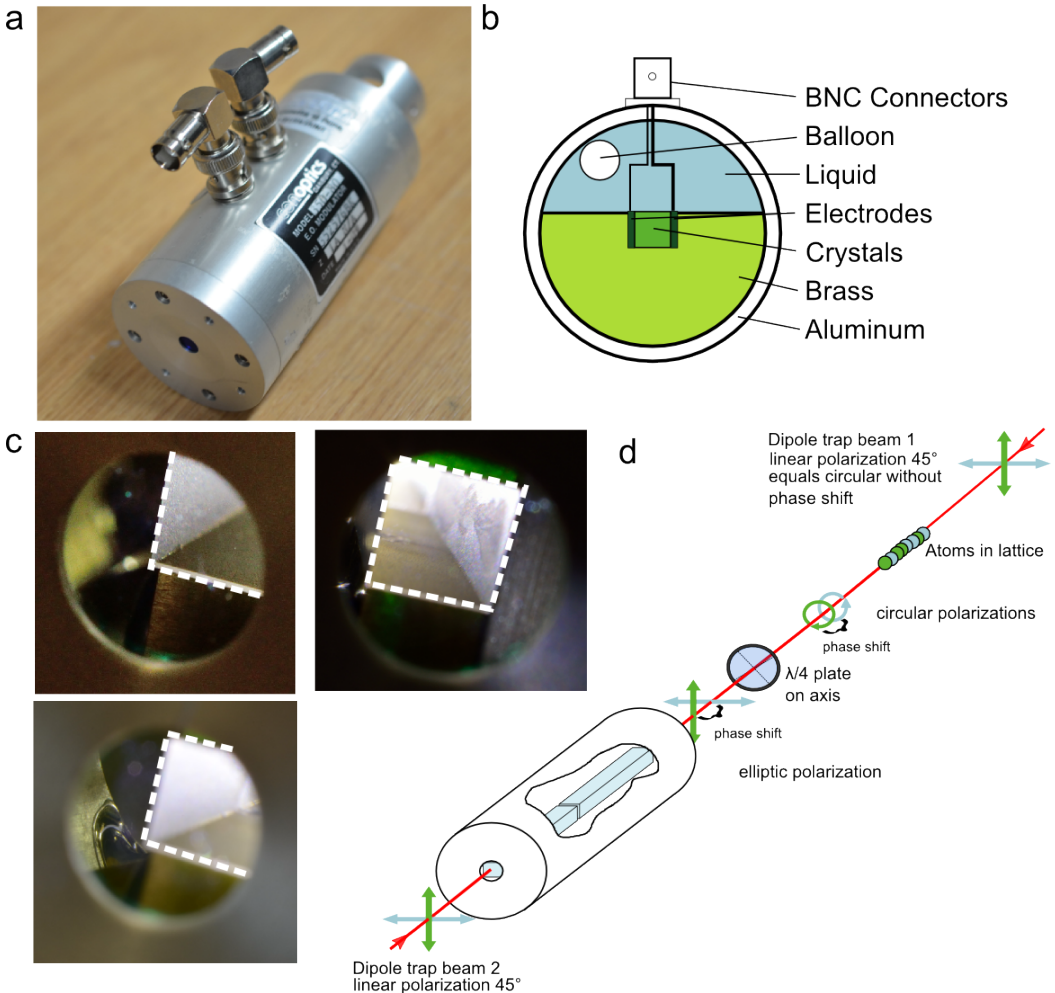


Figure 2.5: **a** Photograph of the EOM for atom interferometry. **b** Speculated inner construction. The liquid is filled in to reduce reflection from the crystals (albeit not fully index-matched) as well as to prevent water from entering the hygroscopic KD*P. The balloon absorbs pressure changes from thermal expansion [20]. **c** Close-up angled photographs through the entrance hole, showing the sides of the crystal, the BNC connector in the background and glue traces on the side. The crystal is marked in white to guide the eye. **d** Realizing the phase between the chiralities via EOM, here shown for the two-arm setup (see 2.2.3). A beam with linear polarization is oriented such that it evenly fills both eigenpolarizations of the EOM. Applying a voltage results in phase shift between the eigenpolarizations, producing an overall elliptic polarization for $V \neq 0$. Afterwards, a $\lambda/4$ plate transforms both components into circular polarization. The circular components interfere with the counter-propagating arm, which is linearly polarized. For alignment, the EOM is set to $V = 0$. The linear polarization exiting the EOM then must be matched to the axis of the $\lambda/4$ plate and to the counter-propagating laser's linear polarization. This is done using additional waveplates (not shown here, but visible in fig. 2.6).

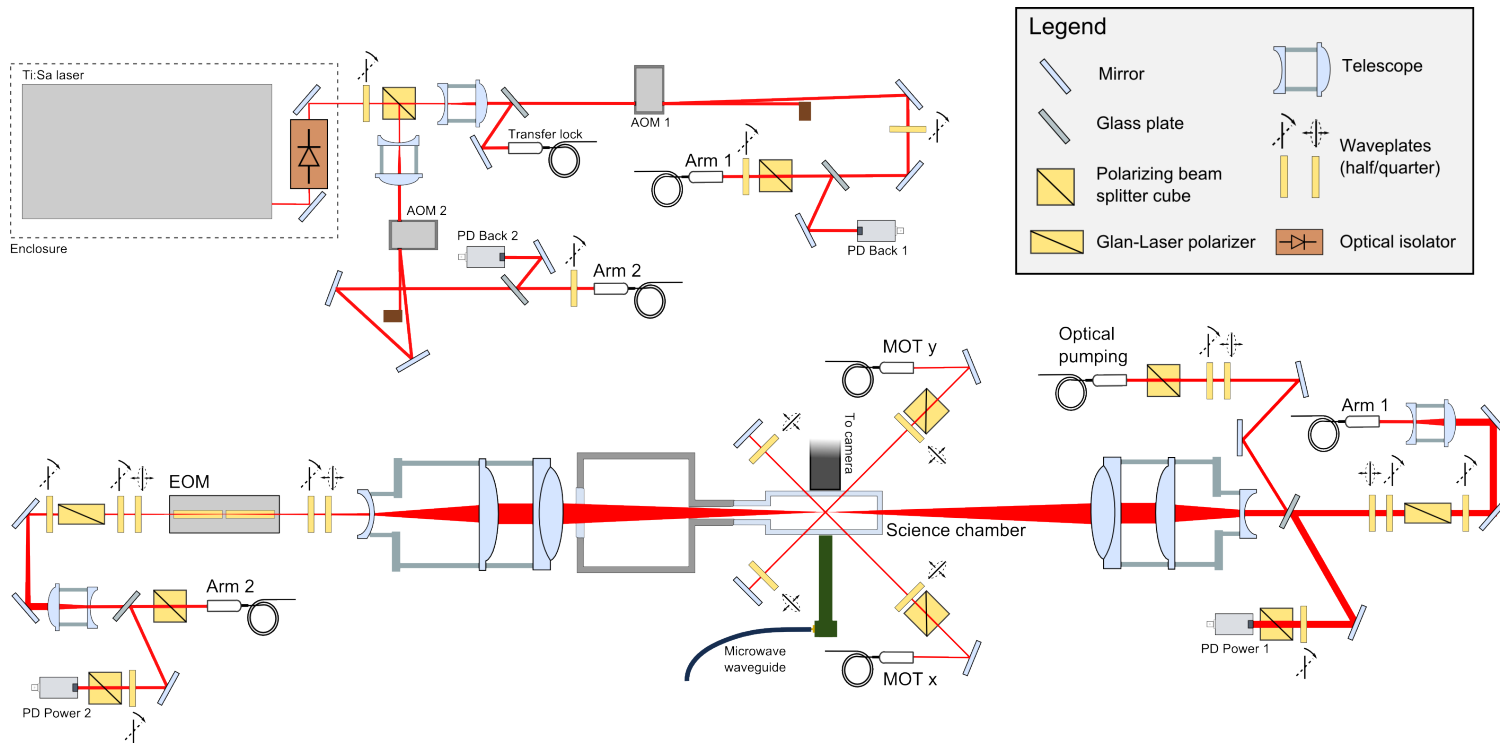


Figure 2.6: Schematic of the two-arm setup. The back-reflection mirror left of the EOM is removed and the newly introduced second arm mode-matched to the first. Additional fibercoupling, power stabilization and polarization control have become necessary. The optical pumping beam no longer needs to be blocked and can be co-propagating with the lattice beam.

of frequencies f_1, f_2 that can be detuned with respect to each other by Δf , leading to a lattice moving with a detuning-dependent velocity. How quickly the atoms move as a result can be understood by considering that if the atom moves towards the beam with the smaller frequency at the right speed, the Doppler shift modifies the frequency of both beams so that the atom no longer perceives any detuning. In the moving reference frame, the lattice does not appear detuned and is at rest, which occurs at $v = \Delta f \cdot \lambda/2$.

To provide the two beams with different frequencies, the back-reflection mirror is removed and the Ti:Sa laser output is split 50:50. The split-off light is coupled into a new optical fiber and power-stabilized, with the setup for these tasks copied from the original lattice. The beam exiting the new fiber is overlapped onto the atoms and mode matched to the first arm, reaching up to 85% cross-coupling of power from one arm through the fiber of the other. The EOM's phase-shifting power is halved by the conversion from double to single pass and a new model with longer crystals (Conoptics 350-105BK) is installed to reach the required 2π . The switch from back-reflection to two independent beams can allow lattice phase noise to increase due to the two independent RF sources used; heterodyne measurements with a Michelson interferometer and a fast photodiode show that the noise is well within the tolerance [22].

In the course of these modifications, the telescopes focussing the lattice beams right after the fiber couplers were improved by using lenses with longer focal length and re-centering the beam on the lenses. The waist radius on the atoms was thereby decreased to $18 \mu\text{m}$, from $30 \mu\text{m}$ previously. To reduce polarization inhomogeneity, we minimize the beam radius in the EOM by moving the telescope next to the second arm fiber coupler to move its focus into the EOM. This reduces the beam radius in the EOM to $280 \mu\text{m}$, but also shifts the focus in the vacuum away from the atoms, increasing the beam radius at the atoms by a factor of 1.4. It also reduces fiber cross-coupling to about 60% because the first arm is not mode-matched fully anymore.

DDS setup

In addition to two independent laser beams, atom acceleration in a conveyor belt requires detuning the two beams from each other. We achieve this by using a flexible digital RF source to drive the two AOMs that control the frequency and power of the two lattice beams (see fig. 2.6). The source is a DDS (direct digital synthesis) device with two RF outputs, namely an Analog Devices AD9954 evaluation board, containing two AD9954 chips.

Direct digital synthesis generates a sine wave based on the principle $f = \int \phi dt = \sum_i \Delta\phi$: the device contains a 32-bit phase buffer that is incremented every clock cycle by a certain value $\Delta\phi$. The current value of the phase buffer is then used to create an output voltage corresponding to a sine wave of that phase via a lookup table and a digital-to-analog convert unit (DAC). The output frequency depends on the phase increment $\Delta\phi$; if it is $2^{32}/100$, the DDS will output a hundredth of its clock frequency.

The device's reliability and noise performance is very good as long as it is

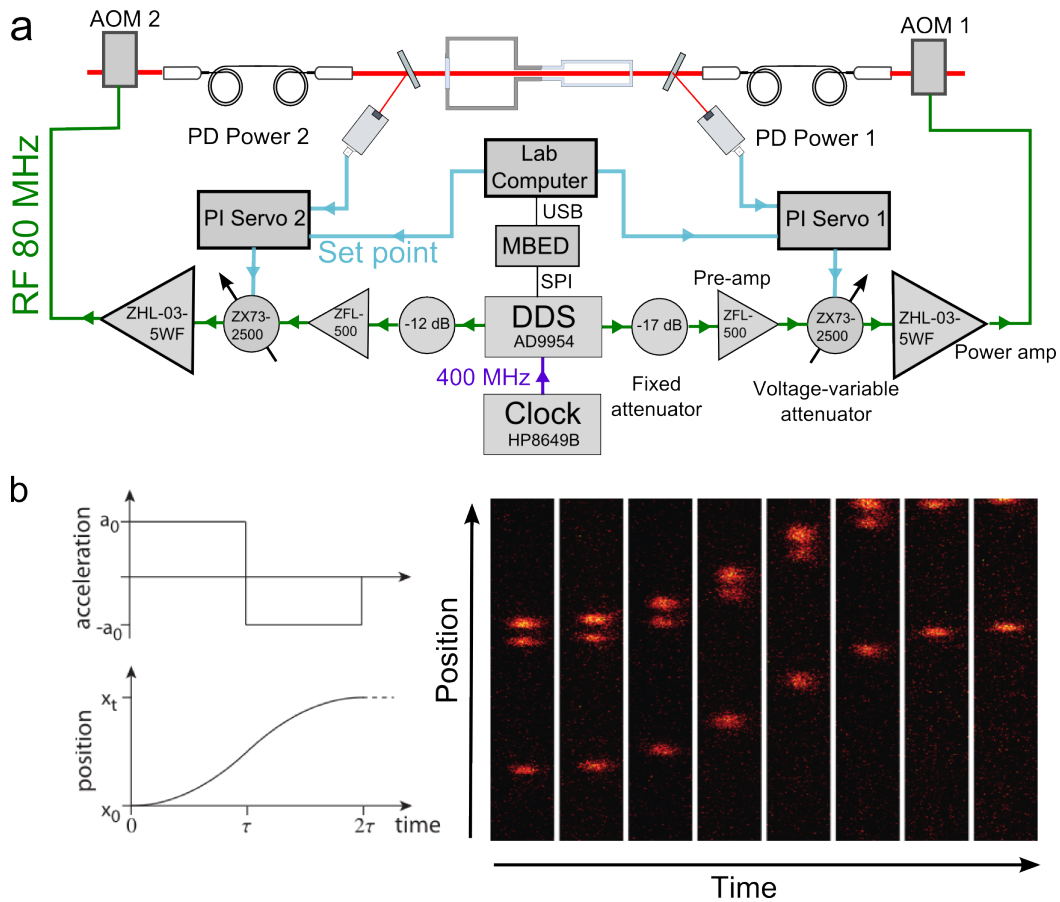


Figure 2.7: **a** Schematic of the RF setup for acceleration and the connected components in the optical setup. The DDS provides two phase- and frequency-tunable 80 MHz signals, which are amplified and fed to the AOMs. To produce sufficient final power without harming any components, the DDS output signals are amplified, but with some attenuation (-12 or -17 dB are both workable). Two PI servos control the amplitude of the signal with variable attenuators to stabilize the laser power. The error signal for this control action is the difference between the photodiode voltage and a setpoint voltage coming from the lab computer. **b** Picture sequence showing a test experiment, accelerating and decelerating the atoms in linear ramps, causing a sigmoidal position evolution. The pictures are taken with 1 s exposure one right after the other. Observe the blurring in the middle due to movement during the image. Image from M. Genske.

operating from a clean clock. For this reason, we are employing an external generator (HP8640B) to deliver highly stable 400 MHz clock input to both chips on the board [22]. One advantage of a digital generator is that the frequency and the phase of the output can be quickly and accurately switched, but in exchange, there are resolution constraints for frequency ramping.

A frequency ramp is performed by changing $\Delta\phi$ every 10 ns; changing $\Delta\phi$ by one raises the frequency by $400 \text{ MHz}/2^{32} = 0.09 \text{ Hz}$. This means that if a ramp is to take $15 \mu\text{s}$, it must consist of 1500 time steps and thus change $\Delta\phi$ by multiples of 1500, limiting the frequency resolution of the entire ramp to 135 Hz. The DDS chip can also perform frequency ramps with coarser time steps; in our experiment, we choose 100 ns, which increases the frequency resolution of the same $15 \mu\text{s}$ ramp to 13.5 Hz, sufficient for our needs.

The DDS device is controlled by anMBED microcontroller that communicates with it via serial peripheral interface (SPI) to set parameters, namely the base frequency of the two arms, the maximum detuning, the ramp duration and the number of ramps. TheMBED receives a trigger from the control computer which instructs it to in turn trigger the DDS to execute the prepared ramp and to enter the new ramp right afterwards. In this manner, the DDS can be reprogrammed in a few microseconds, which is required if one wants to accelerate repeatedly, since this means ramping to a new frequency each time.

The output signals of the DDS chips are independently amplified and sent to the respective AOM. A variable attenuator is placed in each signal path, allowing amplitude control to change the refraction efficiency of the AOM and thus the beam power on the atoms (see fig. 2.7a). The voltage-variable attenuators shown were replaced after the quantum walks measurements with mixers (Minicircuits ZLW-6+), allowing a much higher bandwidth (220 kHz instead of 30 kHz). Unlike the two-arm setup, the RF setup for the one-arm setup was much more compact, consisting only of a voltage-controlled oscillator, followed by a variable attenuator and an amplifier.

The acceleration was tested by accelerating and decelerating atoms while continuously imaging them. The expected movement calculated from $s(t) = at^2/2$ results (see fig. 2.7b). Another test was performed by inserting acceleration into an atom interferometer (see fig. 3.10b), showing excellent phase stability and no negative impact on coherence.

Back-reflection from fiber ends

The two-arm setup has brought not only new possibilities, but also at least one new problem: fiber back-reflection. The fiber ends from which the two lattice beams emanate towards the atoms are reflecting back a small fraction of the incoming light, about 1%. Together with the two beams interfering, 1% of each beam is back-reflected and forms an interferometer with the main beams (see fig. 2.8). The resulting interference can cause a modulation of up to 15% of the total intensity incident on the atoms, depending on an optical phase difference affected by the movement of a dozen optical components. Also, the intensity incident on the power stabilization photodiodes is modulated as well. The stabilization circuit will respond to this and alter

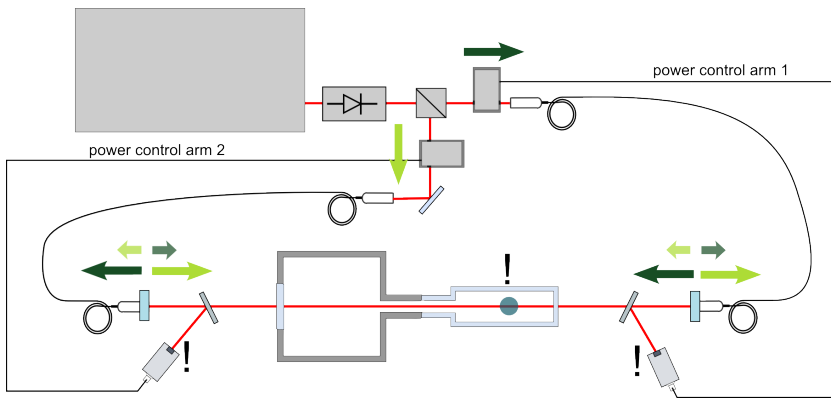


Figure 2.8: Simplified schematic of the setup showing fiber back-reflections. The two lattice beams are represented by dark and light green large arrows. The reflective surfaces are shown as mirrors, returning about 1% in both directions (small arrows). The exclamation marks show where the most harmful interference arises: At the atoms and on the photodiodes for power stabilization.

the beam power mistakenly translating phase fluctuations in this undesired interferometer into power fluctuations.

I have traced the back-reflection to the fiber ends using additional beam splitters to check for reflected light in several positions in the setup. In addition, the optical path length difference in the interferometer can be measured by scanning the laser wavelength and recording the interference fringes, using $\Delta l = c/(2\Delta f)$ with Δf the frequency period of the fringe. The resulting optical path differences for both back-reflections match with the fiber ends pointing towards the atoms. To confirm this, I turn the second-arm fiber around by switching the two ends; this changes one optical path length difference by slightly more than the length of the fiber, which proves that the fiber is responsible and that the reflection is happening close to one end.

This clearly shows that one end on each lattice fiber is responsible, in both cases the one pointing towards the atoms. We consider placing optical isolators to reduce the effect, but space is precious and they make the beams more difficult to overlap. Instead, we used another pair of optical fibers, which has diminished the effect by roughly a factor of three, likely due to the surface quality of the end faces. The FC/APC fibers used are specified to reflect back -60 dB of incoming light, but for freespace coupling this value may be quite a bit higher. If the problem persists, manually polishing the fibers to a 12° angle instead of the standard 8° may be a viable solution.

2.2.4 Coherence in the lattice

Ramsey measurements and dephasing

Coherence in single-particle systems is the ability to maintain and interrogate a superposition of states with a well-defined phase. It is normally

investigated using Ramsey spectroscopy[23] with the common theoretical description modelling a Caesium atom as a quantum two-level system described by the optical Bloch equations[24]. These methods are derived from nuclear magnetic resonance research, which benefits from accessible two-level systems and has spawned advanced techniques for manipulating them[25]. More detailed descriptions of Ramsey spectroscopy on neutral atoms in lattices can be found in [10, 26]; a brief summary is given here:

Coherent superpositions of spin states can be created and interrogated by microwave pulses; these act as rotations of the state vector on the Bloch sphere. Ramsey spectroscopy uses three variants of the general microwave operator, here expressed as matrices in the $|\uparrow\rangle, |\downarrow\rangle$ basis:

$$\hat{U}_{\pi/2} = \frac{1}{\sqrt{2}} \begin{pmatrix} 1 & i \\ i & 1 \end{pmatrix}, \quad \hat{U}_{\pi/2}^\phi = \frac{1}{\sqrt{2}} \begin{pmatrix} 1 & ie^{i\phi} \\ ie^{-i\phi} & 1 \end{pmatrix}, \quad \hat{U}_\pi = \begin{pmatrix} 0 & i \\ i & 0 \end{pmatrix}. \quad (2.3)$$

The operator \hat{U}_π flips the qubit state, and $\hat{U}_{\pi/2}$ implements a quarter rotation on the Bloch sphere and creates a superposition from a pure state. The operator $\hat{U}_{\pi/2}^\phi$ is used as a final operation to interrogate the superposition by mapping it back onto the pure states, e.g.:

$$|\uparrow\rangle \xrightarrow{\hat{U}_{\pi/2}} \frac{1}{\sqrt{2}}(|\uparrow\rangle + i|\downarrow\rangle) \xrightarrow{\hat{U}_{\pi/2}^\phi} |\uparrow\rangle. \quad (2.4)$$

From creation to interrogation, the component states of the superposition may accumulate phase relative to each other depending on the Hamiltonian; common sources are microwave detuning, lattice light shifts, or magnetic fields. In most experiments, the ratio of state populations can be measured while the phase of a state is not directly accessible, so the final pulse must be used to map the phase to the state populations. A full interrogation of a state is performed by scanning the phase ϕ of this mapping, which changes the rotation axis of the operation on the Bloch sphere. The resulting relation of state population is sinusoidal and shifts according to the state phase: $p_{|\uparrow\rangle} - p_{|\downarrow\rangle} = \cos(\phi_{\text{state}} + \phi)$. The desired phase ϕ_{state} can then be extracted from this fringe (compare fig. 3.3).

Decoherence arises foremost by stochastical variations of the state phase ϕ during measurements, leading to a blurring of the sinusoid and a reduction of its apparent amplitude (the contrast of the fringe). This mechanism is more accurately called dephasing and not strictly speaking proper decoherence; see 4.2.3 for a real decoherence mechanism[27]. Ramsey spectroscopy tracks the decay of contrast with increased time between creation and interrogation; the figure of merit is the so-called T_2 time, after which contrast is halved.

The phase fluctuations causing contrast decay are classified as inhomogeneous (acting differently on separate atoms) and homogeneous (affecting all atoms equally). The standard method to combat inhomogeneous effects is the so-called spin echo: A π pulse is placed in the center of the time interval, inverting the spin states. A constant phase accumulation will now impact both components equally and thus have no overall effect. Also, if we are sampling an ensemble of spins that are all experiencing statistically independent (i.e., inhomogeneous) dephasing, spin echo will achieve a marked

improvement in the ensemble signal. Spin echo is a full research field of its own [25], but can be briefly described as a high pass filter on phase fluctuations: signals with a period longer than the total interrogation time are strongly suppressed.

Because a single spin echo operation changes the contrast decay significantly, one often also lists the corresponding coherence time with echo T_2^* . More advanced sequences can contain multiple pulses to raise the filter cut-off, increasing coherence time far beyond T_2^* and may even be used to extract a spectrum of the noise acting on the system [28].

Dephasing mechanisms in our lattice

I have performed Ramsey measurements both in the lattice and with one or two of the laser beams briefly turned off. The results show clearly that the optical lattice is limiting the coherence time in our setup: the inhomogeneous coherence time without any trap is about $T_2 \approx 500\mu\text{s}$, whereas in the lattice with EOM, it is $200\mu\text{s}$. Without trap, atomic coherence is degraded by magnetic field fluctuations. Two effects combine to cause dephasing in the lattice: First, the lattice is causing a shift in the qubit transition by shifting the two levels by different amounts (differential light shift). Second, the atoms are experiencing different trap depths over time, both because of thermal motion in the lattice wells and because of laser power fluctuations [26]. Together, these two phenomena lead to stochastic fluctuations of the qubit phase, decreasing T_2 .

The differential light shift is a combination of scalar and vector light shift effects. On the one hand, the dipole force (scalar light shift) on the two qubit states is not equal because the detuning between laser and transition differs by the qubit level splitting of 9.2 GHz, leading to the intrinsic differential light shift δ_0 . On the other hand, an imprecise polarization state of the lattice beams in either ellipticity or angle will also cause a differential vector light shift, which in our experiment is commonly up to 7 δ_0 .

A mismatch in angle between the polarizations of the lattice beams not only shifts the sublattices apart, but also leads to a differential light shift, due to the 7:1 admixture the 3,3 state experiences from the other chirality. This makes differential light shift depend on the lattice phase φ :

$$\delta(\varphi) = \delta_0 + U_0 \cdot \frac{7 + \cos \varphi}{8}. \quad (2.5)$$

Fortunately, the angles are easy to match using a high-quality polarizer.

An ellipticity of polarization translates into a power imbalance between the two chiralities and thereby causes a differential light shift that can be as large as the full trap depth (for fully circularly polarized lattice beams). Assuming that an extinction $\epsilon = P_H/P_V$ comes purely from ellipticity, the resulting differential light shift is

$$\delta(\epsilon) = \delta_0 + \frac{7}{8}(U_+ - U_-) = \delta_0 + \frac{7}{8}U_0 \frac{2\sqrt{\epsilon}}{1+\epsilon}. \quad (2.6)$$

For a good extinction like 1:8000 and our usual trap depth of 1.6 MHz, this results in 30 kHz differential light shift if both beams have equal ellipticity.

We know that in our experiment, the incoming beam is purely linear and only the returning beam (after passing the EOM) can be elliptical. In that case, constructive interference leads to a four-fold reduction in extinction, because the desired linear component is quadrupled by interference, while the unwanted linear component is not. This reduces the actual differential light shift above to 15 kHz. We can test a laser beam for ellipticity by placing a $\lambda/2$ and $\lambda/4$ waveplate in front of the analyzer and co-optimizing them. This should be able to reduce any homogeneous polarization's extinction to within the specification of the analyzer, so if this improves the extinction further than rotating the analyzer, ellipticity is present.

The strong differential light shift from polarization defects is why the polarization state must be extremely well aligned to achieve good coherence times. Our experimental figure of merit is the extinction given above, which can reach up to 1:100,000 (no EOM in beam), 1:3000 (Conoptics 350-80BK) or 1:8000 (Conoptics 350-105BK). Our experience is that neither angle mismatch nor ellipticity are present: instead, the extinction hits a limit that cannot be improved with the waveplates, meaning that our polarization is inhomogeneous over the beam. We do not have a model describing the impact of inhomogeneous polarization on coherence. Even the basic case of a linear potential gradient causes a deformation of the trapping wells and it becomes questionable to model the atom using harmonic oscillator wavefunctions.

The second aspect required for dephasing is a fluctuation of the trap depth felt by the atoms. One source is the finite temperature of our atoms, which is about $10 \mu\text{K}$, leading to thermal motion in the trap wells. As each atom has an unknown individual energy and phase of the oscillation, the ensemble average shows stochastic variations. The axial movement is faster than our experimental processes and averaged out, while the slower radial oscillation is the strongest source of dephasing, limiting the inhomogeneous coherence time to $T_2 \approx 200\mu\text{s}$. Fortunately, spin echo techniques can strongly reduce this source of dephasing.

Moreover, intensity fluctuations of the laser beam also modulate the trap depth homogeneously for all atoms. To suppress the fluctuations, we have an active power stabilization using a PI servo and an AOM as power modulator.

2.3 Special alignment procedures

2.3.1 Aligning the EOM

As discussed in the last section, a highly linear polarization of the lattice beam is essential to good coherence time because it minimizes differential light shift. Additionally, the axis of polarization of the two lattice beams must be aligned to guarantee full overlap of the two sublattices. The major challenge is to achieve this with the EOM placed in the beam. Below are descriptions for the atom interferometer (EOM in double pass) and the quantum walks (EOM in single pass).

EOM in double pass

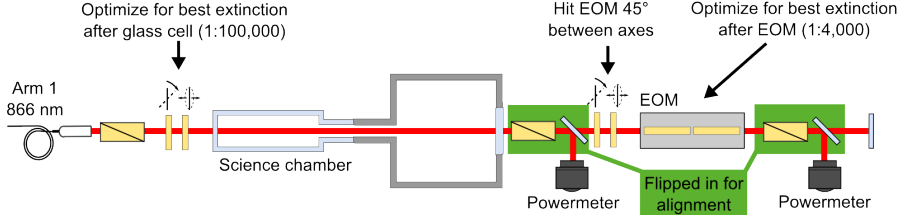
The lattice passes the atoms twice: Once incoming and once reflected, and both extinctions must be about 1 : 3000 to achieve good qubit operations and transport. As we cannot insert a polarizer at the atom position itself, we can only measure the incoming arm once between vacuum cell and EOM and another time between EOM and mirror (see fig. 2.9a). Measuring the polarization of the beam after reflection is impossible, as any beamsplitter inserted would disturb the incoming beam severely. Instead, one has to suppose that good extinction after the first pass also means good extinction of the reflected beam at the atoms.

For the incoming arm, the only birefringent element between polarizer and analyzer is the vacuum apparatus, with one window and the glass cell front face. At the time of the interferometer measurements, it was uncertain which is more strongly birefringent; the tradition was to analyze behind the vacuum chamber. New measurement techniques later revealed that the window is much more birefringent than the cell (see 2.3.4). To achieve a linear polarization of the laser at the atoms, the waveplate duo in front of the vacuum chamber is tuned to maximize the extinction at the analyzer behind the chamber (see fig. 2.9a); if no good value can be reached (worse than 1:50,000), the analyzer is rotated a bit and the waveplates are realigned. We now know that this aligns the polarization to the axis of the window's birefringence, passing both cell and window with a well-defined linear polarization.

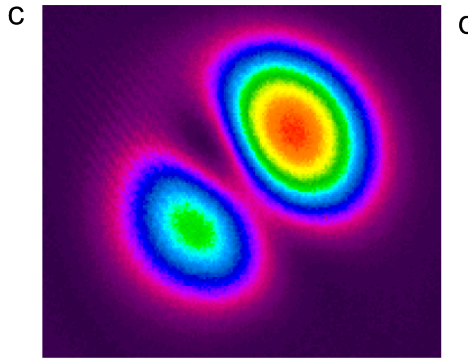
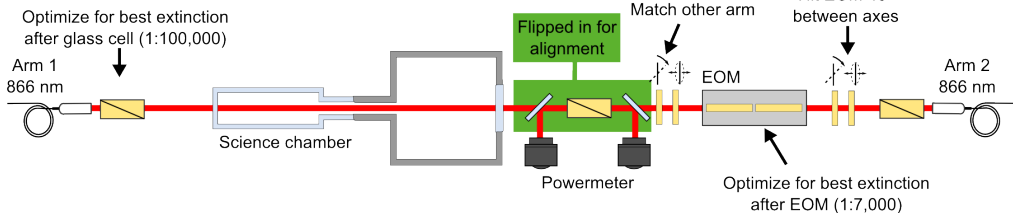
The more difficult part of the alignment is to place the EOM in the reflected arm. A 5-axis mount is available to control tilt and shift in both directions transversal to the beam. Also, a waveplate duo is placed in front of the EOM to allow rotation of polarization (instead of a cumbersome rotation of the EOM) and compensation of ellipticity. The $\lambda/4$ plate also fulfills the important role of switching between linear and circular basis in polarization, to allow the EOM to act as a circular phase shifter. After placing the EOM, it is first shifted and tilted until the beam passes without clipping or internal reflection. The EOM is then rotated and tilted to minimize the extinction, which should decrease to about 1 : 30,000. This value is reached when the beam passes along the longitudinal axis of the crystals and is polarized along one of the two transversal axes. To get the most precise alignment, the EOM voltage can be modulated and the polarization analyzed with a polarizer at 45° . When the incoming polarization hits the axis precisely, the polarization modulation is minimal and should be hardly visible on the signal. In general, tilt and rotation can interact due to the birefringence of the crystals, so an iterative optimization of the two tilt degrees of freedom and the rotation angle is advised.

If the desired extinction is reached, the EOM is well placed with polarization passing on-axis. In this configuration, both chiralities are shifted equally and no state-dependent transport is possible. That requires the polarization to hit at 45° between the two crystal axes. A precision of half a degree is fully sufficient. A good way to implement this is to rotate the analyzer behind the EOM by 45° using the mount's scale, then aligning the

a One-arm setup: EOM in double pass



b Two-arm setup: EOM in single pass



d

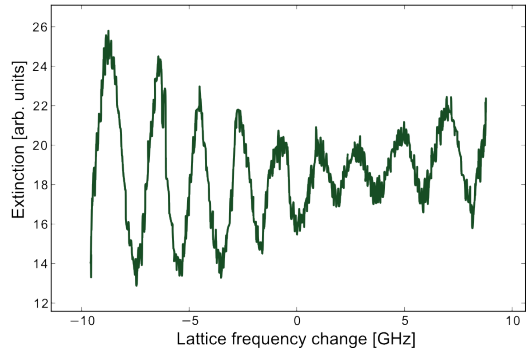


Figure 2.9: **a** Polarization alignment for EOM in double pass. The birefringence of the vacuum windows is precompensated using the first duo of waveplates. The second duo matches the lattice polarization to the EOM, resulting in optimum extinction after one EOM pass. EOM quality affects extinction most severely when polarization enters at 45° to the crystal axes, as is needed for shifting. Note that only high-quality Glan-Laser polarizers and zero order waveplates custom-made for our wavelength are in use. **b** Modified scheme for EOM in single pass: the first beam is rotated to the eigenaxes of the vacuum window. The other arm is aligned at 45° to the EOM axes, then the EOM is optimized for extinction. Finally, the polarization of the two arms is matched. **c** Beam profile recorded after EOM and a crossed polarizer: the two spots visible stem from polarization inhomogeneity caused by the EOM. Image from L. Förster. **d** Transmission through a crossed polarizer behind the EOM as a function of lattice detuning. The clearly visible fringe indicates a Fabry-Perot effect inside the EOM, which changes extinction by a factor of two depending on laser frequency. Zero frequency change corresponds to a laser frequency of 346,220 GHz or about 865.9 nm.

waveplate duo for best extinction. At this angle, the impact of crystal homogeneity is increased and extinction suffers, reduced to about 1 : 4000 at good alignment, 1 : 1000 in poor cases. Reaching good extinction requires tilting and shifting the EOM, as well as experimenting with small offset voltages (less than 40 V) applied via the driver. The EOM shows a tendency to settle over hours and days, meaning that once removed from the beam, the extinction reachable tends to improve over several days after reinsertion. To reach optimum stability, the EOM is temperature stabilized to 30°C using a heating tape driven by a digital PID controller (Wachendorff T16) and monitored over a PT100 sensor.

There are two known peculiarities of the EOM utilized, and both have been confirmed in several EOMs made by Conoptics. The first is the profile of polarization across the beam: When viewed through an analyzer on a beam profile camera, there is a clear double spot structure. Rotating the analyzer makes one lobe shrink at the expense of the other, indicating that they contain linear polarization of different angle, or rather, an angle gradient exists in the beam. This spot persists if no voltage is applied to the EOM, so it does not derive from electric field distributions. Other candidates are strain from crystal mounting or k-vector spread in the laser beam (analogous to the isogyre patterns [29]).

The second feature is in the wavelength-dependence of extinction. Scanning the wavelength of the lattice laser over a period of a few GHz while monitoring extinction shows a sinusoidal oscillation. This indicates a Fabry-Perot effect inside the EOM, which modulates the polarization. From the period of the modulation, the effective length of the cavity can be calculated and translated by knowing the refractive index of KD*P perpendicular to the optical axis, since $\Delta\nu = c/(2nl)$. This results in a length of 5 cm approximately, since we do not know the refractive index of the fluid or the empty space between the crystals precisely. Moreover, the dimensions of the Conoptics 350-80BK contain several spacings of about 5 cm between similar surfaces, leading to possibly coupled resonators. Inquiries with Conoptics have revealed that the fluid is only approximately index-matched and that a custom fluid could greatly reduce the index step from fluid to crystal.

EOM in single pass

The switch to two independent beams for the conveyor belt technique requires using a longer EOM in single pass and changes the alignment procedure.

The rotation power is increased by longer crystals but even so only suffices if the EOM is cooled to 17°C. A peltier element with an Innovatek CPU cooler replaces the heating tape; the controller can be reconfigured in software. As the cooling element is placed at one end, ambient temperature inflow may cause temperature gradients in the crystals and affect the birefringence cancellation. A 3 mm foam shell is wrapped around the EOM as insulation to prevent this.

To gain control over input and output polarization of the EOM, a waveplate duo is placed in front and behind (see fig. 2.9b). The input polarization is

first aligned to one of the axes using the method described above; the $\lambda/4$ plate is needed because a real $\lambda/2$ plate alone will not produce an ideal rotation of the polarization. An analyzer behind the EOM should then show a very good extinction of 1:30,000 or better. Rotating the analyzer by 45° defines the polarization orientation necessary for shifting; extinction can be minimized using the waveplates in front of the EOM (reaching the required input polarization between the eigenaxes).

Extinction will now be normally quite bad; the way to improve it is first EOM tilt (may only go down to 1:500 extinction), then tilt and offset iterated, as in the double pass case. Offset voltage can be replaced to some degree by the waveplates in front of the EOM (in particular the $\lambda/4$). In fact, best extinction has sometimes been achieved with a rather elliptical input polarization (extinction about 1:6).

After the EOM itself is aligned, the output polarization must be matched to the first arm of the dipole trap: the analyzer is flipped in and turned to extinction with the first arm. The waveplate duo behind the EOM is then used to bring the second arm into extinction as well, at which time the extinction reachable should be as good as when analyzing directly behind the EOM.

2.3.2 Axial ground state cooling

Microwave sideband cooling is a technique developed on this experiment [30] that allows bringing the atoms into the ground state of axial motion. After loading from the MOT, our atoms are initially thermal at $10\ \mu\text{K}$ and occupy several motional states in the axial ($\bar{n}_{ax} = 1.2$) and radial ($\bar{n}_{rad} \approx 200$) directions of the trap. The key is to perform a qubit transition with a change of motional state associated. This is normally impossible for a microwave photon, which carries little momentum, but in our state-dependent lattice, displacement can substitute for momentum and the atom is switched between two spin-states trapped in spatially displaced wells. In other words, two normally-orthogonal motional states are given a non-zero coupling by displacing them with regard to each other using a small phase shift between the two chiralities, usually about $\varphi = 14^\circ$. Then, an optical repumper can be activated that will incoherently undo the change of hyperfine state with a low probability of modifying motional state. The energy is dispersed by the spontaneous emission in the repumping event.

Using the techniques established in [30], cooling to $\bar{n}_{ax} = 0.03$ is possible. This is detectable by the disappearance of the cooling sideband from microwave spectra: Without motional quanta available, no transition is possible on that frequency (see fig. 2.10c).

To prepare the coherent delocalization of atoms, axial cooling is a standard procedure. It enhances the fidelity of microwave operations due to the decreased axial motion, which reduces the high-frequency fluctuation of differential light shift. It also allows a more precise suppression of motional excitation during shifting, as the excitation properties of the higher motional states can be ignored.

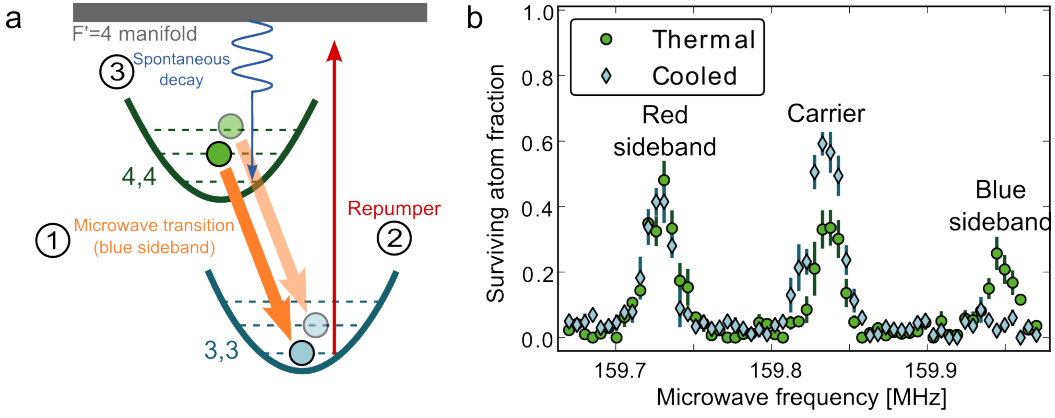


Figure 2.10: **a** Simplified scheme for the microwave sideband cooling cycle, shown using the trapped state $|F = 4, m_F = 4\rangle$ and $|F = 3, m_F = 3\rangle$ and the manifold of excited states $|F' = 4\rangle$. The atom is switched from $|F = 4, m_F = 4\rangle$ to $|F = 3, m_F = 3\rangle$ by a microwave sideband pulse, which removes one vibration quantum from the atom. The atom is then quickly optically repumped to the excited states. Because these are unstable, it quickly decays back into $|F = 4, m_F = 4\rangle$ (closing the cooling cycle) or $|F = 3, m_F = 3\rangle$ (waiting for another repump). The vibrational state is in most cases not changed by the repump events, so every cooling cycle removes one vibrational quantum. **b** Experimental data showing a microwave spectrum with carrier and the first blue and red sideband. The blue sideband is the cooling sideband: after cooling, it disappears because the vast majority of atoms are in the ground state.

2.3.3 Tuning transport parameters

Transporting atoms coherently over multiple lattice sites requires precise tuning of two further parameters, namely the voltage $V_{2\pi}$ required by the EOM to reach a lattice shift of 2π and the ramp time τ preventing motional excitation.

First, we determine the voltage $V_{2\pi}$; reaching $\varphi = 2\pi$ corresponds to reaching a full overlap of the two sublattices. The shape and position of the microwave spectrum are highly sensitive to slight displacement of the two chiralities and comparing a qubit operation at high voltage to the 0 V spectrum allows the best determination of $V_{2\pi}$. To achieve greater precision, a short transport sequence of four steps is usually performed, involving three π pulses. Shifting always broadens the resulting spectrum, but the resonance frequency should not move. This alignment is critical to about 1% because shifts over multiple sites require a spin change every step, and an error in overlap reduces the spin transition effectiveness by the Franck-Condon factor (see eq. 2.1.11 in [11]). The best measurements have shown 98.97(7)% success rate per spin transition while shifting, measured by shifting many steps and counting the fraction of atoms arriving on target (compare fig. 2.11).

Once $V_{2\pi}$ is known, the last parameter to adjust is the ramp duration τ . For interferometry, this is the most significant parameter, as the ramp speed

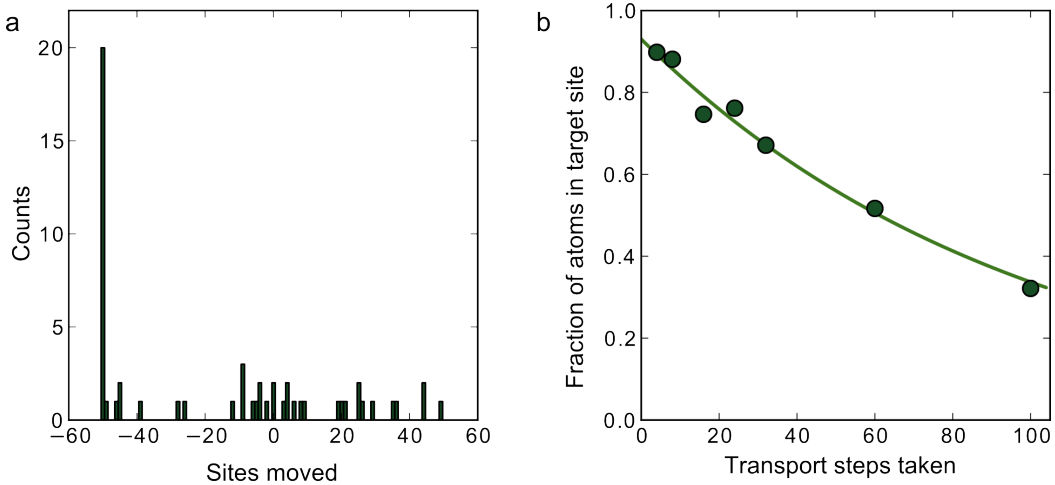


Figure 2.11: Transport effectiveness is detected by transporting single atoms by a number of steps and measuring the fraction of atoms in the target site with single-site detection. **a** Example histogram for 100 steps transport (i.e., 50 sites movement). The placement of incorrectly shifted atoms follows a random distribution. **b** The fraction of correctly transported atoms decreases exponentially. The fit gives a fidelity per step of 99%. Error bars are smaller than plot markers.

controls motional excitation and heavily affects contrast. This also offers the best way to optimize the ramp duration, by performing a interferometer and changing τ until contrast is maximized. The "double diamond" geometry (for operations see fig. 3.5) is the most suitable here, as it automatically compensates spatial as well as state-dependent detunings in first order, as is visible from the stable phase. According to the theory [10], an optimum is expected around $\tau = 18\mu\text{s}$; experimentally found values range from 16 to $20 \mu\text{s}$. The precision with which the optimum can be determined is usually about $0.2\mu\text{s}$ and the probability of motional excitation becomes less than 1% (cmp. section 3.3).

A way to double-check the hypothesis "maximum contrast equals minimum excitation" is to observe the microwave cooling sideband. After sideband cooling, it is depressed below the detection threshold; excitation of atoms to higher motional states will make it reappear. Sideband spectra after transporting cooled atoms are presented in fig.2.12; the depression around the optimum τ is clearly visible. The disadvantage of this technique lies in the reduced data quality, as the sideband disappears below the detection noise for a normal number of repetitions.

Ramp duration should be reoptimized at the beginning of every experiment day, as the optimum changes somewhat depending on dipole trap power and polarization.

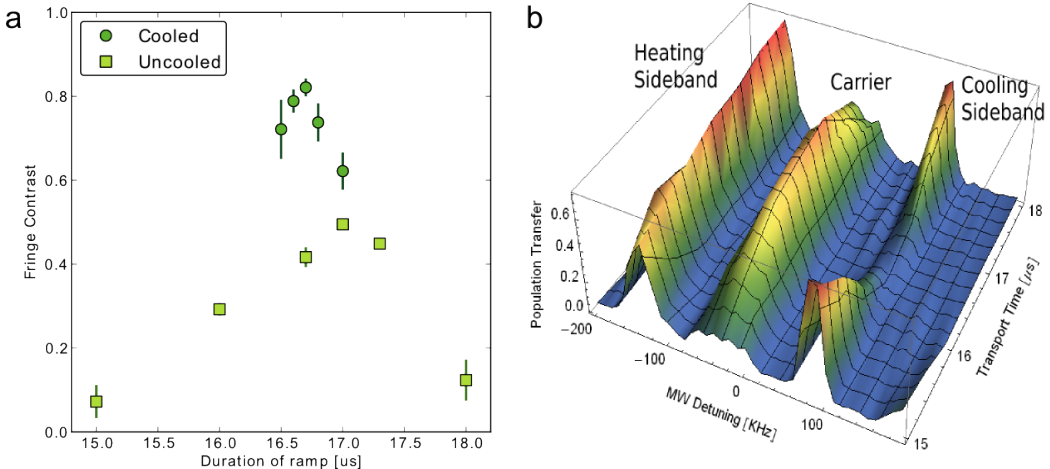


Figure 2.12: Contrast of an interferometer for different transport ramp durations. Small variations in duration change the probability of motional excitation significantly. **a** The two traces show the difference between axially cooled and uncooled atoms, although it is possible to reach higher contrast with uncooled atoms as well. **b** Sideband spectra showing carrier with first red and blue sideband. The blue cooling sideband is suppressed unless transport reexcites atoms. Note that the two figures are from different days. Image from Dr. Jai-Min Choi.

2.3.4 Measuring vacuum window birefringence

Apart from the EOM, the major unknown affecting the polarization of light at the position of the atoms are the windows of the vacuum chamber. The issue is that the atoms experience the polarization after one of the two possibly birefringent elements is passed, but we can only measure the state after both have been passed using optical methods. Indeed, standard polarimetry techniques establish the Müller matrix of an optical element by placing polarizers on both sides of it; thus, one could measure the joint Müller matrix of both windows, but this cannot be resolved to the two individual matrices. The key to solve this problem is to use the atoms themselves as polarimeters by measuring the differential light shift caused by the ellipticity of light (see 2.2.4). This is done by turning off one of the lattice beams for 100 μs , thereby turning the lattice into a running wave trap and eliminating issues arising from lattice structure or the two sublattices. Taking a microwave spectrum of the atomic transition gives the resonance frequency with a precision of 1 kHz. The linear input polarization through the window of interest can now be rotated from spectrum to spectrum, while following with the other beam to maintain the initial lattice for trapping atoms. If the window is birefringent, the change in polarization angle will cause an ellipticity to arise at the atoms, and the resulting differential lights shift changes the resonance frequency. See the data in fig. 2.13: the data shows a sinusoidal behaviour.

I introduce a basic model: the birefringence is induced by stress via the photo-elastic effect [31] and is proportional to the local stress:

$$\Delta n = C \cdot (\sigma_{11} - \sigma_{22}), \quad (2.7)$$

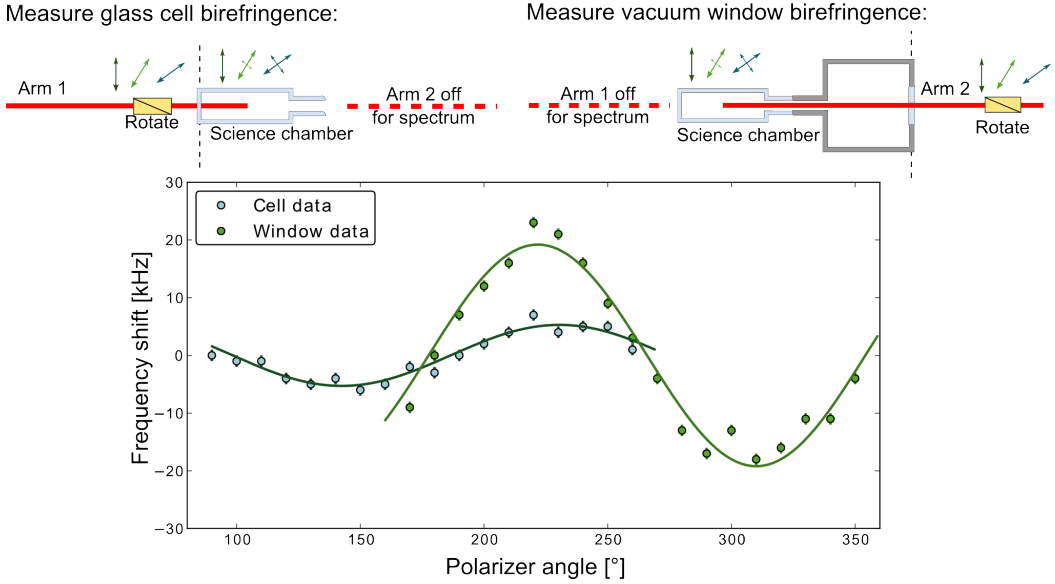


Figure 2.13: Determination of the individual birefringence of the vacuum window and the glass cell by using the microwave transition frequency to measure ellipticity. The atoms are trapped in the normal lattice, but for the spectrum, one arm is briefly turned off to eliminate lattice effects. The polarization of the other arms is rotated step-by-step, leading to different ellipticities at the atoms. Each data point is extracted from one microwave spectrum; the two data sets are fitted with a sinusoid to find zero-crossings and amplitude.

where C is the photoelastic constant of the material and σ_{11}, σ_{22} are the two principal stresses. It is a well-known result from mechanics that a plain body under stress in the plane always has a coordinate system that diagonalizes the stress tensor, leading to two orthogonal eigenaxes along which the stress acts; these principal stresses are our σ . According to this model, our glass window behaves like a waveplate of unknown retardation R . The effect is a rotation of the Poincaré sphere by $R \cdot 2\pi/\lambda$ around the axis connecting the two linear polarizations incident on the principal axes. Let us call the angle between the (yet unknown) axes of the waveplate and the incident polarization axis α . The intensity difference of the two circular components can then be calculated:

$$I_{\odot} - I_{\circlearrowleft} = I_0 \cdot \sin 2\alpha \cdot \sin \left(\frac{2\pi R}{\lambda} \right) \quad \Rightarrow \quad U_{\odot} - U_{\circlearrowleft} = U_0 \cdot \sin 2\alpha \cdot \sin \left(\frac{2\pi R}{\lambda} \right). \quad (2.8)$$

This causes the differential light shift $\hbar\delta = \hbar\delta_0 + 7/8 \cdot (U_{\odot} - U_{\circlearrowleft})$, in which δ_0 is the scalar differential light shift as earlier.

Now we can interpret the sinusoid curve: the zero-crossings occur when the incident polarization hits the principal axes of the stress distribution. The amplitude of the sinusoid can be translated into the optical retardation of the element if the total trap depth U_0 is known, setting $\alpha = \pi/2$ at the maxima. Note that for the same power in each beam, the trap depth is reduced 4x from the lattice because the lattice has been turned off (half the

power is missing and so is the constructive interference). In the case of only one beam active with 6 mW, this means a trap depth of 330 kHz for arm one (going through the cell) and 170 kHz for arm two (going through the window, larger focus at the atoms after minimizing the beam radius in the EOM).

This gives a retardation of roughly $\lambda/47$ for the window and $\lambda/363$ for the cell; I say roughly because it is based on a calculated U_0 , not a measured one. Most importantly, the eigenaxes of the window are clearly shown, meaning that a linear polarization can be shone onto the atoms without disturbance at this orientation. To achieve a more precise measurement, the quickest way is to raise the trap strength; we could probably realize about a factor 50 more laser power, yielding the same factor in sensitivity.

3 Single Atom Interferometer

3.1 Theory

Interferometry means splitting one quantum state into several and letting them evolve in time and/or space, finally recombining them to read out the difference between the phase they have accumulated. The best known case is optical interferometry, in particular the archetypical Mach-Zehnder interferometer, which consists of two beamsplitters, the first splitting and the other rejoicing the two paths of light, creating beam paths in the shape of a diamond. The common way to refer to the two beam trajectories is to call them the "arms" of the interferometer.

In quantum optics, an ideal non-polarizing beam splitter is a unitary operator \hat{B} of the form seen in eq. 3.1 for the basis $|V\rangle$, $|H\rangle$ [32]. The system becomes interesting if one allows some evolution of the state between the two beam splitters, e.g., passing an optical element, which may change the phase of one arm relative to the other. Then, the transmission in one port of the interferometer is a sinusoid function of the phase accumulated:

$$\hat{B} = \frac{1}{\sqrt{2}} \begin{pmatrix} 1 & 1 \\ 1 & -1 \end{pmatrix}, \quad \left\langle V \left| \hat{B} \cdot \begin{pmatrix} e^{i\phi} & 0 \\ 0 & e^{-i\phi} \end{pmatrix} \cdot \hat{B} \right| V \right\rangle = \frac{1}{2} |\cos \phi|^2; \quad (3.1)$$

nanoscale changes of the optical path length can be mapped to strong fluctuations of the received light power. Optical interferometers are accordingly used for high bandwidth and high sensitivity phase measurements, e.g., for measuring displacement, refractive index, optical phase noise or laser linewidth.

The beamsplitter for photons is quite similar to the $\pi/2$ microwave pulse for a two-level qubit system like our atoms. While microwave operations cannot produce the exact matrix \hat{B} because of the degrees of freedom available in $\hat{C}(\theta, \phi)$ (see eq. 2.1), $\pi/2$ pulses can nevertheless be used to perform interferometry with atoms. A big difference between photons and atoms is that the latter may accumulate phase from a much wider range of effects, connected to the various terms an atomic Hamiltonian may have, such as magnetic fields, inertial force, optical potentials, atom-atom interaction etc. This is what makes atom interferometers so useful and flexible and in fact, atom interferometry is a major field with significant discoveries.

The two main techniques are atomic beam interferometers and cold fountain interferometers. Atomic beams are the older technique, using collimated beams emanating from an oven to produce fringes very much like beams of light, and although the means of beam steering are different, they recognizably correspond to mirrors, gratings and the like [33, 34]. Remarkably, these techniques have even been transferred to molecules and used to

show coherence of extremely large bodies, even up to the C_{60} molecule [35], or make precision measurements of fundamental properties like the electron's dipole moment [36].

Fountain interferometers are more recent developments utilizing magneto-optical traps to gather large, compact atom clouds and achieving extremely precise phase measurements. Interference occurs by launching two parts of the cloud upwards at different speeds (basically, splitting the paths in momentum space), thus letting one travel higher than the other one [37, 38]. By applying a second laser pulse inverting the velocity difference at the apex, the two clouds arrive simultaneously at the launching point for state detection. Fountain interferometers are characterized by long periods of complete free fall and a high rate of atoms interrogated. As a result, only few effects (mostly magnetic fields and laser noise) can disturb the phase accumulation, and the phase accumulated can be extremely large, leading to some of the most precise interferometry measurements achieved [39, 40].

Our interferometer is in a third class, trapped interferometers. Instead of letting atoms propagate freely, they are tightly held, allowing much greater control and flexibility in the experiment [41, 42], but also introduces new phase fluctuations from the trapping (see 2.2.4), making precision measurements more challenging.

To predict the phase difference accumulated in an atomic interferometer, the time evolution of the atomic states under a Hamiltonian can be calculated from the Schrödinger equation:

$$\frac{i}{\hbar} \partial_t |\Psi\rangle = \hat{H} |\Psi\rangle \implies |\Psi(t)\rangle = e^{\frac{i}{\hbar} \hat{H} t} |\Psi(0)\rangle. \quad (3.2)$$

The expression becomes most convenient when \hat{H} is diagonal in position and spin, accumulating phase based on the eigenvalues of the states.

In our measurements, the two paths have a similar evolution of their momentum, meaning the kinetic term accumulates the same phase for all paths and can be dropped. The potential term remains and can cause an energy difference based on position or spin.

To calculate the resulting phase difference, one must consider not two states, but the two different *arms* of the interferometer and the changes in states of each arm during the interferometer. The phase difference accumulated between the two arms results from the energy $E(t)$ via the integral:

$$\phi = \phi_1 - \phi_2 = \frac{1}{\hbar} \int_0^t E_1(t) - E_2(t) dt, \quad (3.3)$$

where "1" and "2" signify the arms of the interferometer, or quantum paths. The spin state correlated to one path changes in time (see fig. 3.1a), as may the energy, but this is only bookkeeping. Integrating over the instantaneous values of the energy will provide the correct phase accumulated from the potential term of the Hamiltonian. The exception are microwave pulses, which may add an energy-independent phase if applied with detuning. Said phase has to be calculated separately by solving the optical Bloch equations.

Although the paths accumulate phase separately, the interferometer responds to the difference in phase. Because of this, interferometers are often aimed at measuring gradients [3]. If some field or potential U has a

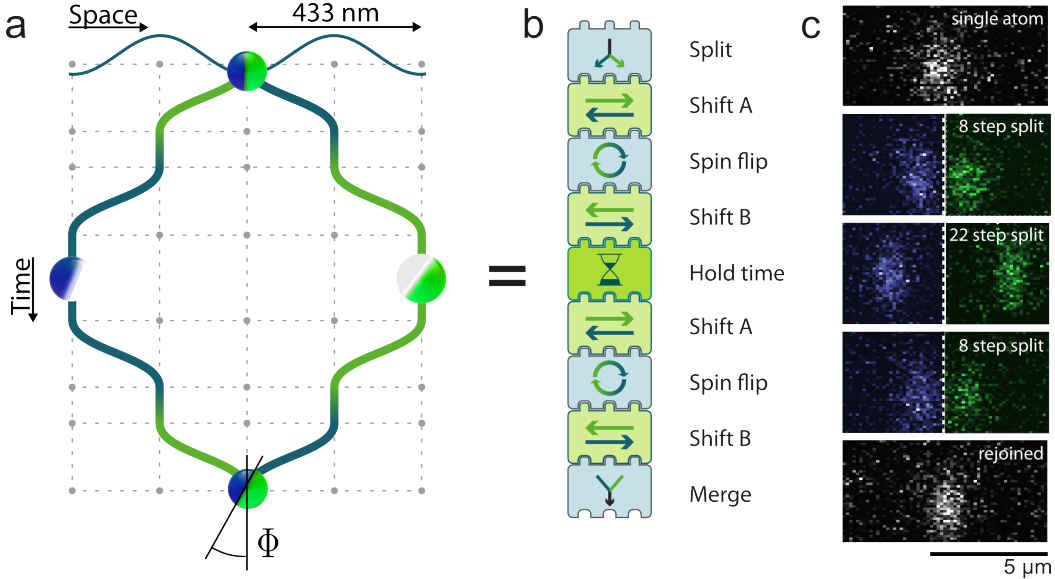


Figure 3.1: **a** Schematic of a four-step diamond geometry. A $\pi/2$ pulse brings the atom into a superposition and the two spin states are separated by two shifts for a distance of 2λ . After remaining at this distance for some time, they are recombined and a final $\pi/2$ pulse maps the phase difference into state populations. **b** The sequence represented in primitive operations. Note the implementation of multi-step shifting. **c** The largest coherent interferometers can reach almost $10 \mu\text{m}$ separation using 44 shifts. The images were made by recording two times after half the sequence, finding the atom right or left.

linear gradient $\partial_x U = f(t)$ it can proportionally alter the energies of the two spin states: $E_{|\uparrow\rangle}(x, t) = \alpha \cdot x \cdot f(t)$ and $E_{|\downarrow\rangle}(x, t) = \beta \cdot x \cdot f(t)$. One can split the energy shift into a spin-symmetric part $(\alpha + \beta)/2$ and a spin-antisymmetric part $(\alpha - \beta)/2$. Besides the gradient, the integral in eq. 3.3 depends on the trajectory $x(t)$ of the atomic paths.

I will discuss first the basic "diamond" geometry visible in fig. 3.1, which splits and rejoins the atoms in the most direct manner, resembling a diamond shape. All other sequences I have performed are variants of this elementary one. The operations required are shown in fig. 3.1: A $\pi/2$ pulse creates the coherent superposition, a series of shift operations and π pulses moves the two states apart, a similar sequence moves them back together and a final $\pi/2$ pulse projects phase onto population.

The resulting trajectory can be computed: Shifts cause a linear movement over half a lattice site in a time τ_s , all other operations cause no movement but keep the path stationary for their duration. Microwave π pulses in particular need a time τ_π . The symmetry of shifts means that the interferometer ends on the initial site. For state-symmetric gradients, the energy difference integral can be greatly simplified, because the current spin state of a path is insignificant:

$$\phi = \int_0^t [E_1(t) - E_2(t)] dt = \frac{\alpha + \beta}{2} \int_0^t \Delta x(t) dt =: \frac{\alpha + \beta}{2} A, \quad (3.4)$$

where $\Delta x = x_1(t) - x_2(t)$ is the distance between the two arms and A is defined as the spacetime area of the interferometer. That the sensitivity of an interferometer depends on the enclosed area is a concept applicable to several types of interferometry, e.g., SQUIDs[43]. A can be calculated geometrically, and for a diamond with n shifts and no hold time it is:

$$A(n) = \frac{\lambda}{2} \left[\left(\frac{n}{2} \right)^2 \cdot (\tau_s + \tau_\pi) - \frac{n}{2} \cdot \tau_\pi \right]. \quad (3.5)$$

The sensitivity of an interferometer scales quadratically with the maximum separation, making large separations the main strategy for high-precision measurements.

The situation is more complicated for state-asymmetric measurements. Here, the integrand $\Delta x(t)$ gets an alternating sign, as the π pulses exchange spin states between the two paths, reversing the phase accumulation. Also, a calculation based on eq. 3.3 only works for gradients that are too weak to significantly detune the atomic resonance - otherwise, phase effects and incomplete population transfer arise at each π pulse. This is the main reason no state-asymmetric gradient was measured in my thesis.

For gradients that are sufficiently weak, the spacetime area can nevertheless be calculated and is

$$A(n) = -\lambda \cdot n \cdot \tau_S. \quad (3.6)$$

This much shorter formula has only a linear dependence on the number of shifts, and is independent of the π pulse duration. The reduction from quadratic to linear dependence occurs because the pieces of spacetime area added from one shift operation to the next have opposite sign and almost the same area (see fig. 3.2). The only difference is the one additional shift performed in the latter operation (during opening). The time of the π pulses does not contribute to this formula because during the pulse, each path spends half the time in either spin state.

If the gradient is strong enough to detune the microwave transition significantly, fully modelling the effect of detuned pulses requires solving the Bloch equations [44] for each pulse and departing from the energy difference integral. Moreover, detuned pulses lead to path errors that cause interference at lattice sites next to the target; very complicated effects related to quantum walks with unbalanced coins arise (see 4.3.2). In the end, a full simulation of the quantum walk using density matrix formalism and numerical solution of the Bloch equations would be required.

I have extended the single diamond geometry in two ways: By mirroring it and by inserting hold times. Appending a mirrored diamond creates the double diamond geometry (for operations see fig. 3.5), which accumulates no phase from either spin-symmetric or antisymmetric gradients because the second diamond precisely cancels the first one. This effect strongly resembles normal spin echo techniques, which use π pulses to cancel the sensitivity of a quantum state to low-frequency disturbances. We have therefore dubbed it "spatial spin echo", as it rephases low-frequency spatial disturbances; constant gradients should be fully erased. Apart from rephasing, another application is to measure a change in gradient, while suppressing all constant background effects.

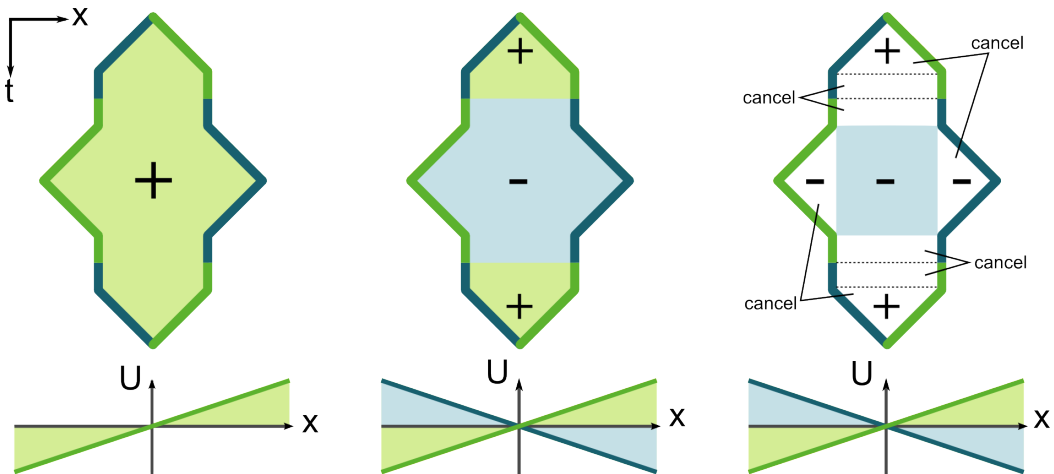


Figure 3.2: Behaviour of the spacetime area for interferometers with diamond geometry. The shape stems from the alternating linear shifts and state switches while stationary. The return points are determined by not switching the state, so the next shift operation starts moving the arms back together. **a** State-symmetric gradients cause phase accumulation proportional to the total spacetime area enclosed by the two paths, irrespective any state switches. **b** State-antisymmetric effects change with state switches, requiring an alternating sign to be used for different segments of the spacetime area. **c** A graphical representation of how the alternating sign leads to a strong reduction in effective spacetime area: The pulses are each cancelling completely, and the alternating sign causes major cancellation between different areas. Only a small area linear in the number of shifts (blue) remains.

The other extension is to insert a hold time τ_h at the maximum splitting, adding a spacetime area of $\Delta x_{max} \tau_h$. For measuring potential gradients, this is inferior to the quadratic behaviour of the normal diamond, but it could keep the atoms near an object of interest, and can also accumulate phase without any possible interference from the shifting process. The hold time can also be filled with π pulses to realize a spin echo sequence inside the hold time in order to reduce inhomogeneous dephasing.

3.2 Measuring potential gradients

3.2.1 Phase detection and noise

Phase detection

An interferometer measurement in our experiment does not directly return a phase; instead, we map the quantum state resulting from the interferometer to spin state populations, in order to extract the phase of the interferometer. We detect state population by counting atoms: The initially loaded and counted N atoms are all optically pumped into $|\uparrow\rangle$, the interferometer is performed and a push-out laser removes all $|\uparrow\rangle$ from the lattice, leaving only

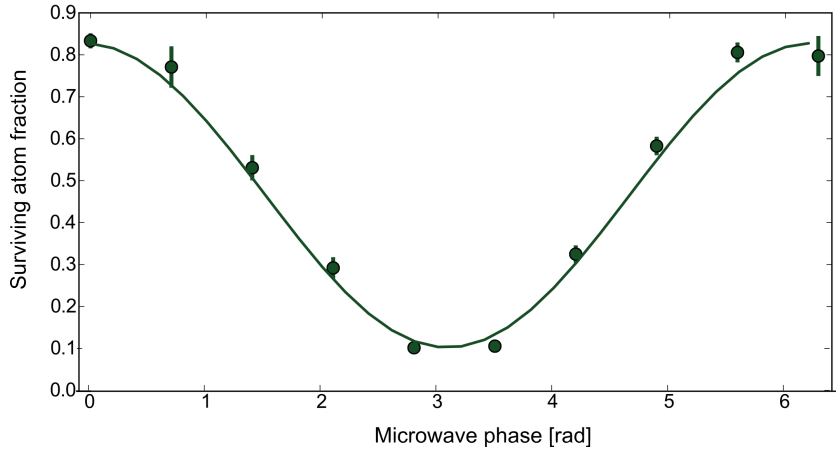


Figure 3.3: A Ramsey fringe for $C = 0.78$, $\phi = 0.06$. Each point was repeated 20 times; the error bars are the standard deviation of these repetitions to measure shot-to-shot fluctuations in the experiment. The resulting atom number N per point was between 600 and 1100; projection noise is therefore expected to be less than 0.2%.

the $M |\downarrow\rangle$ atoms in a second photo. A small fraction of atoms is lost independent of spin state due to temperature effects, leaving about $\gamma \approx 95\%$ of atoms. The fraction ϱ of surviving atoms is then

$$\varrho(\phi_{\text{MW}}) = \frac{M}{N} = \gamma \frac{1 + C \cdot \cos(\phi + \phi_{\text{MW}})}{2}, \quad (3.7)$$

with C the fringe contrast and ϕ_{MW} the phase of the join operation, which is scanned to produce the fringe. The interferometer measurements are generally performed with 30-50 atoms in the picture per shot, ten phase points and twenty repetitions per point, yielding 600-1100 atoms per point (see fig. 3.3). After the individual $\varrho(\phi_{\text{MW}})$ values have been measured, the phase, contrast and survival rate are extracted from them by a nonlinear fit.

A large challenge during the measurements was maintaining phase stability. Series of interferometry results are only useful if no spontaneous shift in the interferometer phase can occur, but exactly this seemed to happen in early measurements. To investigate this further, two long duration measurements were recorded in which a diamond interferometer was performed for several hours in a row without realignment of the setup. The results are displayed in fig. 3.4a and show an acceptable stability (considering the experiment was running without realignment for eight hours), except in the shaded areas. Here, phase is drifting strongly, covering several full revolutions even, and the reason is the lattice laser dropping out of its wavelength lock. The connection between wavelength and phase is likely the EOM's etalon effect (see fig. 2.9d), since it can change the state of polarization hitting the atoms significantly and thus change the differential light shift.

Our Ti:Sa laser is initially locked by a stock multi-stage system that keeps the laser wavelength stable to a few pm, which can still be monitored using a wavemeter. This is not sufficient, because the etalon effect discovered

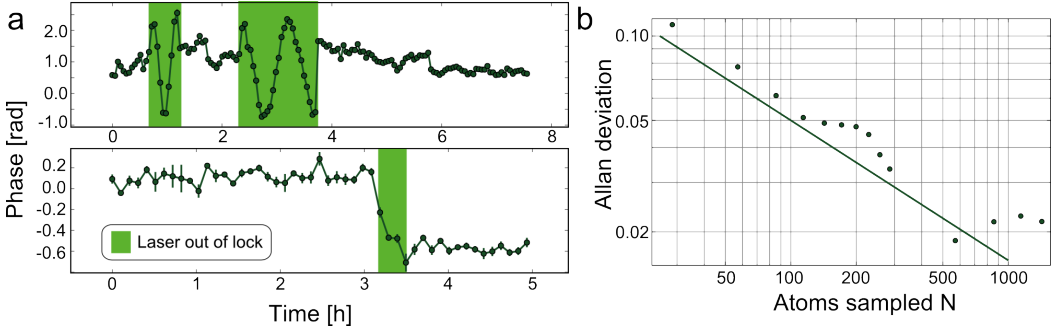


Figure 3.4: **a** The interferometer phase for two long-run interferometer measurements. Both datasets were taken in a normal four-shifts diamond sequence. The resulting datastream was sliced by hundred runs of the experiment or about six minutes. Under normal operation, drifts on the order of 100 mrad occur. The shaded areas with large phase fluctuations were tracked to the lattice laser falling out of wavelength lock. The main connection between laser wavelength and phase may be the EOM's etalon effect (see fig. 2.9d). The lower trace was produced after leaving the lattice laser to thermalize for several hours. **b** The Allan deviation of the surviving atom fraction ϱ , measured on the flank of the interferometer fringe. The points stay mostly above the theoretical limit (solid line), which is $1/\sqrt{2N}$, indicating additional noise. Long term drifts are not very strong on this timescale, but seem to begin at a few hundred atoms sampled. The bump at 200 atoms corresponds to a timescale of about 3 minutes, pointing to possible issues with the air conditioning.

on the EOM (see fig. 2.9d) has a periodicity of about 4 pm, so I placed an additional lock stage to prevent modulation of the extinction. This stage uses a Fabry-Perot cavity with the lattice laser in one polarization and the MOT repumper laser in the other to indirectly lock the Ti:Sa to the atomic resonance, albeit with 17 nm offset. The quality of the lock can be estimated using the cavity signal to stabilize the laser to better than 0.05 pm.

Lock breaks can occur for two known reasons:

1. The laser warms up during operation and drifts too far for the range of its wavelength actuators.
2. A mechanical shock knocks the MOT repumper laser out of lock.

The top plot in fig. 3.4a shows a lock break from the first mechanism and the strong drifts of the phase after losing lock. The bottom plot is an example for a lock break after mechanical shock, showing a step in the phase. In both cases, the laser was relocked to the original wavelength. Relocking the laser to the same wavelength as before (read off a Coherent WaveMaster with 1 pm resolution) doesn't lead to the same interferometer phase as before. I could not identify the reason for this, but the wavelength-dependent polarization effect of the EOM is the only known effect that is sensitive to wavelength changes on the picometer scale. I was able to prevent lock breaks during measurements by warming up the Ti:Sa sufficiently and preventing mechanical shocks to the laser table.

Phase noise

Our measurement of the atom fraction ϱ is affected by two noise sources: projection noise and technical noise. When counting a finite number of atoms to determine the ϱ , we are subject to binomial statistics with $p = \varrho$, $q = (1 - \varrho)$, which limits the precision reachable depending on N :

$$\sigma_\varrho = \frac{\sqrt{Npq}}{N} = \sqrt{\frac{M(N-M)}{N^3}} \quad \Rightarrow \quad \frac{1}{2\sqrt{N}} \leq \sigma_\varrho \leq \frac{1}{N}. \quad (3.8)$$

This fundamental noise is joined by the technical detection noise in our system: the fluorescence counted on the EMCCD chip fluctuates. We can determine this by taking many images of a small numbers of atoms and observing the histogram of the resulting counts, which shows separated gaussian peaks for one, two or more atoms. As the number of atoms increases, the peaks grow broader and lose distinction at around 20 atoms. The fluctuations causing this broadening have two components: one is dependent on the square root of the number of counts and constitutes photon shot noise, which is again a projection noise. The other term is linear in the fluorescence and is technical, relating to chip readout[10]. For atom numbers that are much higher than ten, it becomes difficult to analyze the noise behaviour, precisely because the peaks lose separation. I will therefore not analyze my noise bottom-up like this, but top-down from the resulting phase data.

The long-term measurements shown above can also be used to quantitatively analyze our phase noise and stability, using the so-called Allan deviation [45]. This is an established tool for analyzing the stability of a frequency standard, by measuring how much adding more samples to a measurement reduces its noise. First, to measure phase in the most precise and efficient way, one would not sample full interference fringes, but instead only at one point: on the steepest slope of the flank with the strongest sensitivity $\partial_\phi n$. At this point, $\varrho = 0.5\gamma \approx 0.5$, providing the optimum binomial noise.

In a noise-free experiment, ϱ is subject to binomial statistics and by recording more and more samples, the deviation between different runs of the experiment should decrease with $\sigma_\varrho = 1/(2\sqrt{N})$, where N is the number of atoms sampled - this is the law of large numbers. Noise and drifts cause the experiment deviation to exceed this theoretical limit. To analyze how strong the excess it at which timescale, one uses the Allan deviation: a long series of samples is recorded and subdivided into blocks of N samples each. The mean value of each block is recorded and called ϱ_i ; then, the Allan deviation is computed:

$$\sigma_A(N) = \sqrt{\frac{1}{2} \langle \varrho_{i+1} - \varrho_i \rangle^2} \quad (3.9)$$

. This shows whether consecutive measurement series follow the law of large numbers. I have selected a point on the steepest slope from the second long-term measurement and analyzed the Allan deviation of ϱ for this point. Selecting one point out of fringe measurement is not a problem, since the Allan deviation depends on the number of samples taken instead of the measurement duration. Only if we want to make conclusions about timescales in the noise do we need to consider this detail.

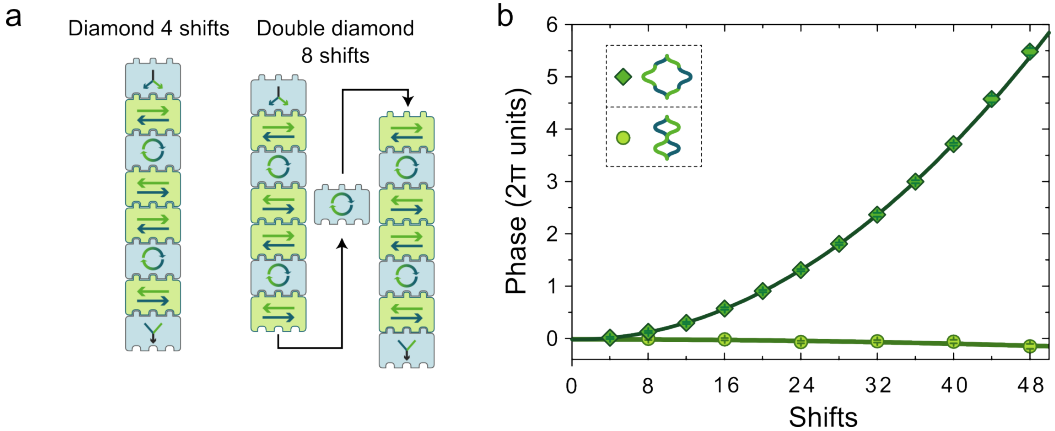


Figure 3.5: The phase recorded by diamond interferometers of increasing size increases quadratically, up to 35 rad for 48 shifts, equal to $10 \mu\text{m}$ separation. The behaviour can be precisely fitted based on the change in spacetime area, suggesting a state-independent potential gradient. A double diamond geometry records almost no phase accumulation, suggesting almost complete cancellation of the effect by the "spatial spin echo" of the double diamond.

The resulting Allan deviation is shown in fig. 3.4b: as we can see, it is running slightly above the theoretical limit, indicating that our system experiences either phase noise or noise in atom detection. Coming from only one time series, the deviation data is itself noisy, which explains why points can fall under the theoretical limit. One can see that for larger numbers of atoms sampled, the points begin to fall further away from the limiting curve, indicating that drifts are affecting the long measurements. The bump at 200 atoms sampled may be due to fluctuations on a specific time scale, in this case about 3 minutes. At that timescale, the air conditioning is a possible culprit. Nonetheless, this performance is fully satisfactory for our measurements.

Translating the deviation of ϱ into phase happens by dividing the error in ϱ by the sensitivity $\partial_\varphi \varrho$ of the interferometer[5]. For maximum sensitivity, ϕ_{MW} should be set so that ϱ is measured on the flank of the interference fringe. The slope at the steepest flank is $\partial_\varphi \varrho = \gamma \times C/2$: a poor contrast of the interferometer reduces the phase sensitivity.

3.2.2 Light shift gradient

To characterize the behaviour of the interferometer in our system, we observe the phase while changing the size of the interferometer. Size can be measured in the number of shift operations applied; my convention is to count the total number in the sequence, without counting the left and right arm separately.

The evolution of phase vs. the number of shifts in a diamond geometry is shown in fig. 3.5. A parabolic behaviour is immediately apparent, reaching over 40 rad of phase. We have explored a number of scenarios for this be-

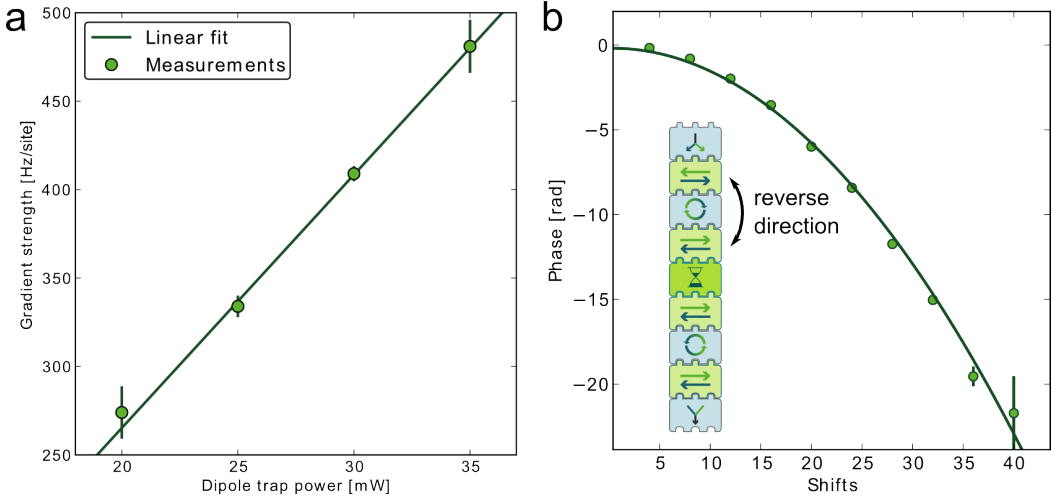


Figure 3.6: **a** The gradient strength calculated from parabolic fits (given in detuning per site) for different dipole trap powers. For each setting, transport was independently optimized. The fit is linear and passes through the origin, identifying light shift as the effect recorded. **b** The diamond interferometer opened in the other direction (possible by EOM realignment) produces the same magnitude of phase accumulation with the opposite sign. Note that the shift operation blocks are sorted differently from fig. 3.5.

haviour, including a stray magnetic gradient or a tilt of the lattice leading to gravitational effects [10]. The parabolic behaviour indicates the presence of a linear potential gradient which affects both spin states equally, which excludes magnetic fields.

An extended search was performed for possible sources; eventually we were able to clearly identify a gradient in the lattice light shift as the cause. The gradient results from a divergence of the lattice laser over the experimental region, which varies the total light shift of about 700 kHz proportionally to intensity. Based on our model in eq. 3.5, a potential gradient of $h \times (324.5 \pm 0.8)$ Hz/d has been detected, with d the lattice spacing. I investigate whether such a gradient can be produced by a displacement of the lattice beam focus from the imaged region and calculate the intensity gradient for a gaussian beam of $w_0 = 30 \mu\text{m}$, $z_R = 3.2 \text{ mm}$ and $U_0 = 1.6 \text{ MHz}$. The result is that a gradient of the correct magnitude can occur at an axial displacement of about $600 \mu\text{m}$ from the focus and that the change in intensity is approximately linear over the experimental region of $40 \mu\text{m}$. The gradient produced in this manner is state-symmetric, because the polarization of both lattice beams is aligned to minimize differential light shift and thus state-asymmetry.

Several measurements together give solid proof that the light shift is indeed responsible for the accumulated phase. First, I have measured interferometers at different lattice powers, from 20 to 35 mW; for each power, the lattice ramp duration must be redetermined due to the change in trap frequency. As light shift is proportional to intensity, the gradient resulting

from the model should be proportional to the beam power. The resulting parabolas are fitted to extract gradient strength and the result is clear: the linear behaviour is as expected (see fig. 3.6a).

Second, the double diamond will not accumulate phase from constant potential gradients. As the data in fig. 3.5 shows, the phase accumulated is orders of magnitude lower and in fact, of opposite sign. I believe that the sign inversion is due to defects in the cancellation arising from dephasing. This measurement proves that the gradient is time-independent, which would not be the case for electronic drifts during the sequence (for example, capacitative charge buildup in the EOM or low-pass effects).

A third piece of evidence is that switching transport direction inverts the accumulated phase. We can switch the direction by realigning the EOM to swap the crystal axes, which changes the sign of the lattice phase change φ . This causes the qubit states to be exchanged between the two arms of the interferometer and changes the sign of A , as visible in fig. 3.6b. The gradient recorded is $h \times (-328 \pm 4) \text{ Hz/d}$, compatible with the previous gradient and less precise because of a shorter measurement. This demonstrates that the phase observed results from a spatial effect, and not from a non-linearity in shifting or a variation of lattice depth. The magnitude of the gradient from all measurements is tabulated in table 3.1.

Hold time

The final geometry that will be demonstrated is a diamond with hold time. Opening the interferometer and pausing for a certain time allows us to sample the potential difference between two constant atom positions for a freely variable time. This is an ability unique to trapped interferometers; neither atomic beams nor fountains can achieve anything comparable. The benefit is to collect phase for a prolonged time while the atom is stationary. The upper limit is posed by the coherence time, as the normal dephasing mechanisms are active. To extend the time available, spin echo can be applied during the hold time, so that the full homogeneous coherence time can be utilized. Spin echo symmetrizes the hold time with respect to the spin states, meaning that state-asymmetric effects will be cancelled.

Table 3.1: Gradient strengths recorded in the different measurements. The single diamond delivers the most precise measurement with the most atoms sampled. The reversed diamond confirms that it is a spatially fixed effect and not a phase arising from our shifting operations. The hold time with spin echo confirms again the complete independence from shifting but more significantly the state-symmetry of the effect.

Measurement	$h \times$ Gradient [Hz/d]	Standard deviation [Hz/d]
Single diamond	324.5	0.8
Reversed diamond	-328	4
Hold time with spin echo	324	7

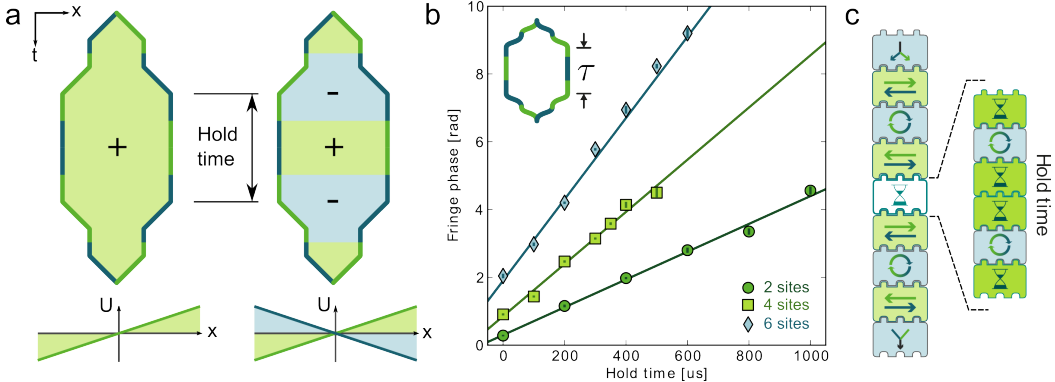


Figure 3.7: **a** Illustration of the behaviour of the spacetime area for interferometers with hold time and spin echo during hold. For state-symmetric gradients (left), the state switches can be neglected and area increases linearly with hold time. For state-dependent gradients (right), the spin echo series causes an alternation of sign, which cancels to zero for state-antisymmetric effects. Note that any combination of linear potentials can be decomposed into one symmetric and one antisymmetric contribution. **b** The phase accumulated during a hold time at 2, 4, or 6 lattice sites separation, plotted vs. the duration of the hold time. Spin echo is implemented with two echo pulses spaced in the hold time, cancelling all state-dependent effects. A linear phase accumulation quantitatively confirms the potential gradient due to lattice laser divergence. The calculated gradient strength is $h \times (324 \pm 7) \text{ Hz}/d$.

The measurement is a diamond interferometer opened to 2,4 and 6 lattice sites separation with a hold time inserted at the maximum spreading. To extend the time available, two spin echo pulses are inserted with a 1:2:1 spacing in the hold time; using two pulses has the advantage that no additional spin flip has to be considered. The duration of the hold time is varied between 0 and 600 μs . We record the phase and subtract the value accumulated for no hold time, leaving only the phase gathered during the hold, expected to be $\partial_x U \cdot \Delta x_{\max} \cdot \tau_h/\hbar$.

The phase behaviour visible in fig. 3.7 conforms to the expected linear behaviour vs. time, and the magnitude of the gradient is fitted to be $h \times (324 \pm 7) \text{ Hz}/d$, fully consistent with the value from fig. 3.5. This adds one more aspect to our lightshift model: it confirms that the phase accumulated is not related to the shift process. That the gradient can be recorded with spin echo also means that it cannot be state-antisymmetric.

In this way, our different geometries complement each other elegantly:

- The normal diamond is best for measuring the magnitude of a gradient.
- The double diamond shows whether the gradient is constant over the sequence.
- A hold time with spin echo shows whether the gradient depends on shifting and whether it is spin-symmetric.

For a linear gradient, together they deliver a very precise characterization.

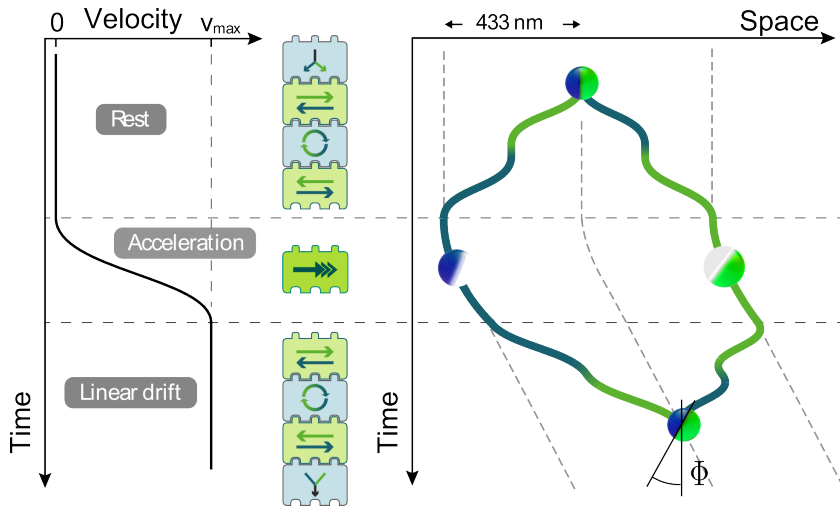


Figure 3.8: Schematic of the acceleration measurement in a diamond interferometer. The atom is split into two spatially separated paths, accelerated during a hold time, then rejoined while moving at a steady velocity. The phase accumulated stems from the linear potential gradient that an acceleration causes. The final displacement is small and no problem for measurement.

More complicated gradients can be dealt with in a similar manner, as the basic symmetry statements are still true, but the equations become more complicated.

The interferometer with hold time is less efficient than a diamond at gathering phase from a gradient, but it can be useful for measurements on the submicrometer scale, i.e., close to surfaces or nanostructures. The ability to keep the atom at rest with a position control better than 20 nm certainly has potential, but the data rate from a single atom is low and problems with the optical lattice near a surface must be solved.

3.2.3 External acceleration

Measuring local gravity is one of the main fields of precision interferometry and therefore a logical choice for demonstrating the measurement of deliberately applied external potentials. Since our lattice is horizontal, atoms cannot be split in the direction of earth's gravity. To produce a similar effect, the atoms can be split and then accelerated to produce a pseudopotential (see fig. 3.8), whose slope is $\partial_x U = m_{Cs} \cdot a$, where m_{Cs} is the atomic mass of Caesium and a the applied acceleration. It should be noted that this corresponds to the gravitational redshift if one considers the atom an accelerating clock with a frequency of $\omega = mc^2/\hbar$ [46]. As this frequency is extremely high, we can observe a sizeable redshift with accelerations around g .

There are several methods to apply accelerations, and moving the back-reflection mirror is the one with the least technical setup required. The phase of the lattice is pinned with respect to the mirror, so moving it by means of a piezo will cause a parallel movement of the atoms. Using a piezo

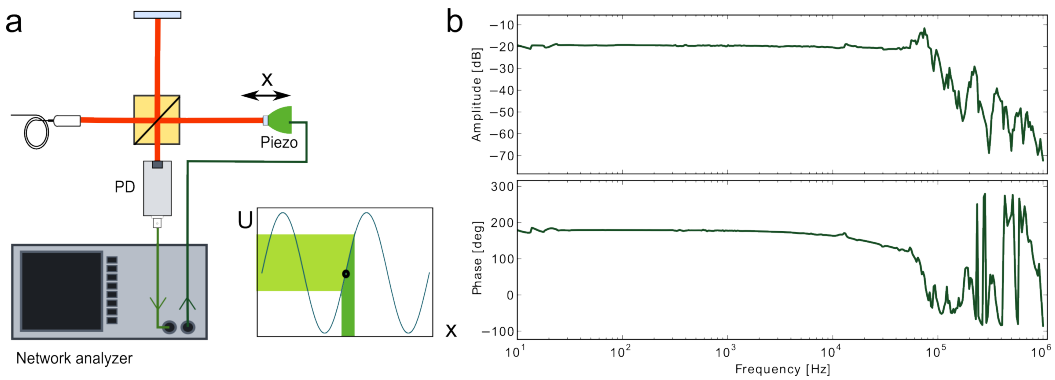


Figure 3.9: **a** Scheme for calibrating the piezo mirror in a Michelson interferometer. **b** Bode plots for a calibration of the self-built piezo mirror employed in the acceleration measurements. The first resonance is at 50 kHz.

limits total displacement (due to its breakdown voltage) as well as speed, as rapid movement will excite mechanical resonances of the piezo and its mounting. The mechanical resonances can be reduced and moved to higher frequencies. This means decreasing masses, introducing dampening and removing sharp transitions in elasticity (jumps in Young's modulus act similar to refractive index jumps). Following the techniques presented in [47], a small, thin mirror is combined with a small piezo and attached to a mirror mount with a hand-made holding rod. This rod has an outer shell of a soft steel, tapering towards the piezo to match the size of its endface. The interior of the rod is hollowed out and filled with soft soldering lead to introduce a dampening body which can absorb vibrations. Mirror, piezo, rod and mount are connected with epoxy glue.

To characterize the piezo mount, an optical Michelson interferometer is set up using a frequency-locked laser beam (see fig. 3.9). A network analyzer is connected to the setup with input to the piezo and output from the photodiode. The network analyzer applies a small modulation voltage with increasing frequency and determines amplitude and phase of the same frequency in the output signal, returning the complex frequency response function of the linearized system. To treat the interferometer as a linear system, the Michelson interferometer must be operated on the center of the fringe's slope, i.e., the path length difference Δx between the arms should be about $\lambda/4$, the modulation effect significantly smaller than that. After being set up on a breadboard, the interferometer's phase varies on the second time scale, likely due to thermal drifts and acoustic fluctuations. The interferometer can now be "locked" by human intervention: Pressing the breadboard corner down slightly increases Δx , so by observing the photodiode output on an oscilloscope, the interferometer can be stabilized. Care has been taken that this human servo loop does not qualitatively affect the measurements; slight deviation from the optimum Δx will only cause gentle changes in the frequency response, unlike mechanical resonances which produce many dB change in amplitude and corresponding phase features as

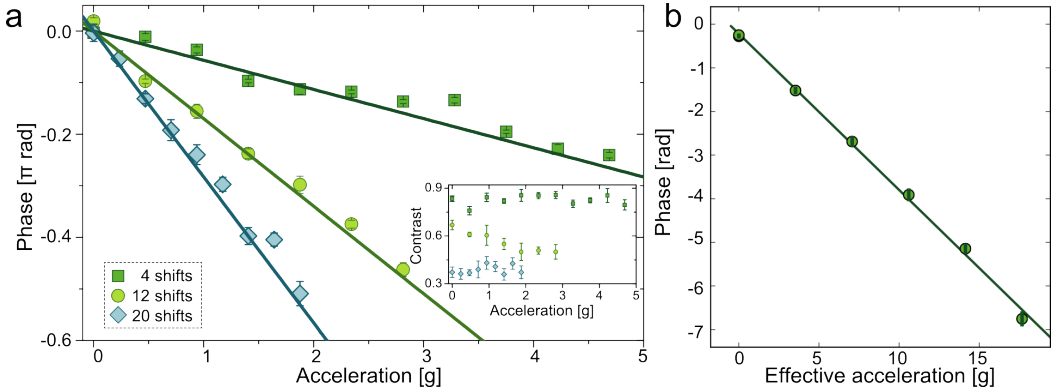


Figure 3.10: **a** The interferometer phase recorded vs. piezo acceleration for different separation of the paths. The expected linear behaviour is clearly visible, although the measured values scatter significantly more than their statistical error would suggest. Inset: Fringe contrast is constant for a given separation, indicating that motional excitation from the acceleration is not taking place. **b** Interferometer phase vs. acceleration using the DDS for acceleration. Data values are much closer to theory; remaining scatter is explainable by statistical error.

seen in fig. 3.9. Investigating different mirrors shows that resonances can be pushed to higher frequencies with decreasing piezo and mirror mass; the custom mount finally reaches the first resonance at 50 KHz. The scale of movement was calibrated in a DC measurement, using a slow ramp of piezo voltage and recording the interferometer fringe, which gives a sensitivity of 8.8(1) nm/V.

To perform the acceleration in a normal interferometer, a brief hold time without spin echo is inserted at maximum splitting. In that time, the piezo accelerates from standstill to the final velocity, which is maintained while the interferometer is closed and phase read out. To decelerate before the interferometer is closed would cancel out the accumulated phase. The doppler shift during the closing is negligible, as $v/c < 10^{-11}$. Nevertheless, the need to maintain the final velocity imposes a technical limitation: During the closing, the piezo voltage must continuously rise. The maximum acceleration that can be applied is thus limited by the maximum voltage available.

The phase accumulated by the interferometer due to acceleration is

$$\Phi_{\text{acc}} = \frac{\Delta x \cdot m}{\hbar} \cdot \int_0^\tau a(t) dt = \frac{\Delta x \cdot m \cdot v_f}{\hbar}, \quad (3.10)$$

where τ is the duration of acceleration, v_f the final velocity and Δx the splitting. This way of calculating the phase assumes that the atoms are not excited in any way, but only exposed to a linear potential gradient. To achieve this, $a(t)$ should be a smooth ramp, so a cut out of a sinusoid is inserted to match position and velocity at beginning and end of the acceleration. The proof that excitation is negligible is the interferometer's contrast (see fig. 3.10a inset), which stays constant for different accelerations and varies only based on the number of shifts.

Measurements were performed with an acceleration duration of $50 \mu\text{s}$ and splitting of up to 10 lattice sites. The data plotted in fig. 3.10 show the expected linear behaviour and match the predicted phase well. An offset arising from the different opening and closing sequences for different sizes has been fitted and subtracted, leaving only Φ_{acc} . Although the precision is acceptable for a proof-of-principle measurement, there is a problem: several points are more than three sigma away from the fit, making the χ^2 very poor. The most likely explanation is that the mirror is not an accurate method of applying acceleration, likely due to either excitation of the resonance at 50 kHz or a sensitivity to environmental conditions.

The optical conveyor belt that is installed for quantum walks measurements (see 2.2.3) can accelerate atoms with much greater accuracy. One of the checks performed for the new setup was an interferometer with acceleration as described before, except that the acceleration is delivered now by the conveyor belt. Also, as required for the quantum walks, the acceleration is not applied at once with varying strength, but in a number of discrete boosts that all have the same strength. The phase accumulated is then proportional to the number of boosts, since for n boosts we have $v_f(n) = n \cdot v_f(1)$. The results are plotted in fig. 3.10b: now, the scatter is limited by the statistical error of the data points, which is the preferred situation. Contrast is not shown but is constant.

Our phase measurements are a good demonstration of the interferometer's capabilities, resolving a potential gradient with a relative precision of $2 \cdot 10^{-4}$. Most importantly, we can gather information about gradients from very different angles, delivering a complete picture of the gradient's properties with multiple crosschecks.

3.3 Measuring contrast

Next to the phase, fringe contrast is the second output of an interferometer. All effects discussed in 2.2.4 also apply to interferometers; coherence is on the one hand significantly extended by the repeated π pulses for multi-site shifting, which double as spin echo pulses. On the other hand, shifting also introduces new effects that significantly reduce the contrast decay time, namely acceleration, lattice wobble and phase jitter. More effects arise from the atoms being spatially separated

3.3.1 Contrast decrease from shifting

The acceleration applied during state-dependent shifting is significant: the voltage ramp delivered to the EOM driver is linear and proportional to displacement, meaning that acceleration at beginning and end is in theory infinite and in practice as strong as the EOM driver (bandwidth 200 kHz) can deliver. The atoms reach the final velocity of one lattice site per $20 \mu\text{s}$, or 24 mm/s, within about $2 \mu\text{s}$, giving a peak acceleration of about 1200 g. As stated before in section 2.3.1, strong motional excitation can only be avoided by correct selection of the ramp duration.

In fact, the initial acceleration at the beginning of each shift does excite the atom to different motional states; the only way to cancel this is to achieve complete de-excitation with the final deceleration, which is possible if the deceleration is applied with correct timing: an oscillator excited from a kick can be brought back to rest by second kick at the correct instant. In a strict treatment, each transport step should therefore be considered as a multi-path interferometer. We nonetheless avoid this because any phase that might be accumulated in one shift will be accumulated at another shift with opposite sign due to the symmetry of the trajectories.

Motional excitation by the shift can be detected by an equal decrease in contrast. If a fraction of the atom is excited from the motional ground state to the first excited state, it will rapidly accumulate phase from the 120 kHz difference in trap depth and will quickly dephase completely. By analyzing the decay of contrast in the interferometer data, I will later show that motional excitation is certainly below 2% per step (see table 3.2).

The second effect arising from the shifting process is an increase in dephasing because of the elevated differential light shift during shifting. In fact, the lightshift is many times higher than for overlapped sublattices, due to the 7:1 admixture of the other chirality the $|F = 3, m_F = 3\rangle$ state experiences. The formula from 2.2.4 shows that $\varphi = \pi/2$ leads to a differential light shift of $U_0/4$, normally about 400 kHz. Averaged over the transport step, this still amounts to 200 kHz. Since normal dephasing occurs with a mere 20 kHz differential light shift, during transport it should be amplified tenfold. Fortunately, the high rate of spin echo pulses during the interferometer will still act as a high pass filter on dephasing.

The third effect produced by the shifting process itself are aftershocks in the polarization angle due to resonances in the EOM. As KD*P is a piezomechanical crystal, the voltage ramp creates mechanical shocks, which excite resonances in the crystals of the EOM. Despite constructive measures to suppress the resonances by damped mounting, brief aftershocks are visible on photodiode signals after a voltage ramp, lasting for less than $2\ \mu\text{s}$. As each crystal resonates individually, it cannot be assumed that this is only a modulation of lattice phase, but can also extend to changing the power balance between the chiralities. Also, the polarization effect is from experience not the same for each repetition and thus is not cancelled out completely by spin echo.

3.3.2 Contrast decrease from separation

Beyond the effects of the shifting process itself, a spatial separation of the spin states also introduces new mechanisms for contrast decay.

The most significant one (compare table 3.2) is a failure of paths to meet at a common site for the final join operation. The effectiveness of the microwave π pulses for multi-site shifting is finite, and the affected atoms deviate from the intended path because their spin state is not flipped. With high probability, they do not have an interference partner of the opposite state at their final site and do not contribute to the fringe at all, reducing the contrast.

The reduction in contrast can be estimated: if the probability of a successful state switch is p , then the contrast after n steps is $C_0 \cdot p^{2n}$. The factor of two arises from the need to successfully invert the state of both arms each step. These "deviant" paths can still achieve interference by two mechanisms: paths that drop towards the inside of a diamond shape can rejoin the returning trajectory if a second flip error happens, making the probability for this proportional to p^2 . Furthermore, two deviant paths can meet at a lattice site that is not the primary target; consideration of the geometry shows that this requires three spin flip errors because the two deviant paths must come from opposite directions to the secondary site, having opposite spin state. The trouble with deviant interference is that the phase is different from that of the main interferometer. If some atoms produce their own interference fringe with a different phase, they decrease contrast and skew the phase detected overall.

In principle, since the deviant trajectories are fully coherent, we need to treat the sequence as a quantum walk with a coin angle close to π (or 0 if one does not consider alternating shifts, see fig. 4.3). Practically, this is unnecessary because for p near unity almost no interference takes place away from the main site.

Separation can also contribute to dephasing if the paths still meet in the end; just like differential light shifts can fluctuate, so can potential gradients. The position-dependent phase accumulated can vary over several repetitions of the experiment, leading to a blurring of the recorded fringe. For light shift gradients due to focussing, this is not a major issue, as they are extremely stable. Inertial force gradients applied by, e.g., piezo mirrors, can suffer depending on the reproducability of the acceleration, just as magnetic field gradients might fluctuate due to current noise. Our acceleration measurements do not show significant contrast reduction from the acceleration (see fig. 3.10), indicating that this effect is minor.

3.3.3 Data analysis

Data for contrast decay has been accumulated for diamond and double diamond interferometers, as well as for a diamond with hold time. The most significant dataset is that of the single diamond of varying size, see fig. 3.11a. The data show an exponential decay vs. the number of steps taken, extrapolating to unity for zero steps and decreasing at a rate of 0.6% per shift. We have independently quantized the homogeneous decoherence time without shifting and the fidelity of π pulses during shifting sequences. The homogeneous decoherence time T_2^* of course must be measured for the same number of spin echo pulses in the same timing as during an interferometer sequence. The results are plotted in fig. 3.11a as the dashed line, showing a very good coherence time > 2 ms that is far from limiting interferometer performance.

Apart from the normal spin decoherence, the interference contrast also suffers a known reduction due to the limited spin flip fidelity: we have independently characterized this by shifting atoms by up to 100 steps (see fig. 2.11) and found 99.0% effectiveness per step. The contrast decay from

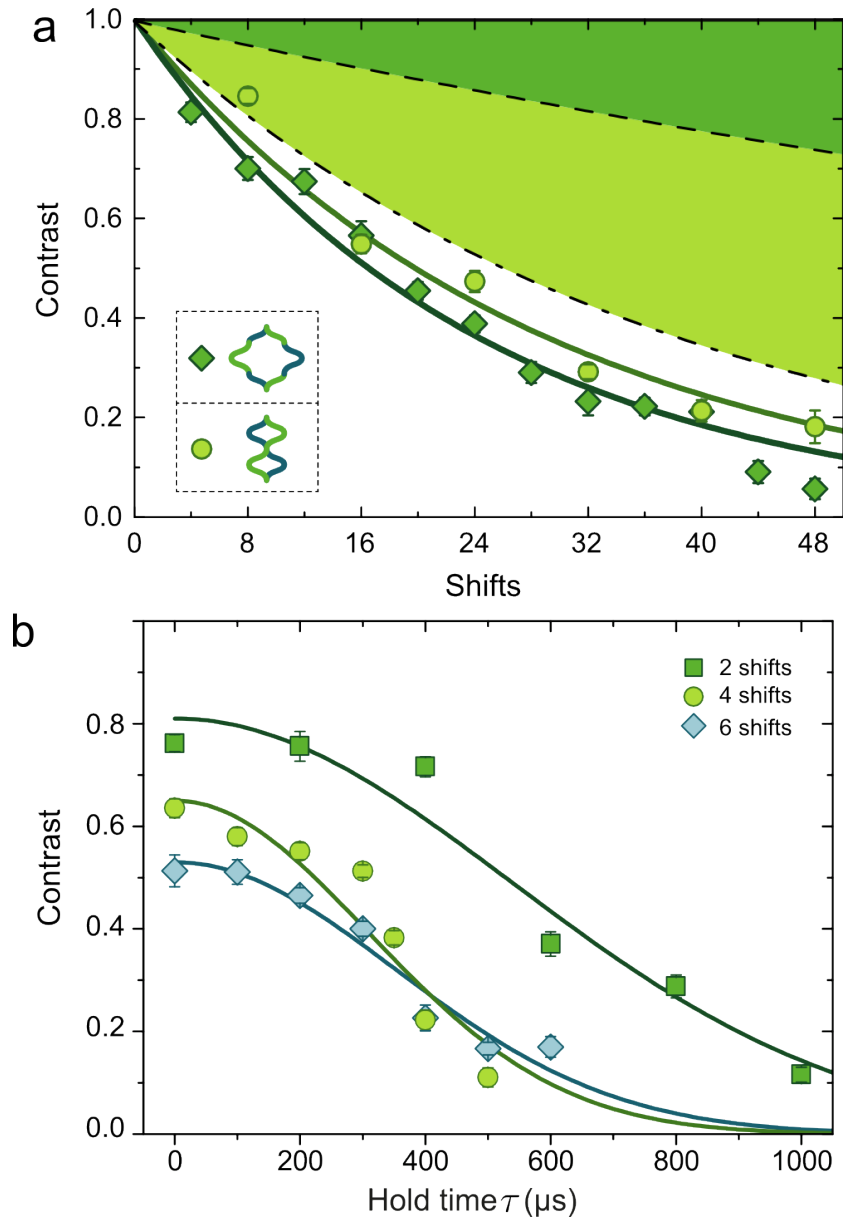


Figure 3.11: **a** Contrast results for single and double diamond geometries vs. the number of shifts, with exponential fits. The shaded areas show the measured contribution of two known contrast reducing effects: Shift-independent spin dephasing (dark green) and contrast decay due to finite shift fidelity (light green). The remaining contrast decay can not be resolved further and comes from a combination of other effects. **b** The contrast of a diamond with hold time shows the normal gaussian behaviour for homogeneous decoherence [26]. The time constant is comparable to that of unshifted atoms.

this phenomenon follows the formula named above; multiplying it onto the contrast without shifting results in the dash-dotted line, accounting for most of the contrast decay. The two understood mechanisms and the total decay rate are listed in table 3.2. I have chosen to list the contributions in dB because this is convenient for multiplicative factors. Remarkably, the remaining decoherence that could stem from a third mechanism is smaller than its own errorbar - to investigate decay mechanisms further, we need to increase the precision of the contrast measurements.

The other mechanisms that were discussed above could therefore not be identified separately, meaning that the possibly remaining decoherence contribution (1.7% per shift) could be split between transport excitation, polarization jitter and gradient fluctuations. Gradient fluctuations can still be analyzed individually by looking at the contrast of the double diamond geometry. This geometry has the ability to rephase gradients in first order, meaning that decoherence from slow gradient fluctuations should be suppressed significantly. The contrast decay is indeed slightly slower, but the difference is quite small. One can conclude that gradient fluctuations are a minor contribution if any.

Let us finally compare the results for hold time interferometers; these should suffer from contrast decays due to separation and fluctuating trap depth, but not due to shifting effects. The applied spin echo also cancels the contribution from state-dependent effects (gradients or global) in first order.

The behaviour visible in fig. 3.11b confirms several expectations: The contrast decays vs. hold time as a gaussian function, as expected [26]. Note the difference to fig. 3.11a, in which contrast decays exponentially. This is due to the different x-axes in the two plots: Contrast will decay in a gaussian fashion vs. time, but exponentially vs. the number of echo pulses. Decay times in fig. 3.11b are fully consistent with the behaviour of unshifted atoms, indicating that once at rest, atoms behave in the normal manner - being split does not speed up decoherence significantly, as no strongly fluctuating gradients are applied.

To summarize, contrast in our interferometer behaves in a well-understood fashion: it is dominated by the spin flip errors occurring at each transport

Table 3.2: Tabulation of the decay sources identified in the diamond interferometer. Contrast starts from 1 and decreases per step; phase can be detected until about 10% contrast. Note that given the uncertainty on the total decay, we cannot be sure that our two identified mechanisms do not describe the decay entirely (i.e., others becomes zero).

Mechanism	Decay contribution [dB/step]
Total	-0.19 ± 0.01
Stationary dephasing	-0.026 ± 0.004
Spin flip defects	-0.17 ± 0.02
Others	-0.01 ± 0.02

step, while normal spin dephasing is of secondary importance. The other contrast decay mechanisms cannot be experimentally separated. The overall performance is fully satisfactory, allowing us to reach splittings of about $10\text{ }\mu\text{m}$ and interferometer durations of about 1 ms.

In conclusion, the interferometer measurements have demonstrated our successful control over delocalized atoms. We have extracted phase information from atoms that were split over up to $10\text{ }\mu\text{m}$ and modified the interferometer's geometry to identify and separate different effects. The benefit lies in the validation of our toolkit approach to coherent trajectory design and a greatly increased understanding of our system, in particular the dephasing mechanisms.

4 Quantum walks

4.1 Introduction

Quantum walks are the quantum mechanical analog of classical random walks. Classical random walks are applied in such different fields as information science [48], fluid dynamics [49] and biology [50], but the model can be quickly described: the walker takes a stochastical decision (e.g., tosses a coin) and based on the outcome, moves in a certain direction. The core process is repeated as often as desired, and the resulting walker movement possesses rich dynamics [51].

The principle can be adapted to quantum mechanics, and the quantum walker is capable of interference, superposition, and entanglement, as well as using quantum states for the decision process, e.g., the internal spin states of a particle. Quantum walks were first presented in 1993 [52] and quickly singled out for their remarkable spreading properties in position space. Classical random walks spread diffusively - the RMS spread of the probability distribution after n steps of the walk is $\propto \sqrt{n}$. This speed fundamentally bounds diffusion [43], random search algorithms and many other phenomena. Quantum walks, in contrast, spread ballistically ($\propto n$) [9]. It has been demonstrated that leveraging quantum walks can drastically speed up search algorithms [53], meaning somewhere between polynomial to exponential speedup [9]. Several publications have proposed quantum walks occurring in plants as part of the photosynthesis mechanism, to speed up the transport of excitons in protein complexes [54]. The intense theoretical study has revealed further applications, in particular, as a sufficiently powerful primitive for universal quantum computation [55], which means that whoever implements a well-controlled quantum walk has a working quantum computer. Finally, and of the most relevance for us, quantum walks in lattices can mimic features of other periodic systems, amongst others electrons in solids (see 4.2.2).

Experimental quantum walks began in 2009 with a breakthrough in our experiment [56], demonstrating the first quantum walks, and reproducing the hallmarks ballistic spreading and unitarity. Several alternative realizations were presented quickly afterwards, based on photons in freespace [57] or in waveguides [58], or on ions in phase space [59]. Since then, the experimentally possible number of steps has been increased and even a two-dimensional walk has been realized [60].

In our laboratory, we have been working towards the long-term goal of simulating complex quantum system with quantum walks. In the present chapter, we will use quantum walks to mimic the behaviour of a charged particle in a lattice while under the influence of an electric field. The following is the first simulation of another quantum system by quantum walks

with neutral atoms.

4.2 Theory

4.2.1 Spreading

A quantum walk is a repetitive two-step process: Coin and shift, repeat. The first cycle splits the initially localized atom over two sites, the next over three and so forth. From the second step onward, quantum paths meet and interfere, producing the distinguishing features of the quantum walk. For our atomic quantum walks, the coin is an operator \hat{C} on the Hilbert space of the spin \mathbb{C}^2 , implemented by microwave operations as in 2.2.4. The Hadamard coin \hat{C}_H (see eq. 4.1) is generally considered the standard coin. It is "fair", meaning it splits a pure state into a 50:50 superposition.

The most general coin for a microwave operation is given by $\hat{C}_{\theta,\phi}$ (see eq. 2.1) and cannot implement \hat{C}_H . We are therefore implementing \hat{C}_B instead:

$$\hat{C}_H = \frac{1}{\sqrt{2}} \begin{pmatrix} 1 & 1 \\ 1 & -1 \end{pmatrix}, \quad \hat{C}_B = -\frac{1}{\sqrt{2}} \begin{pmatrix} 1 & -1 \\ 1 & 1 \end{pmatrix}, \quad (4.1)$$

which is also a fair coin and equivalent to \hat{C}_H .

The shift operation, here termed \hat{S}_+ and \hat{S}_- , is a movement to a neighboring lattice site, whose direction is defined by the spin state. Our experimental implementation of the shift operator requires the sign to alternate from one shift to the next (see 2.2.1).

$$\hat{S}_\pm = \begin{cases} |\uparrow\rangle \otimes |x\rangle \longrightarrow |\uparrow\rangle \otimes |x \pm \frac{1}{2}\rangle \\ |\downarrow\rangle \otimes |x\rangle \longrightarrow |\downarrow\rangle \otimes |x \mp 1\rangle \end{cases}. \quad (4.2)$$

The mathematical framework and our experiment data number the lattice sites in different ways: our experimental shift moves each atom by $\lambda/4$, which is half a site of the optical lattice. This is because for $\varphi = 2\pi$, our lattice is offset from its normal spacing by $\lambda/4$, creating a temporary lattice site between two normal ones (each sublattice is shifted by π , see fig. 2.4b). The mathematical framework specifies the distance of each shift as one site and can thus work in a constant lattice geometry. I will follow the latter convention in the theory and in numerical calculations, meaning that the lattice spacing shown in these graphs is $\lambda/4$. In the experimental data, I will count sites of size $\lambda/2$, as natural for optical lattices.

Combining the two shifts and the coin produces the full walk operator \hat{W} :

$$\hat{W} = \hat{S}_- \cdot \hat{C}_B \cdot \hat{S}_+ \cdot \hat{C}_B, \quad (4.3)$$

applying it n times to an initial state produces an n -step quantum walk. Common initial states for a quantum walk are a single localized atom in either $|\uparrow\rangle$ or in $(|\uparrow\rangle + i|\downarrow\rangle)/\sqrt{2}$. The resulting evolution of the probability distribution is simulated numerically and is shown in fig. 4.1. Its most striking feature is the presence of clear peaks which move with constant velocity in position space. The walk starting from an initial pure state has one peak (going right

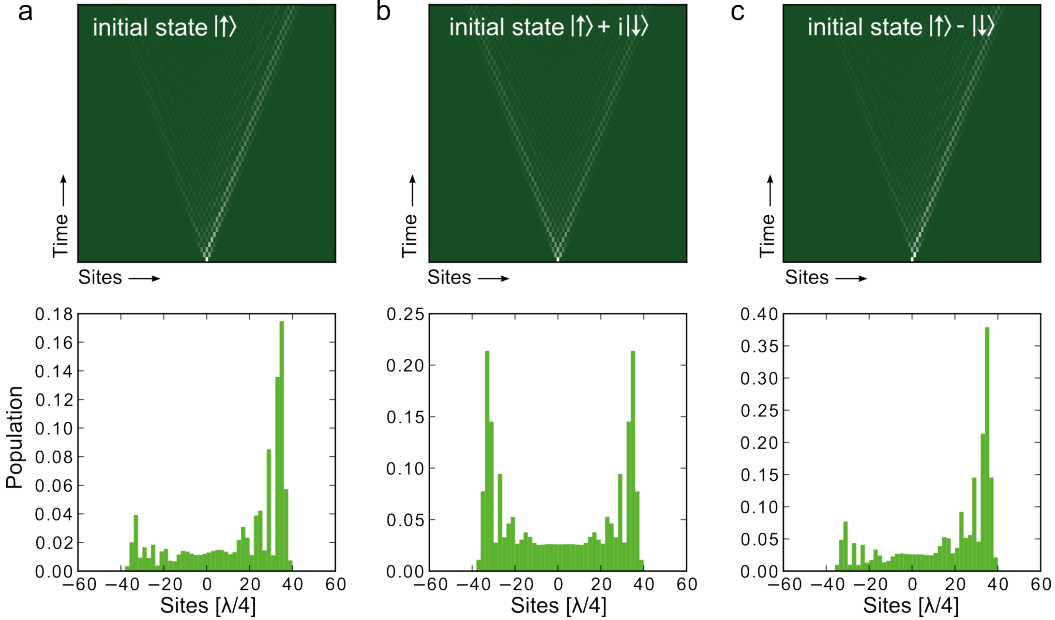


Figure 4.1: The spreading of the quantum walk with balanced coin \hat{C}_B simulated for different initial states. Shown are the occupation probabilities evolving for 50 steps and the final distribution. The linear spreading is clearly visible. **a** The pure $| \uparrow \rangle$ state, spreading quickly to the right side. **b** The symmetric $| \uparrow \rangle + i| \downarrow \rangle$ superposition leads to a double peaked structure because the real coin does not mix the two independently proceeding walks. **c** In contrast, the superposition $| \uparrow \rangle - | \downarrow \rangle$ on the right interferes strongly, leading to a stronger single-peaked walk.

for $| \uparrow \rangle$, left for $| \downarrow \rangle$) and the one starting from a superposition has two of half the height.

In the superposition listed above $| \uparrow \rangle$ has real amplitude and $| \downarrow \rangle$ has imaginary amplitude; the coin \hat{C}_B is real and does not mix the two, leading to two non-interacting walks from one initial site (see fig. 4.1b). If the amplitude of both states is real, strong interference occurs, as shown in the rightmost plot, leading to a completely different final distribution (see fig. 4.1c).

This comparison illustrates a key property of quantum walks: quantum walks from different initial states do not converge to a common limiting distribution, as a classical random walk would. Instead, the unitarity of the walk operator ensures that the walk can always be reversed to the initial condition [56], barring decoherence.

Apart from the initial state, the other parameter controlling the quantum walk is the coin; our microwave operations can be tuned in phase and rotation angle on the Bloch sphere. Changing the overall phase of the coin only matters in relation to the initial state, but changing the rotation angle impacts the walk strongly. If the coin angle approaches π , the walk will become a coherent transport as seen in the interferometer (see fig. 3.1), in which case the atom stays fully localized at one site but moves one site per walk operator. On the other hand, a coin angle of 2π will leave the atom

unmoved in the original site.

4.2.2 Quantum walks in the Brillouin zone

Quantum walks were named above as possible quantum simulators, but their behaviour in position space may not indicate why. By moving the analysis to k -space, it becomes possible to equate the walk itself with a particle moving in Bloch bands. The Fourier transformation shifts the discussion from the discretized periodic position space of the lattice to the continuous quasimomentum space of the Brillouin zone [61, 62]. Note here that we are defining k as the quasimomentum on a lattice of spacing $\lambda/4$. The coin operator is unaffected, but the shift operator takes on a different form:

$$\hat{S}_{\pm k} = \mathbb{I}_k \otimes \left(e^{\mp ik} |\uparrow\rangle\langle\uparrow| + e^{\pm ik} |\downarrow\rangle\langle\downarrow| \right). \quad (4.4)$$

The shift is now diagonal on momentum space, due to the fact that momentum states are translation-invariant, which means that the entire walk operator becomes diagonal on the momentum space:

$$\hat{W}_k = \mathbb{I}_k \otimes \left[\begin{pmatrix} e^{ik} & 0 \\ 0 & e^{-ik} \end{pmatrix} \hat{C}_B \begin{pmatrix} e^{-ik} & 0 \\ 0 & e^{ik} \end{pmatrix} \hat{C}_B \right]. \quad (4.5)$$

To simplify the system, we ignore the alternating shift sign for now and idealize the walk operator:

$$\hat{W}' = \hat{S}_+ \hat{C} =: e^{i\hat{H}_{\text{eff}}t/\hbar}. \quad (4.6)$$

Fortunately, this simplification is possible: as studied in [22], it only leads to a shift in k -space of π , which in position leads to a mirror inversion $|x\rangle \rightarrow |-x\rangle$. Because \hat{W}' is a time evolution operator, it can be connected to an effective Hamiltonian as in eq. 4.6. Diagonalizing the Hamiltonian gives us the eigenstates and energies of the walk. These states and their energies are the quantum system that is being simulated by our atoms.

The resulting eigenenergies of the simplified operator are [22]:

$$E_{\pm} = \pm \hbar \arccos \left[\cos k \cdot \cos \frac{\theta}{2} \right]. \quad (4.7)$$

The diagonalization shows that the walk possesses two energy bands with a shape tunable by coin angle θ . The movement of the k -states in position space can be calculated using the group velocity in the two bands $v_g^{\pm}(k) = \hbar^{-1} \partial_k E_{\pm}$. We will later use two symmetries of the group velocity:

$$v_g^{\pm}(k) = -v_g^{\pm}(k + \pi) \quad \forall k, \quad v_g^+(k) = -v_g^-(k) \quad \forall k, \quad (4.8)$$

in calculating the spreading of electric quantum walks.

The eigenstates of the walk operator can be described on the Bloch sphere using the latitude ϑ and the longitude φ :

$$\vartheta = 2 \arctan \left(\frac{\tan \frac{\theta}{2}}{\sqrt{\tan^2 \frac{\theta}{2} + \sin^2 k + \sin k}} \right), \quad \varphi = k + \frac{\pi}{2}, \quad (4.9)$$

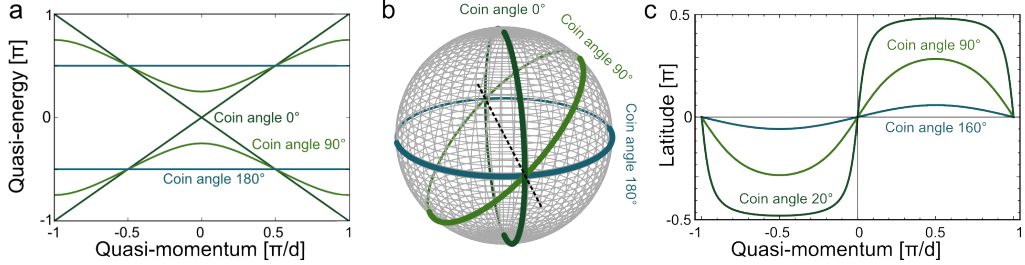


Figure 4.2: **a** The two bands of a quantum walk for different coin angles, showing the influence of coin angle on group velocity (cmp. eq. 4.11). **b** The spin composition of the eigenstates of the walk on the Bloch sphere. The state moves along the circle as k is varied; changing the coin angle θ tilts the circle around the hinge axis. The two bands are always opposing vectors due to their orthogonality. **c** The latitude on the Bloch sphere corresponding to one eigenstate for different k . Notice that for $\theta = 0$ the state remains at the poles, only jumping at $k = 0$ and $k = \pi$: the pure spin states are eigenstates no matter of their momentum.

or alternatively in cartesian coordinates:

$$\begin{pmatrix} x \\ y \\ z \end{pmatrix} = \frac{1}{\sqrt{\sin^2 k + \tan^2 \frac{\theta}{2}}} \cdot \begin{pmatrix} -\sin k \tan \frac{\theta}{2} \\ \cos k \tan \frac{\theta}{2} \\ \sin k \end{pmatrix}. \quad (4.10)$$

For every k , there is a different linear combination of the two spin states to create the two walk eigenstates in a linear combination (see eq. 4.9). The walk eigenvectors trace out a circle on the Bloch sphere for k going from $[-\pi.. \pi]$; this circle is tilted with regard to the axes of the Bloch sphere at an angle depending on the coin angle (see fig. 4.2). The orthogonality of the bands requires that the eigenvectors on the Bloch sphere point in opposite directions.

The coin angle θ can be varied to change band curvature and the tilt of the eigenvector circle. The bands that are approximately sinusoidal for a balanced coin move towards the two linear extrema: For $\theta = 0$, the bands are sawtooth-shaped; for $\theta = \pi$, they are flat and level. This behaviour is intuitive, for the band slope at any k determines the group velocity of that state. Ignoring the alternating shift sign, a coin angle 0 means a constant linear transport of the atom, obviously corresponding to a k -independent steep slope. On the other hand, a coin angle of π causes the atom to move back and forth between two sites, with zero group velocity - a flat band. The position space behaviour is simulated for several angles in fig. 4.3. In the experiment, the behaviour is shifted in θ by π because of the alternating shift sign, so that $\theta = 0$ is the resting atom and $\theta = \pi$ is the moving one. The formula for the group velocity is [22]:

$$v_g^\pm(k) = \frac{1}{\hbar} \partial_k E_\pm = \pm \frac{1}{\hbar} \frac{\cos \theta / 2 \sin k}{\sqrt{1 - \cos^2 k \cos^2 \theta / 2}}. \quad (4.11)$$

Since we cannot yet produce individual k states in our experiment (see 4.4),

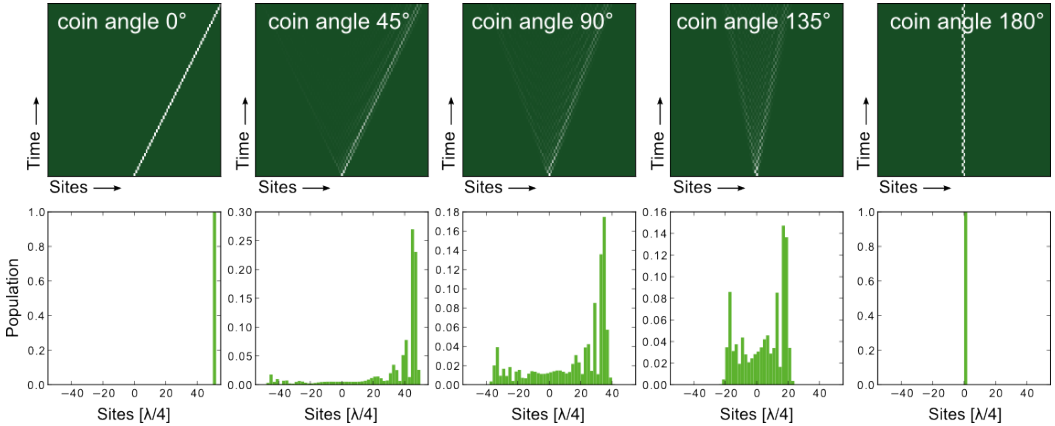


Figure 4.3: Simulated spreading and final distribution of a 50 step quantum walk from the initial state $|\uparrow\rangle$. The coin angle θ is varied from 0° to 180° , shifting across the whole range from full transport to balanced walk to stationary atom.

we observe an averaged spreading, given by the RMS of the position distribution. The corresponding spreading speed is

$$v_{\text{RMS}} = \sqrt{\frac{1}{2\pi} \int_{-\pi}^{\pi} v_g^2(k) dk} = \sqrt{1 - \sin \theta / 2}. \quad (4.12)$$

The effect of the coin angle on the eigenvectors can be visualized more easily than the effect on energy: the eigenvector circles tilts as on a hinge on the equator crossing: For $\theta = \pi$, it fills the equator, for $\theta = 0$, it stands vertical like a meridian. Again, this can be connected to the limiting cases: The full transport moves $|\uparrow\rangle$ and $|\downarrow\rangle$ in opposite directions without intermingling, making them eigenstates of the walk with opposite k . The eigenstates on the Bloch sphere collapse to the poles because no superposition can be an eigenstate anymore (see fig. 4.2c). A walk with coin angle π doesn't move atoms, but continuously applies spin rotations that image the equator plane of the Bloch sphere onto itself - naturally, all eigenstates must reside there. The hinge axis of the eigenstate disk depends on the microwave phase ϕ and can be rotated around on the equator of the Bloch sphere.

The Fourier picture gives access to the eigenstates and group velocities of the ideal walk. For us, this picture of the walk provides a tunable band system with fine control over experimental parameters and precise readout. But just as we cannot create k -states, we cannot read out k -states, since our detection can only record position distributions. We have instead simulated the expected position distribution, and compared it to experimental results.

4.2.3 Decoherence by projection

Similar to interferometer measurements (see 3.3), decoherence plays a significant role in quantum walks measurement. While the interferometer has two paths with a final interference event, the quantum walk has a very large

number of paths, which grows exponentially with the number of steps. Because of this, the walk is more sensitive to decoherence of spin states, while the transport error that is dominant for the interferometer is less important.

One cannot model the decoherence by a stochastic treatment of the accumulated phase; while feasible in the interferometer with its two paths, a walk consists of an exponential number of paths, many of which interfere making this approach very complicated. A more accessible way to describe decoherence is the density matrix formalism, because it can keep track of coherences between many separate states. We now introduce a projective measurement at each step with a probability p . Projection erases off-diagonal elements in the density matrix, and can be motivated as coherent coupling to an environment that is afterwards traced out [27]. The principle is familiar from "welcher-Weg-Information": if an outside system gains knowledge of a local state by entanglement with it, interference is suppressed. The following formula describes the stepwise evolution of the density matrix ρ using the projection operator $\mathbb{P}_i = |i\rangle\langle i|$ [22]:

$$\rho_{n+1} = (1 - p)\hat{S}\hat{C}\rho_n\hat{C}^\dagger\hat{S}^\dagger + p \sum_i \mathbb{P}_i \hat{S}\hat{C}\rho_n\hat{C}^\dagger\hat{S}^\dagger \mathbb{P}_i^\dagger. \quad (4.13)$$

Apart from p , the other degree of freedom in the model are the projection operators. Space projection as in $\mathbb{P}_i = \mathbb{I}_{|\uparrow\rangle, |\downarrow\rangle} \otimes |x_i\rangle\langle x_i|$ models spatial fluctuations, such as magnetic field gradients, laser speckle from stray light, etc., which produce an environment coupling that is spin-independent - i.e., the environment gains no information about atom spin.

The opposite are spin projection as in $\mathbb{P}_0 = |\uparrow\rangle\langle\uparrow| \otimes \mathbb{I}_{|x\rangle}$ and $\mathbb{P}_1 = |\downarrow\rangle\langle\downarrow| \otimes \mathbb{I}_{|x\rangle}$, which describes decoherence by a spin-dependent coupling to the environment that is position-agnostic. From the interferometer data, we know that there are no strong spatial gradients, nor spatial decoherence present in the setup (see 3.3.3), while spin dephasing affects the interferometer contrast measurably. We therefore elect to use a model with pure spin projection, which erases coherence between different spin states, but keeps off-site coherences of the same spin orientation intact.

How does this decoherence model relate to the dephasing model used for Ramsey and interferometry measurements? Dephasing means that contrast decays because of statistical fluctuations in the phase, leading to a characteristic polynomial decay of contrast over time. Spin echo pulses introduce a high pass filter for fluctuations and shift the behaviour to a gaussian curve [26]. These two curves describe dephasing, which is a stochastic loss of knowledge of a quantum phase. The projective decoherence model describes a physically different mechanism, namely decoherence by entanglement with an uncontrolled environment, removing the coherence. A Ramsey modelled with projective decoherence will have an exponential contrast decay, because for a constant rate of projection, the probability of avoiding projection for the entire lifetime of a superposition state goes down exponentially.

More generally, the projective decoherence model lets off-diagonal elements of the density matrix decay exponentially which is the same behaviour as modelled in the optical Bloch equations [24]. Unlike for dephasing, spin

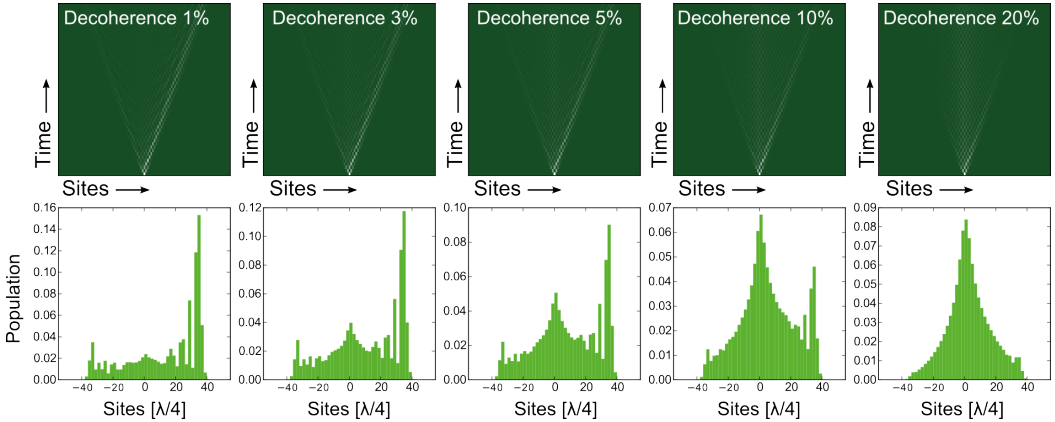


Figure 4.4: Simulated spreading and final distribution of a 50 step quantum walk including spin-projecting decoherence (see eq. 4.13). Decoherence is listed in relative coherence decay per step and really affects the distribution from 1% onwards by creating an exponential central peak. This is not a classical random walk yet (adding spatial decoherence will achieve it). The central peak means that the walk has lost the memory of its initial state and is no longer unitary.

echo doesn't exist in the projective decoherence model, as no spin flip will undo the entanglement with the environment that is removing the coherence from the system. Despite the differences of the projective model from the dephasing model, we shall see that it can model our experimental results for quantum walks just as well as the dephasing model has done for the interferometer data. Further work could investigate how the two models can be connected to describe quantum walks with dephasing.

4.2.4 Dephasing and paths

This subsection will present two known rephasing effects in the quantum walk. As mentioned before, this is disjunct from the projective decoherence model and serves not to extend it, but to explore how quantum walks show coherent behaviour beyond the normal coherence time by implementing spin echo.

I introduce a path-based formalism: a walk of an even step number n has 2^n paths and spreads over $2n + 1$ sites, numbered $0..2n$. The number of paths finally arriving at site k is the binomial factor $(n k/2)$ if k is even, or zero if k is odd. A path p is described by some binary string of length n like "0011", which encodes the state sequence $|\downarrow\rangle, |\downarrow\rangle, |\uparrow\rangle, |\uparrow\rangle$ as well as the movement sequence "-1,-1,+1,+1". The target site of this path is simply twice the sum over all digits, in this case 4, the central site.

The first mechanism reduces dephasing by staying in one spin state just as long as in the other. A static or slowly fluctuating detuning will let the path accumulate a phase for the time in one spin state and an equal but opposite phase for the time in the other spin state. The more balanced the path is, the greater the dephasing protection and the closer it ends to the central

site. The dephasing reduction factor $\chi(k)$ arising from this is:

$$\chi(p) = 1 - \left| \frac{k}{n} \right|, \quad (4.14)$$

which removes dephasing fully in the center of the distribution and barely at all in the wings.

The second mechanism reduces dephasing by staying in one spin state almost all the time. The corresponding paths accumulate a lot of phase from any detuning, but the paths they are interfering with in the end will have spent most of their time in the same spin state, rendering the accumulated phase common-mode. Two paths that arrive in the same final site k must have spent a fraction $\xi(k)$ of the walk duration in the same spin state:

$$\xi(k) = \left(\frac{k}{2n} \right)^2 + \left(\frac{2n-k}{2n} \right)^2, \quad (4.15)$$

and the resulting reduction factor in dephasing from a constant or slowly fluctuating detuning is $(1 - \xi(k))$, which removes dephasing fully in the outermost sites and not at all in the center.

If we combine the two mechanisms into a joint factor $\chi(k)(1 - \xi(k))$, we get a curve that is zero in the center and at the outermost sites and rises to a maximum value of 0.2 in between. Its mean value is approximately 0.1; the two path effects are together reducing dephasing by a factor ten

Introducing the alternating shift sign changes which effect is strongest where: now, the outermost sites are reached by paths that spend time 50:50 in both states, while the paths that spent the most time in one state arrive in the center. The overall statement about the mean rephasing is unaffected, explaining why quantum walks can give coherent distributions for durations that several times exceed T_2 .

4.2.5 Acceleration

To mimic a charged particle exposed to an electric field, we need the ability to apply a force to our atoms. We have implemented the force by accelerating the atoms trapped in the lattice using the conveyor belt technique (see 2.2.3). The effect is that of a constant electric field on an electron in a solid. It is well known that a constant field will cause the electron to undergo Bloch oscillations, in which the electron accelerates, shifting the k -states in the Brillouin zone by $\vec{k} = F/\hbar = -eE/\hbar$ until they reach the zone boundary and are returned to the opposite side [61]. Position and velocity of the atom can be calculated from the shape of the occupied band. For sinusoidal bands, both position and speed are also sinusoid functions; therefore, the acceleration makes the particle oscillate.

We activate the acceleration for discrete periods, applying the force F over duration t_F , which causes a linear spin-symmetric potential gradient along the lattice. Quantum states accumulate phase from the operation \hat{F} proportional to their site number $|x\rangle$:

$$\hat{F} = \sum_x e^{-i\phi x} |x\rangle \langle x| \otimes \mathbb{I}_{|\uparrow\rangle, |\downarrow\rangle} \quad \phi = \frac{m_{\text{Cs}} a \lambda t_F}{2\hbar}, \quad (4.16)$$

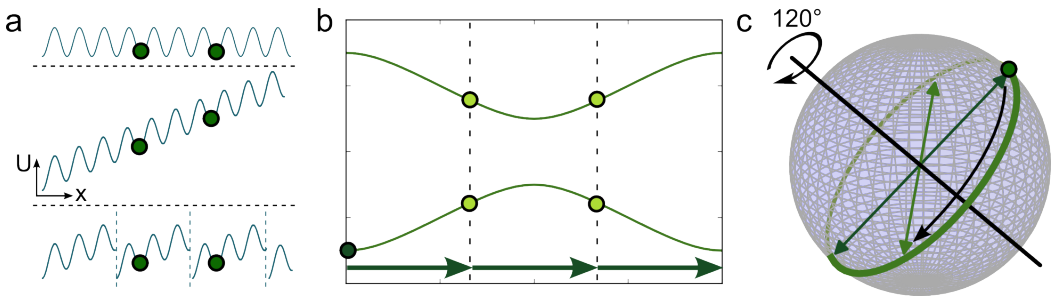


Figure 4.5: Three ways of thinking about acceleration on the walks, illustrated for $m = 3$. **a** The lattice in position space that becomes tilted by the superimposed linear potential. The conversion to quasi-energies causes the folding, equalizing every third site. The folding energy is not related to the well depth. **b** The momentum shift visualized in the band structure. The initial state occupies only the lower band before it is translated by $2\pi/3$. This causes a partial interband transition and moves part of the state to the higher band. After 3 steps, the state is back at the beginning. **c** The eigenstate circle on the Bloch sphere. The original eigenstates (dark green arrows) are replaced by new eigenstates after one shift (light green arrows), due to a rotation of the circle around its axis by 120° . The spin state (dark green point) is unchanged, but has a new mapping.

where m_{Cs} is the atomic mass and a the acceleration. The force is spin-independent and diagonal in position, i.e., it is assumed that no tunneling between lattice sites takes place.

The result of the force can be viewed in position or momentum space (see fig. 4.5). In position space, the lattice is superimposed with a linear potential gradient leading to a washboard shape that seems to have lost translation invariance. For certain values of the acceleration, the translation symmetry can be restored, however, by considering not energy but phase. We describe the phase accumulated by the parameter m as in $\phi = 2\pi/m$. If m is an integer, the phase accumulated per acceleration repeats every m sites, except for an irrelevant 2π difference (see fig. 4.5a). The washboard is thus folded into a sawtooth shape. This procedure resembles the transition from energy to quasienergy in a time periodic system using the Floquet theorem, but here it is caused not by temporal periodicity, but by the stroboscopic nature of our discrete operations [63].

The problem apparent is that no experiment can realize an "integer" force, which requires infinite precision. We use Heisenberg's uncertainty relation to show that for walks of finite size, only a finite precision in m is required. Let two walks of n steps differ in phase by $\delta\phi$, and each step take a time τ . The energy difference between the walks is then $\delta E = \hbar\delta\phi/\tau$. This can be resolved only if the duration of the measurement $n\cdot\tau$ exceeds $\hbar/\delta E$, leading to the criterion $n > 1/\delta\phi$. For under 100 steps, we only need a phase precision of 10 mrad, which the DDS setup provides. We continue with the assumption that m is an integer.

In momentum space, the acceleration \hat{F}_m causes a discrete translation by $\Delta k = -Ft_F/\hbar = 2\pi/m$. The localized atom fills the Brillouin zone evenly, and

in one application of \hat{F}_m , the entire Brillouin zone is shifted and the k states that leave the Brillouin zone are Bragg reflected to the opposite side. After m steps all states are where they started and have sampled the entire band. We assume for now that the state does not transition between bands. For large m (i.e., fine sampling) the spatial movement of a k state after m steps of duration τ is given by

$$\Delta x(k) = \int_0^{m\cdot\tau} v_g^\pm(k, t) dt = \sum_{i=1}^m v_g^\pm(k + i\frac{2\pi}{m}) \approx \int_{-\pi}^{\pi} v_g^\pm(\kappa) d\kappa = 0 \quad \forall k. \quad (4.17)$$

An integrated group velocity of zero means that the system has not spread - it is back at the origin, and since the sum is non-zero before m is reached, the walk is spreading out at first and then recontracting.

Small m require different treatment because the approximation of the sum as an integral is not tolerable. The integrated group velocity after m steps is precisely zero if m is even, because for every k sampled, there is also $k + \pi$ sampled, which has the same group velocity with opposite sign (see eq. 4.8). For odd m , the integrated group velocity is not precisely zero after m steps, but only after $2m$ steps, because it is then that every k gets its $k + \pi$ opposite for precise cancellation.

As the walk continues beyond m (or $2m$ steps), the distributions expands again and recontracts again, continuing indefinitely according to this naive calculation. These regular contractions are the hallmark of electric quantum walks.

Fig. 4.6 shows simulated spreadings using the electric walk operator $\hat{W} = \hat{S}\hat{F}_m\hat{C}$ for different m . The simulated walks perform the expected recontractions: instead of spreading with constant velocity, the electric walk spreads out, stagnates and refocuses towards the origin in a series of oscillations that resemble a plucked string. The period of these oscillations is m if m is an even number. Odd m show an almost-contraction after m steps and an ideal contraction after $2m$.

The faster oscillations like $m = 5$ do not show a clean pattern, contradicting the conclusion of eq. 4.17. The subjective quality of the oscillating pattern increases the larger m is. For the slowest oscillations (e.g. $m = 50$), another feature becomes discernible: the pure state $|\uparrow\rangle$ moves away towards the right; the peak gradually wanes, while the peak on the left that in a normal walk belongs to the $|\downarrow\rangle$ initial state waxes and eventually begins to move right, in time reaching the origin site. Despite the continuing oscillations, the walk is not confined: the size of the refocused distribution is growing and the walk ultimately expands to infinity (see the plot in fig. 4.6).

The expansion is unexpected from eq. 4.17, as is the poor quality of the faster oscillations. The reason are the previously neglected interband transitions. As the acceleration changes k , the mapping between spin states and bands changes (see fig. 4.5b). Now, as \hat{F} leaves the spin state unchanged, the momentum-translated state finds itself mapped to the other band with a fraction depending on the acceleration. Consider some initial state that is purely in one band: this state lies on the eigenstate disc (see fig. 4.5c); the effect of \hat{F}_m is to rotate this disc around its axis of symmetry by $2\pi/m$. The

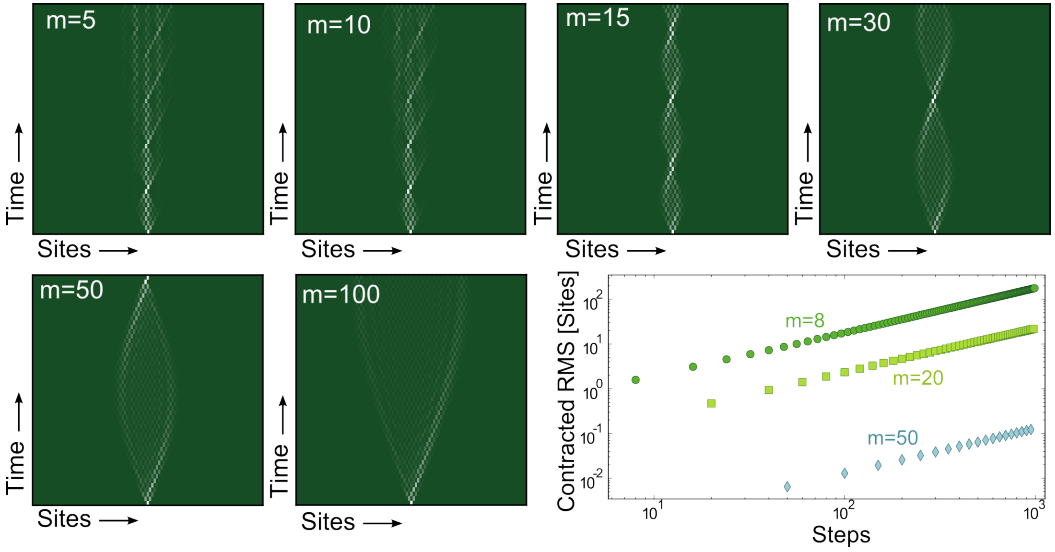


Figure 4.6: Simulated spreading and final distribution of a 50 step quantum walk for different acceleration levels m . Refocusings occur every m steps; odd m values have refocusings of alternatingly low and high quality. For low m , the contractions are disturbed by interband transitions. The graph shows the RMS at the contractions evolving for up to 1000 steps in the cases $m = 8$, $m = 20$ and $m = 50$. A linear increase with an m -dependent slope can be observed.

axis of symmetry in carthesian coordinates is:

$$\begin{pmatrix} x \\ y \\ z \end{pmatrix} = \begin{pmatrix} \cos \frac{\theta}{2} \\ -\cos \frac{\theta}{2} \\ \sin \frac{\theta}{2} \end{pmatrix}. \quad (4.18)$$

The band at the new momentum of the state has a different composition in $|\uparrow\rangle, |\downarrow\rangle$, but the actual state is unchanged - naturally, part of the state is now represented by the other band.

As the group velocities of the bands have opposite signs (see eq. 4.8), it is clear that there are components in the k space that will sample one sign of v_g from one band, then the same sign from the other and *not* cancel to zero after m steps - this is the mechanism behind the eventual escape to infinity and the degraded oscillations for small m .

It's important to note that the atom is not tunneling, but the simulated system is. Full tunneling, i.e., complete band transfer, occurs if the state is mapped entirely into the other band. Considering the eigenstate disc, this happens if the rotation angle is π , which happens for the acceleration $m = 2$. For quantum walks, $m = 2$ is therefore the strongest acceleration possible, as it shifts k by π , which is the maximum shift possible in a periodic system. All smaller m can be remapped to another, larger m , such as $m = 1$, which is equivalent to $m = \infty$, or no acceleration.

The $m = 2$ is special because $\Delta k = \pi$ transfers each k -state to a state on the

other band that has the same group velocity, including the sign (see eq. 4.8):

$$v_g^\pm(k) = -v_g^\pm(k + \pi) = v_g^\mp(k + \pi) \quad (4.19)$$

Remarkably, by achieving full tunneling, $m = 2$ doesn't affect the spreading at all.

The theoretical analysis of the electric walk can be taken a great deal further, leveraging the new symmetry cell of m sites to create a reduced Brillouin zone of $k \in [-\pi/m.. \pi/m]$ and applying Fourier transform and diagonalization to this new description. Detailed calculations and results can be found in [22]. The most interesting result is that apparent correlation between walks with odd m and their even counterpart of $2m$ is confirmed: the asymptotic dynamics can be shown to be identical. Furthermore, the maximum group velocity with acceleration is

$$|v_g^{\max}| = \begin{cases} \cos^m \theta/2 & \text{for even } m \\ \cos^{2m} \theta/2 & \text{for odd } m \end{cases}. \quad (4.20)$$

As long as m is rational, one can establish a new supercell of the lattice and proceed with normal symmetry assumptions, e.g., if $m = 117/118$, then $\phi = 236\pi/117$ and the new lattice period is obviously 117 sites, depending only on the numerator of m . If m is irrational, the new lattice becomes aperiodic - although, as mentioned above, a finite walk has finite resolution and cannot distinguish rational and irrational m . There is ongoing theoretical work in our group [64] exploring the situation, in particular a hypothesis that irrational m may lead to exponential localization of the walk.

4.3 Experiment

4.3.1 Procedure

The experimental procedure for quantum walks measurements is an adaptation of the one used for interferometer measurements. This is not surprising as the quantum walk is another arrangement of the same basic operation blocks: split, shift, accelerate. When these three are aligned, a walk can be executed. To measure the resulting position distribution, accurate single-site position detection is required.

Digital operations

Alignment begins by confirming that atoms survive the sequence with 90-100% probability; otherwise, lattice beam overlap and molassus cooling parameters are improved. Then, microwave π pulses are aligned using spectroscopy - resonance frequency and pulse duration need to be confirmed. Coherence times are checked, although good walks have been recorded even for $T_2 \approx 100 \mu\text{s}$, due to the inherent rephasing of the walk. Nevertheless, in order to improve coherence times in general, the lattice power is decreased to 6 mW per beam and the light shifts reduced in proportion.

The microwave pulse that implements the coin \hat{C}_B is in fact not a $\pi/2$ pulse, but a $3\pi/2$ pulse, because we have observed that the longer pulse is clearly superior in the experiment to the shorter. A possible explanation may be a spin echo effect arising from the added π rotation.

The shift operation works exactly as in the interferometer and needs to move the atom paths by $\pm\lambda/4$ coherently. For this, atoms are first cooled into the axial ground state; then, EOM voltage $V_{2\pi}$ and shift duration τ_s are tuned (see 2.3.3) to precisely achieve lattice overlap after each shift and prevent motional excitation. Compared to the interferometer, lower trap depths are used, and thus the correct shift duration has increased to 22-25 μs , from 16-19 μs in the interferometer. Once this is done, diamond interferometers of varying size can be performed to gauge the decay of contrast vs. steps, which gives some orientation for how many steps the walk may perform and arrive in decent shape.

Accelerated walks

When applying acceleration, there is no additional calibration to perform. The acceleration is generated by detuning one of the lattice beams using the RF output by the DDS (see 2.2.3), which can detune its signal with exceptional accuracy and stability[65] and will output precisely the frequencies demanded of it. Only one thing needs to be dealt with, and that is the movement of atoms due to the acceleration. In early measurements, atom were accelerated during the walk, then decelerated later and thus shifted by an appreciable amount, several tens of lattice sites for very long or strongly accelerate walks. In particular, the movement due to acceleration may be a non-integer number of sites - unless properly corrected, it would lead to aliasing effects on the quantum walks histogram, gravely damaging the resulting data. The distance moved has to be characterized by measuring the atom movement for the electric quantum walks sequence without shift or coin operations One can then determine the center of the resulting gaussian distribution. The value reached is subtracted from the positions in the second picture of the actual walk measurement.

For later measurements, I added a moveback feature to the MBED program. After performing the walk and decelerating the atom, the detuning is shifted to the other arm and a sequence with the same timing as the first but only consisting only of accelerations is performed to move the atom back to its original position. This is particularly useful for long accelerated walks, which otherwise may end up leaving the camera viewfield all together.

The phase accumulated from an acceleration a over a duration t_f is $\Phi_{acc} = \Delta x \cdot m_{Cs} \cdot a \cdot t_f / \hbar$. Using the velocity reached in the conveyor belt technique $v = \Delta f \cdot \lambda/2$, we find the detuning of the conveyor belt to be

$$\Delta f = \frac{16\pi\hbar}{m_{Cs}\lambda^2 m}, \quad (4.21)$$

where as before m_{Cs} is the atomic mass, while m is our desired acceleration parameter.

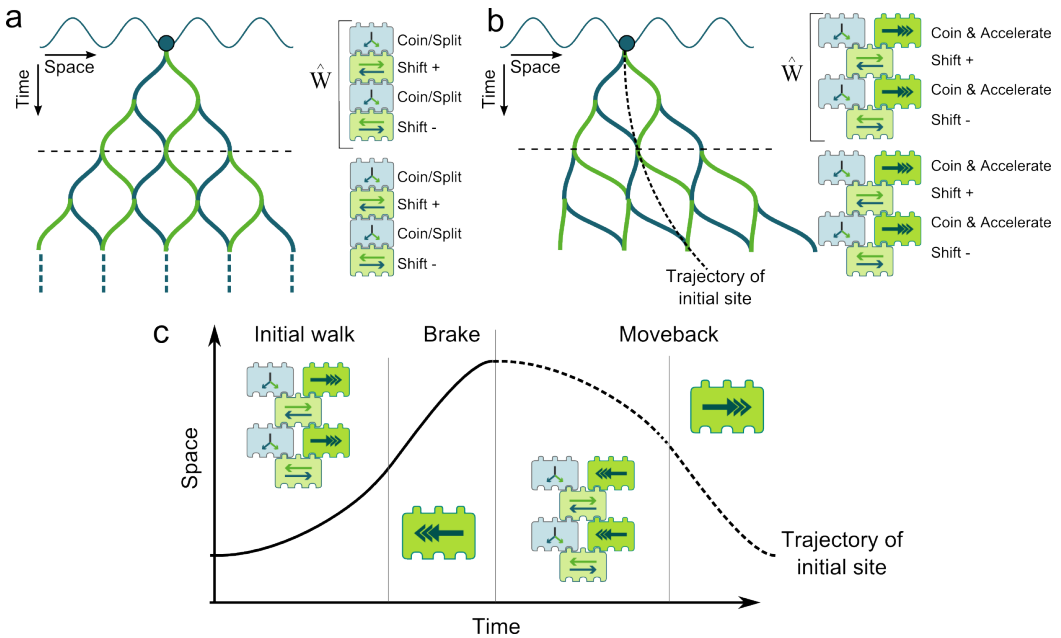


Figure 4.7: **a** Quantum paths and operation sequence for a normal quantum walk. The split operation that implements the coin \hat{C}_B is applied after every shift, leading to 2^n interfering paths. The walk can be extended to the desired length by repeating the basic four-operation sequence implementing the walk operator \hat{W} . **b** Electric quantum walk with acceleration. In every step, a constant acceleration is applied, leading to a parabolic trajectory of the lattice. To decrease decoherence, coin and acceleration are performed concurrently, but do not interact. **c** The trajectory of the initial site during and after the sequence: While the walk is going on, the site keeps accelerating every step. Afterwards, it is decelerated. In the later implemented moveback functionality, the sequence is performed a second time in reverse with all coins and shifts replaced by idle operations of equal length. As a result, the initial site is brought back to its original position, facilitating movement detection.

For our measurements, the usual detunings were on the order of 1-10 kHz and were applied using a linear ramp in the detuning, effectively stepping the frequency every 100 ns by a small amount. For a ramp duration of 15 μ s and the (for our measurements) moderate acceleration $m = 20$, we require a detuning of 1.6 kHz per step, or 10.67 Hz every 100 ns. The DDS frequency resolution is 0.09 Hz, allowing us to stay within 1% of the intended acceleration. Stronger accelerations are relatively more accurate because they have a larger frequency step every 100 ns.

Single-site detection

The output of a quantum walk measurement is a distribution of atom movements. We record it by determining the position of the atom before and after the walk with an accuracy of better than one lattice site. As we know

the number of shifts, we can establish the zone of possible movements of one atom and finding it inside in the second picture, calculate the relative distance by subtracting the position and rounding to the closest number of lattice sites. If two atoms approach so closely that their zones overlap, confusion of these two atoms may be possible and they are dropped from consideration. Dropping atoms because of their initial position should not skew the result.

Single-site detection is achieved by a numerical postanalysis of the images [66], fitting the distribution of CCD counts with a previously characterized line spread function (in the following LSF) of our imaging setup (see fig. 2.3). It succeeds if the noise level on the image is sufficiently low, which can be achieved by raising the exposure time to 600-1000 ms, from 200 ms normally. Furthermore, for the characterized LSF to match, the imaging objective needs to be at the right distance from the atoms down to some tens of microns. A translation stage is used to shift the camera objective minutely while imaging atoms in a lattice, until these appear completely in focus. To confirm that the detection is ready for measuring a walk, atoms are imaged twice without any operation blocks employed inbetween; their relative movement ought to remain below $\pm\lambda/4$. This is normally the case for 90-98% of all atoms, depending on the quality of the focal alignment and molassus parameters.

The long exposure required for correct position detection and the large inter-atom distances required to uniquely identify the movement of each atom force a reduction in atom loading. I reduce the loading duration of the MOT and change the magnetic field parameters for the transfer from the MOT to the lattice: while the MOT gradient is at 1.7 A (11 G/cm) to keep the cloud large, a linear ramp of the compensation fields drags the MOT cloud along the lattice during the transfer, loading atoms all over the viewfield instead of in one cluster. Nevertheless, a quantum walk measures on average 1-2 atoms per shot, with a sequence length of 3 s, due to long illumination times. We intend to improve this in the future by deliberately preparing an initial pattern of atoms [67].

4.3.2 Results from non-electric quantum walks

Quantum walks without acceleration are performed to characterize the capabilities of our experimental setup and to explore the effects that parameter changes and decoherence have on the outcome. They also serve to establish a reference for the following simulation.

The first measurement series is simply a balanced quantum walk performed for a different number of steps, up to 100 in this case. More steps are difficult to perform for several reasons: As the number of steps increases, the atom can spread over more and more sites and more atoms have to be sampled to construct a satisfying distribution. Furthermore, the risk of the atom leaving the camera viewfield increases.

The distribution resulting from a walk measurement should be evaluated both in its spreading (i.e., the RMS of the distribution) and its relative shape, which is most visible in the height and position of the dominant peaks. The

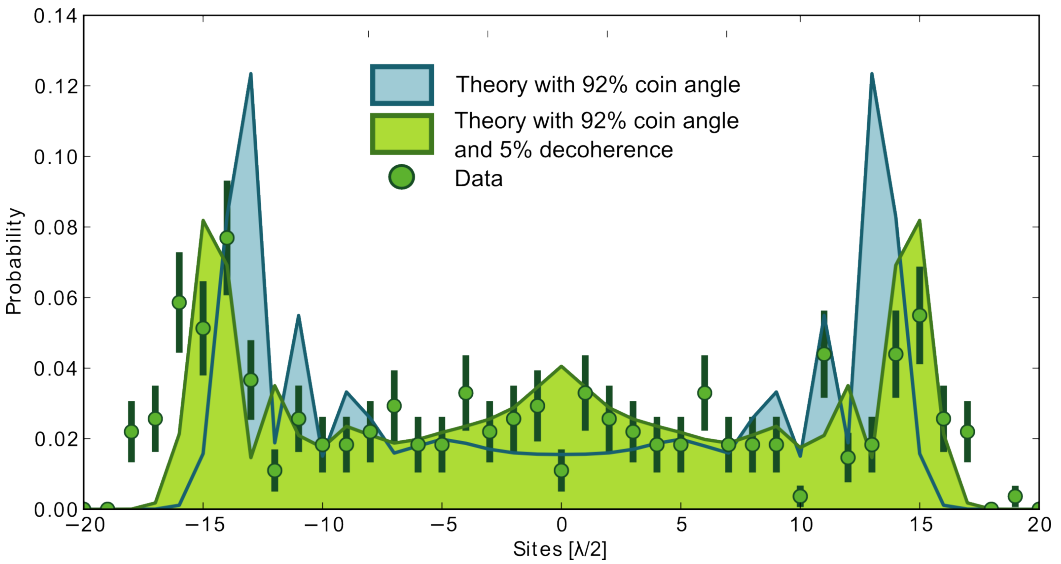


Figure 4.8: Position distribution of a quantum walk with 40 steps, starting with the balanced superposition $|\uparrow\rangle + i|\downarrow\rangle$. The two peaks are clearly visible, but at lower height and shifted outward from the ideal walk. A model adding decoherence and coin angle error fits much better, using 5% decoherence per step and 4% coin angle error.

normal quantum walks were started with a $|\uparrow\rangle + i|\downarrow\rangle$ superposition, producing a double-peaked distribution with a flat center in between.

Test case 40 steps

Figure 4.8 shows the results of a walk with 40 steps for first study: the peaks are reduced in height from the theoretical expectation and pushed slightly outward. In the center, a slight bump is apparent. By applying the decoherence model introduced in 4.2.3 and by fitting the decoherence rate to the data, we gain good agreement for peak height and the central hump, but not for the displacement of the side peaks. With the spin decoherence model, it is not possible to explain the discplacement, but by modifying the coin angle by a few percent, we achieve a good overall agreement. The coin angle changes the group velocities and can move the peaks quite freely.

The error bars on the experimental data are substantial, due to a combination of low datarate (forced by long exposures and reduced loading) and many lattice sites to fill. Sites in the center of the distribution only have a probability of 2-3%, meaning that at least 1000 atoms are required for reasonable statistics, while the large movement causes many atom images to be rejected due to insufficient distance between neighboring atoms. The shape rising up in the center could identify whether our choice of decoherence model is correct by showing either an exponential (for spin-only decoherence) or gaussian (for spin and spatial decoherence). Even so, from the data present that distinction is impossible to make. The suppressed population in the central site remains unexplained; nothing in the model accounts

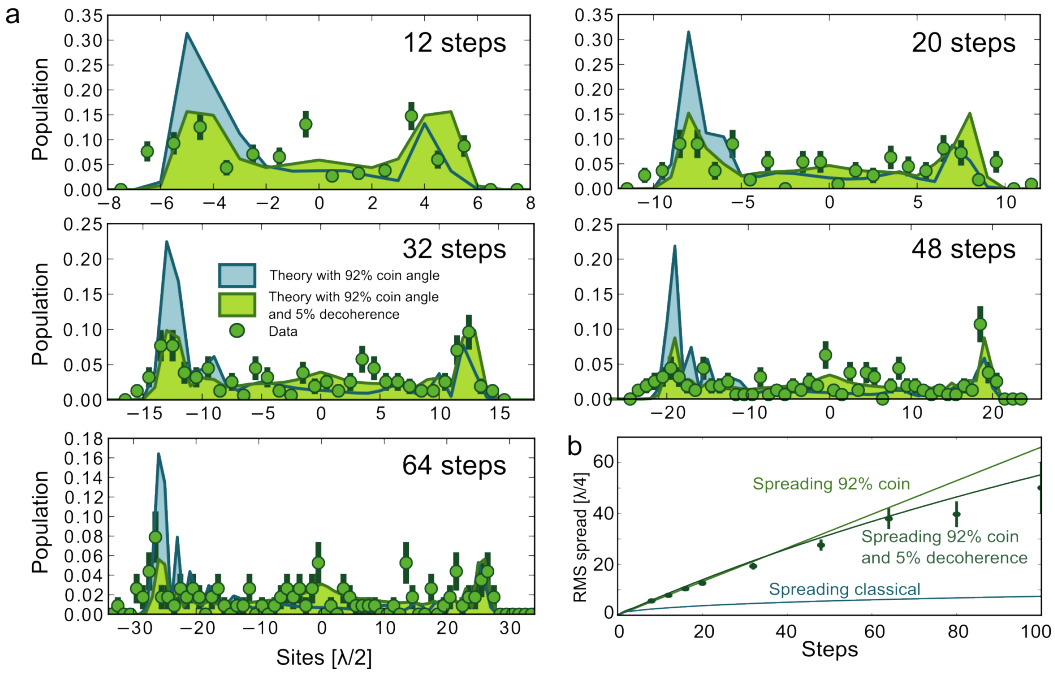


Figure 4.9: **a** Distribution for quantum walks for different number of steps from a balanced initial superposition. The experimental data is well fitted by assuming a coin angle error of 8% and a decoherence per step of 5%. The blue distribution shows the effect of coin angle without decoherence: the peak reaches the same position, but is higher and shows imbalance between left and right despite the balanced initial state - the partial rotation prefers one state over the other. **b** The RMS of the distribution initially follows a linear slope, then gradually falls off at around 40 steps. Spreading continues at superclassical speeds. The theoretical curve without decoherence is from eq. 4.12, the one with decoherence from numerical calculations.

for it, but the datum is significantly different from the others. Since it does not occur in any other datasets, I presume a statistical accident.

Two things about this dataset are noteworthy: the model fits well and the coherence is significant after 40 steps. In contrast, the decoherence rate of 5% per step would naively imply that after 40 steps, the walk should be fully decohered. To find out when it does decohere, we make the walk larger while observing the RMS evolution, which should eventually break away from the linear slope to approach the diffusive \sqrt{n} behaviour of the classical random walk. I have performed a series of walks up to 100 steps as mentioned above, which is the limit given by our camera field of view and data rate. The RMS evolution and some of the distributions are plotted in fig. 4.9. They show that the initial departure from the ballistic spreading occurs at around 40 steps, but purely diffusive spreading will likely not be reached until far above 200 steps. A significant advantage in spreading speed of the quantum walk over the classical random walk is demonstrated here. The actual distributions produced show a great deal of noise, but

preserve the correct spreading and to some degree, the two main peaks. In this set of measurements, the main peaks degrade already around 40 steps.

The decoherence rate is the same as in the previous walk, but the coin angle error has gone up to 8%, which is reaching the limit of the credible - precise alignment of the angle is challenging, but not to this degree. We should review what can affect the coin angle aside from the aligned pulse duration. First of all, the resonance frequency can move, which leads to phase accumulation and a reduction in effective coin angle. To stunt a pulse with a Rabi frequency of 50 kHz to this degree, a detuning of 15-20 kHz is required (going from $\Omega^2 = \Omega_0^2 + \delta^2$), which is not really plausible. Resonance is checked several times over the day, and fluctuations of this order of magnitude would be very apparent. Secondly, microwave power could fluctuate during the pulse, but calibration measurements of the electric signal during the pulse have shown excellent flatness. Also, Rabi oscillation measurements would suffer from this drastically, and while they are not part of the daily regime, they are performed occasionally and always show good coherence times.

In general, any constant defects would be detected by our calibration methods, hence, we should consider the possibility that during a long quantum walks sequences with many pulses, some parameters are drifting, either microwave power or possibly lattice phase. We do know that the EOM acts as a capacitor, accumulating charge on the millisecond scale which changes the birefringence slightly, particularly at a high voltage difference. Such an effect would occur during a longer sequence, skewing the lattice phase φ reached in the latter shifts of the sequence.

If the lattice phase for during a microwave pulse is no longer precisely 0 or 2π , the overlap between the connected spin states is diminished and the Rabi frequency decreases by the Franck-Condon factor [11]. Explaining our coin defect by this has two problems: the Franck-Condon factor can only *reduce* the coin angle (when the overlap between the wavefunctions is less than 100%) and the reduction is approximately parabolic, meaning that small changes in φ have a very small effect. Yet several walk measurements do in fact show a coin angle that is above the expected. Also, to reach a coin defect of 8% in this manner would required an angle defect of about 10° , quite strong. In conclusion, no explanation seems fully convincing; we should investigate further whether some other influence could mimic a coin angle defect.

Shorter walks for simulation

Quantum simulation can be performed with fewer than 40 steps taken, easing coherence and drift problems. Fig. 4.10 shows distributions for smaller step numbers and different initial states. The agreement between model and data is quite good, better in fact than for 40 steps, and the error of the data is much smaller. Similar measurements will provide the readout of our quantum simulator in the next section. For analyzing the coin angle error, the symmetric peaks of quantum walks starting from a superposition $|\uparrow\rangle + i|\downarrow\rangle$ can be useful because the height of the two peaks is a good indicator of coin angle. Note particularly the rather large deviation between

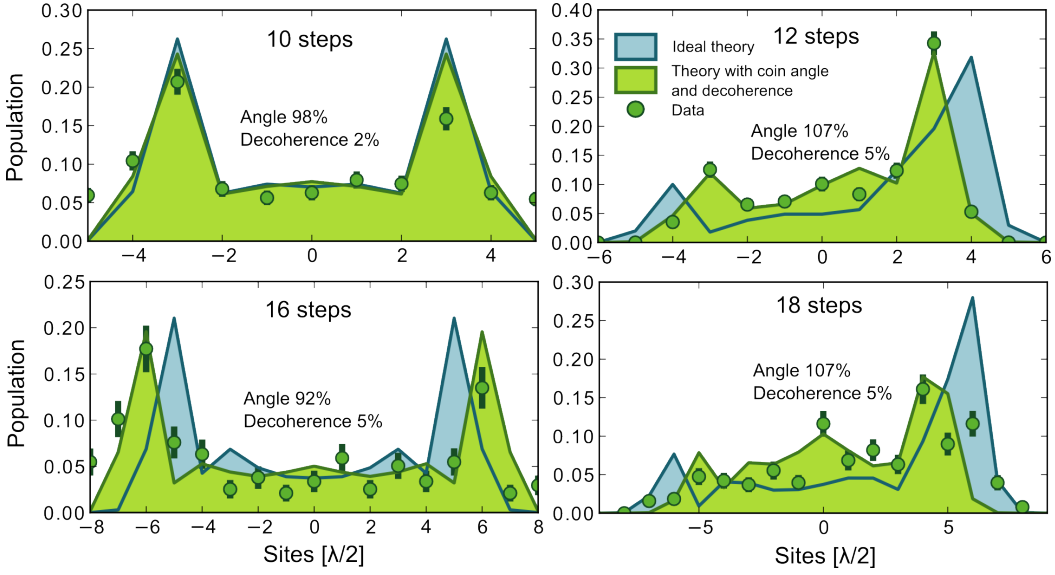


Figure 4.10: Position distributions measured for shorter quantum walks as might be employed in quantum simulation. Shown are the data, the ideal walk and the fitted walk with coin angle error and decoherence. Initial state and fitted parameters are listed in the plots. Observe particularly the disagreement in peak balance in the bottom-left: explaining the peak shift via coin angle error requires an imbalance in peak height that is not present in the data. This indicates that a more complex explanation may be necessary.

model and data in the 16 steps walk: the left peak should be larger for this coin angle error, but is virtually the same size as its counterpart. This gives some indication that a static coin error may not be the correct explanation for what we observe.

Scanning coin angle

Since we are interested in the coin angle, I have systematically measured walks for angles from π to 2π , transitioning from normal transport to full walk to stationary atom. Besides the distributions, I also compare the RMS spreading speed to the theory (see eq. 4.12). The results are shown in fig. 4.11 and are striking: The agreement between data and fitted distributions are good but the intended coin angles differ greatly from the spreading observed. Surprisingly, the difference depends on the angle: for $\theta = \pi$ and $\theta = 2\pi$, the intended and fitted angle match, but in between, the disagreement is up to 0.3 rad. No static misalignment of the pulse can achieve a θ -dependent error in θ .

The immediate thing to suspect is a fluctuation in microwave power over the pulse duration, but as stated before, we know from electronic calibration measurements that the power during a pulse is constant to better than 5%. It would also be strange that the difference aligns so well to our atomic Rabi frequency - an electronic defect has no reason to do so. I therefore

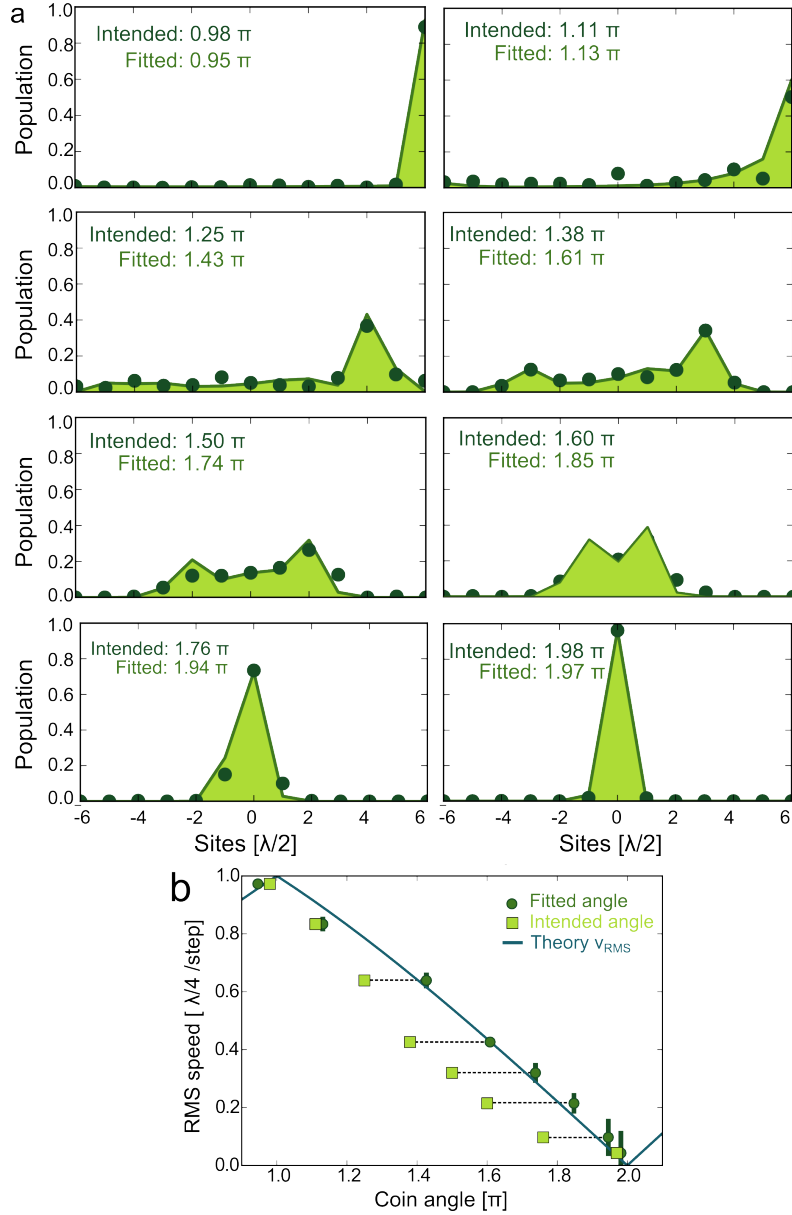


Figure 4.11: A series of walks performed with 12 steps and varying coin angle θ .
a The position distributions recorded, clearly showing the transition from transport to walk to stationary atom. The intended angles are plotted horizontally offset from the actual data; if we had managed to implement them, they would of course have resulted in a different RMS speed. Again, the agreement with the fitted model is high; decoherence is not even considered here. **b** The RMS speed as a metric of group velocity. Squares show the nominal coin angle, points the fit result. The difference is extreme and unexpected, particularly since it depends strongly on coin angle (i.e., pulse duration). The agreement of the fitted values with theory is good, giving them credibility.

believe that some atomic, likely coherent, phenomenon is the reason for the fault. Capacitative effects in the EOM are not completely out of the picture, as they would precisely have the most impact for $\theta \approx 3\pi/2$, when multipath interference is dominant. Future work on quantum walks will need to uncover the reason behind this behaviour, or at least eliminate it.

Despite the deviations in coin angle, the good agreement with theory is positive. In comparison to prior quantum walks measurements [10, 56] the coherence time is improved about four-fold. The main experimental difference from the previous experiments is that axial ground state cooling is now a standard procedure, reducing transport excitation and enhancing microwave pulse fidelity.

Furthermore, several changes were made in the setup, namely a new EOM, improved focus size and lower dipole trap depth. Also, the servo circuit for power stabilization of the lattice was changed and the main Ti:Sa laser was readjusted in-depth, including the lock electronics, to reduce power noise. These improvements did not in the end increase the coherence times T_2 and T_{2*} , as the positive changes in trap depth and power stability were offset by the new EOM, which contains a longer crystal with negative impact on the beam polarization. The most likely explanation is then the introduction of the axial ground state cooling, which improves both shift and pulse performance.

4.3.3 Results from electric quantum walks

Bloch oscillations are performed by a particle in a Bloch band under the influence of a linear potential, e.g., an electron in a crystal under an electric field. In the following, we will observe them using the quantum walk as a simulator. The numerical calculations in 4.2.5 show us the results of these Bloch oscillations in position space: periodic contractions of the walk distribution to the original single site, occurring every m steps, where m is the length of the acceleration-imposed supercell of the lattice, i.e., the acceleration causes $2\pi/m$ phase between neighboring lattice sites. The reason for this refocusing is that the system eventually has sampled the whole Brillouin zone, leading to zero total group velocity after m accelerations.

Due to increasing interband transitions, contractions degrade for $m < 6$. The most striking case occurs for $m = 2$: the entire population tunnels to the other band at every step, erasing the effect of acceleration on group velocity. The resulting position distribution is the same as for a non-electric quantum walk, as well as the case of $m = 1$ (shifts k by exactly 2π).

Both contractions and tunneling will be demonstrated in the following. Finally, measurements for an irrational m will be presented.

Contractions

I begin with $m = 8$, expected to show contractions for 8 and 16 steps. The distributions observed for 4,8,12 and 16 steps can be seen in fig. 4.12a. As with previous measurements, the data is fitted well by the model, resulting

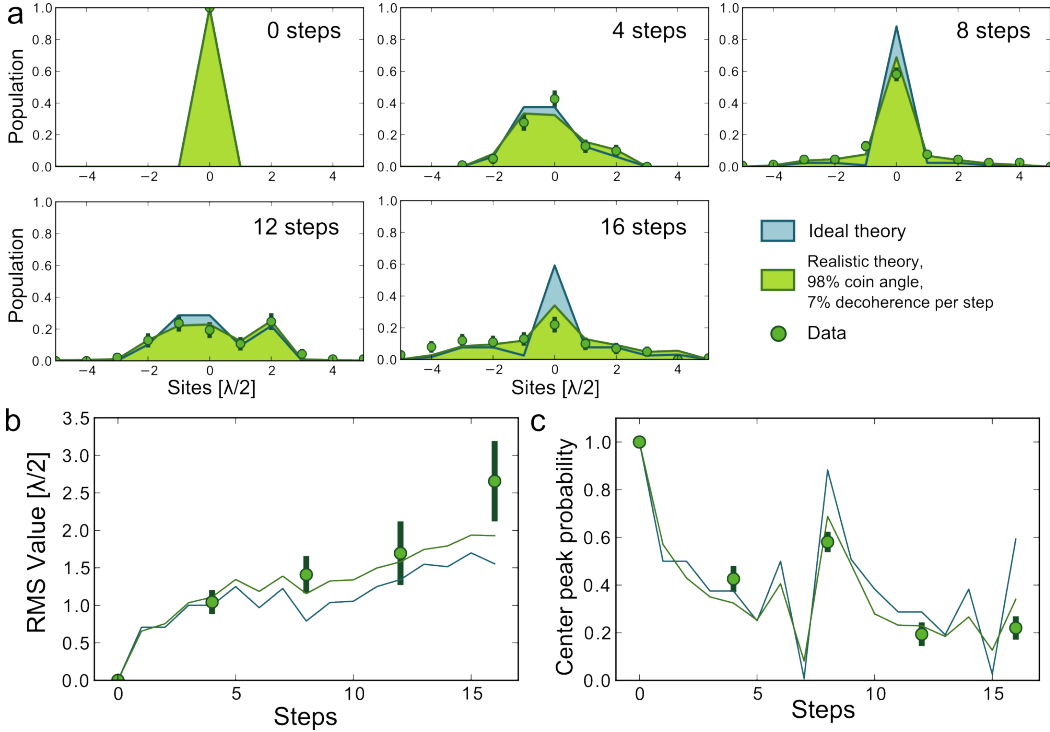


Figure 4.12: A series of walks performed with $m = 8$ acceleration and varying step number. **a** The position distributions, showing data, ideal theory and a fitted theory using 2% coin angle error and 7% decoherence per step. Two contractions occur, at 8 and 16 steps. Both contractions are visible in the data. The second contraction is degraded even in ideal theory due to the low value of m . **b** The RMS value as a measure of spreading: for the contractions, it is not a very informative metric, since it emphasizes the outer parts of the distribution and noise can wash out the events in the center. **c** The summed probability in the interval [-1,1] shows contraction at 8 steps. The contraction at 16 steps is degraded by decoherence; even the ideal contraction is significantly reduced from the first.

in a coin error of 2% and a decoherence per step of 7%. Due to the low step number, we do not observe significant decoherence up to 12 steps.

The key dsitribution is the one after eight steps, which clearly shows that the walk has contracted back from the spreading it had after four steps, placing 60% of all atoms on the original site. A walk without acceleration would have no central peak and very little population in the original site. By comparing the two theory curves in the eight step picture, one can also see that the height of the neigboring bars at -1,+1 is very dependent on decoherence, illustrating that the loss of coherence is degrading the refocusing.

The second contraction at sixteen steps is much weaker, degraded by decoherence and dropping below the model: the central peak is not in good agreement with theory. Such strong decoherence after a mere 16 steps is unusual, but the contraction remains visible.

To quantize the contractions, we need a figure of merit. The intuitive

choice is RMS, which is shown in fig. 4.12b both for data and the two theory curves. Due to its quadratic term, the RMS strongly emphasizes the outer wings of the distribution and when that distribution is noisy, it obscures the events in the center almost completely. Even the ideal theory RMS does not perform a strong dip at eight steps, in contrast to the crystal clear effect in the position distribution. The dip in the RMS virtually disappears when decoherence is applied, again contrasting the distribution. The RMS can be used to gauge when the walk departs from our model, but is not sensitive to the contractions we desire to observe.

I instead plot the height of the central peak for quantitative comparison between experiment and theory. This figure is somewhat arbitrary, but at least sufficiently sensitive to the contractions both in theoretical and experimental data (see fig. 4.12c). The comparison shows that experimental values show the correct modulation as expected with decoherence, barely contracting at 16 steps. The ideal contraction is also reduced significantly from the one at 8 steps, due to interband tunneling.

I have also taken a sequence of measurements for $m = 20$ with walks of up to 40 steps. The resulting position distributions are shown in fig. 4.13a and while the fits shows a higher decoherence rate, we nevertheless observe the expected behaviour for up to 30 steps. The key distributions are the three for 18, 20 and 22 steps, which show onset, apex, and ending of the contraction. After 26 steps, the distribution remains flat and does not contract a second time. Because of the acceleration, the distribution's support is still in the interval $[-6, 6]$, whereas a non-electric walk would have much larger extent after 40 steps (compare fig. 4.8).

As before, the RMS values are most useful for judging when the walk departs from the theory (see fig. 4.13b), but not for spotting contractions, as decoherence will completely erase their signature. The probability for the central site is a more sensitive figure of merit and shows good agreement with the theory for all measurements, with a very clear bump at 20 steps (see fig. 4.13c). Only the datum at 40 steps is significantly away from the model. In comparison with the $m = 8$ measurement, the second contraction is in theory much stronger, reaching far above 90%. All the same, the decoherence strongly suppresses the second contraction event.

These two measurement series demonstrate the contractions resulting from Bloch oscillations; a second contraction can even be seen for $m = 8$. The simulation of Bloch oscillations has been successful. The precision of the results can be improved and the issues with coin angle should be investigated further when we proceed to simulations of more complicated phenomena.

Interband tunneling

For strong accelerations, the contractions degrade as interband transitions increase. In particular, as mentioned above, $m = 2$ causes a 100% interband transition and fully inverts the band populations. Surprisingly, this causes the group velocity to remain constant, and the expected distribution is that of a non-electric walk. We also compare $m = 1$, which shifts all states by a full Brillouin zone, and is thus also equivalent to a non-electric walk.

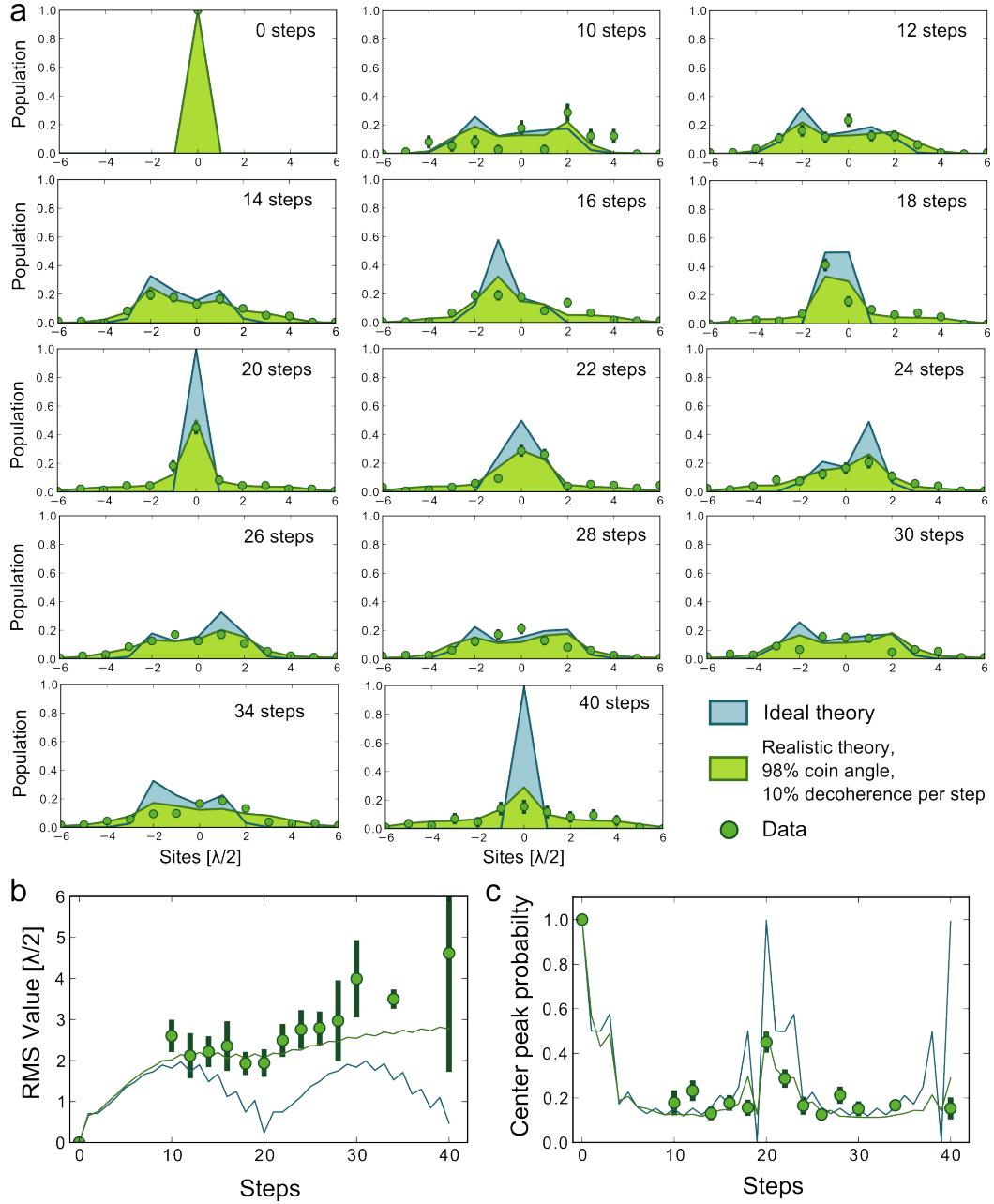


Figure 4.13: A series of walks performed with $m = 20$ acceleration and varying step number. **a** The position distributions, showing data, ideal theory and a fitted theory using 2% coin angle error and 10% decoherence per step. Two contractions occur, at 20 and 40 steps. The first contraction is well reproduced, the second one fails. **b** Decoherence erases the contractions' signature from the RMS). **c** The population in the central peak shows the first contraction cleanly, the second one not at all.

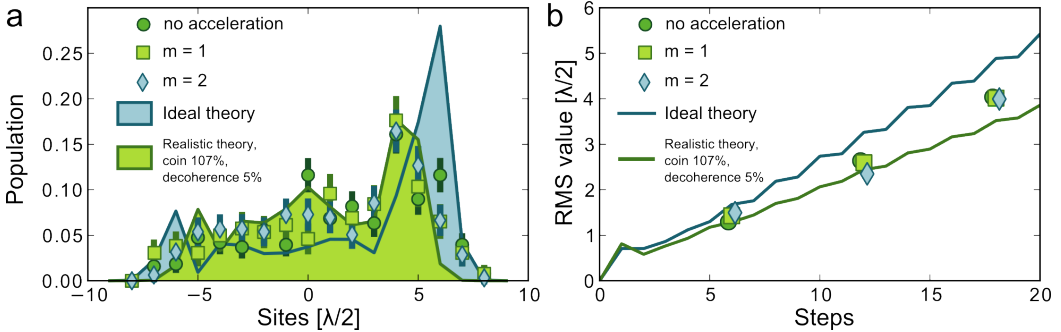


Figure 4.14: **a** The position distribution for 18 steps performed with no acceleration, $m = 1$ and $m = 2$. The theory curves are fully identical for all three cases due to interband tunneling and Bragg reflections and the data confirms the equivalence. The fit returns 107% coin angle and 5% decoherence per step. **b** The RMS value, shown for 6, 12 and 18 steps for all three accelerations. The equivalence hold and the RMS evolves as expected. Data markers are slightly offset horizontally to keep all three visible at all times.

I have measured the walks with $m = 1, m = 2$ and no acceleration for 6, 12 and 18 steps. Fig. 4.14a shows the three distributions arising at 18 steps. There is only one theory curve for the three datasets together and we have also used a common fit, resulting in a coin angle of 107% and a decoherence rate of 5% per step. The three datasets overlap closely, and in particular all reproduce the large peak on the right side. Their largest disagreement is in the central site, which may be due to fluctuating decoherence rates between the measurements.

The RMS spreading of the walks for all three cases is shown in fig. 4.14b. The three datasets coincide with each other and the theory curves: interband tunneling ensures that an acceleration by several dozen g has no effect.

Observing contractions and interband tunneling marks a successful quantum simulation, and demonstrates for the first time the ability to realize Bloch oscillations in quantum walks with considerable control over the states of the walk.

Irrational m

The theoretical treatment of irrational m is completely different from that of rational m ; the main reason is the absence of translational or temporal periodicity. This renders most of our theory developed so far inappropriate; new phenomena arising for irrational m are still under investigation [64]. The most interesting hypothesis so far is that the walk may be localized, akin to Wannier-Stark localization [68].

Numerical simulations show that the electric quantum walk's ideal spreading stays small for thousands of steps, but oscillates with approximately 7 steps period (compare fig. 4.15a for the first 50 steps). Time-averaging the distribution to cancel the oscillation shows an exponential distribution. I have performed electric quantum walks with 4, 6, 8, 10 and 12 steps. Three

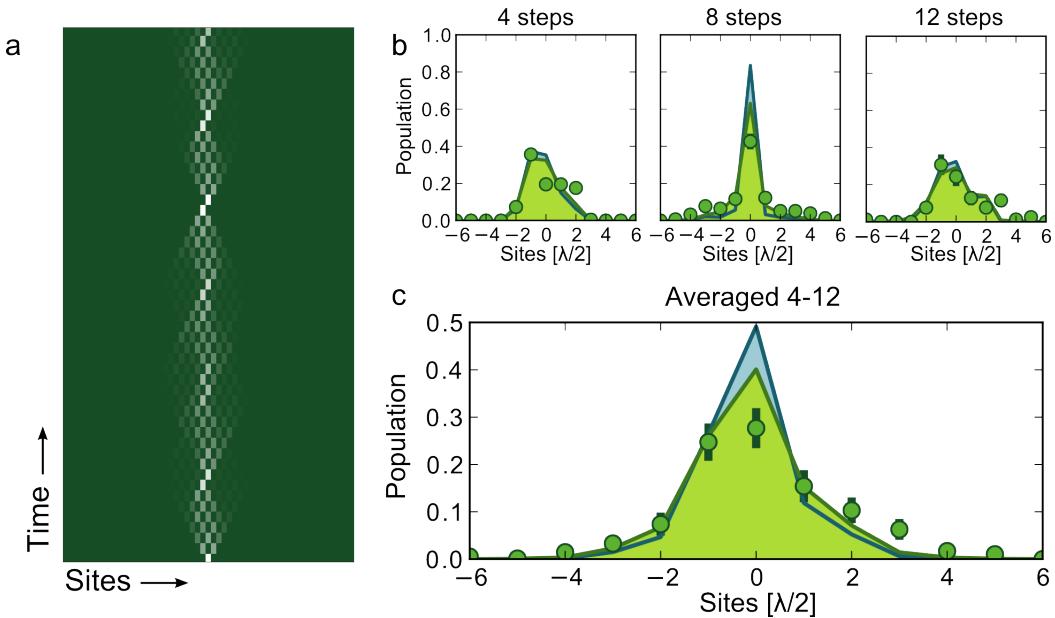


Figure 4.15: Quantum walks for an aperiodic lattice with $m = (1 + \sqrt{5})/2$. **a** Evolution of the position distribution. The distribution oscillates with a period of approximately 7 steps and does not diverge. **b** Measured distributions for 4, 8 and 12 steps, with ideal theory and theory incorporating 10% decoherence per step and 2% coin angle defect. The agreement between model and data is not as good as in other measurements; in particular, the almost-contraction at 8 steps is reduced. **c** Average of distribution for 4, 6, 8, 10 and 12 steps, both data and theory. The data recovers the general shape, but falls significantly under the theory with decoherence.

of the distributions as well as the average of all five are plotted in fig. 4.15. The oscillation is reproduced, albeit with a degraded central peak at 8 steps. The averaged distribution falls significantly below the theory curve on the central site, but is matching the other points well and clearly centered at zero. Certainly the walk behaviour is matching our simulations, reproducing the oscillation and the overall exponential distribution. Further work needs to be done on the theory of irrational m .

4.4 Proposal for k -state selection

All phenomena we have measured in this chapter can be understood and calculated elegantly in momentum space. Our research is therefore hindered by the inability to access individual k -states, and relies instead on a smoothly-filled Brillouin zone and detection in position space. I will present in the following a proposal for the experimental preparation and detection of k states in our system.

The atoms in our experiment are localized to one site, and the Brillouin zone is fully occupied. Since we cool the atoms to the axial ground state,

they are all in the lowest Bloch band. Our normal lattice is so deep that tunneling between sites is suppressed (about 1.6 MHz or 800 recoil energies), so the bands are virtually flat. If we lower our lattice to a few recoil energies, tunneling becomes possible and band curvature becomes noticeable; in particular, the first excited band is approaching the ground state band at the zone boundary.

The core idea is that by accelerating the lattice strongly, we can shift part of the ground state band population into higher bands by Landau-Zener tunneling [69]. Momentum states pushed over the edge of the Brillouin zone tunnel to the higher band if the acceleration applied exceeds the critical acceleration a_c [70]. To visualize Landau-Zener tunneling, imagine the k -states accelerated up the sinusoidal slope and shooting across the band gap onto the higher band (see fig. 4.16a). The concept sequence for k -selection is as follows:

1. Prepare atoms in ground state $|\downarrow, n = 0\rangle$.
2. Lower lattice depth to $U \approx E_R$ adiabatically.
3. Accelerate with several times a_c .
4. A large part of the Brillouin zone is shifted to $|n = 1\rangle$.
5. Decelerate and ramp the lattice back up.
6. Use a microwave sideband transition $|\downarrow, n\rangle \rightarrow |\uparrow, n - 1\rangle$.
7. Use push-out to remove all $|\uparrow\rangle$.

This procedure leaves a thin slice in k -state by removing all other momenta - it is a selection scheme, not a cooling scheme. Detection is possible by adiabatically turning off one of the lattice beams, and switching to a running wave trap for some amount of time. An atom will travel from its initial position depending on its group velocity $v_g(k)$, allowing reconstruction of k .

Several issues must be addressed:

- What is the adiabatic lattice depth ramp $U(t)$?
- What is the critical acceleration a_c and how many atoms tunnel?
- How fast do atoms travel in the running wave for detection?

The bandgap $E_G(U)$ is the key figure for the first two questions. The Schrödinger equation of a particle in a sinusoidal potential can be transformed to Mathieu's equation [71], which has periodic solutions only for certain energy and momentum combinations E, k , with jumps of E at every integer k that gives the band gaps - using a rescaling of E in units of E_R and k in units of π/d . The bandgaps can be calculated using Mathieu's characteristic exponent $a_r(k, E)$:

$$E_G(n) = a_r \left(n + \epsilon, \frac{U}{4E_R} \right) - a_r \left(n - \epsilon, \frac{U}{4E_R} \right), \quad (4.22)$$

where ϵ is an infinitesimal number and $n \in \mathbb{N}$ is the number of the bandgap, corresponding to $k = n \cdot \pi/d$. For deep lattices ($U > 16E_R$), the harmonic

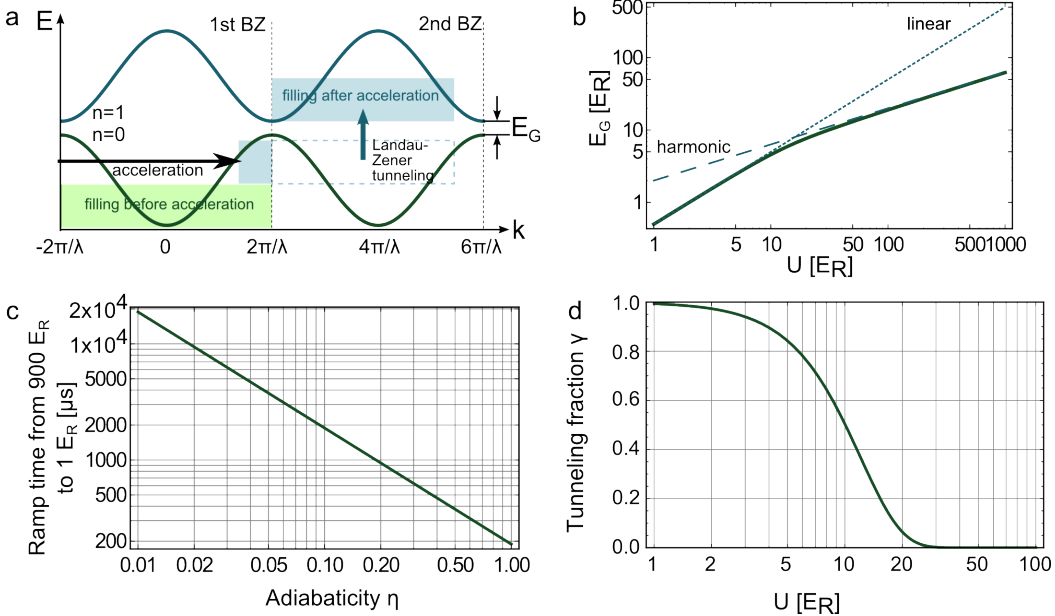


Figure 4.16: **a** The scheme for k -selection: the key is to shift most k -states into a higher band using a strong acceleration to achieve Landau-Zener tunneling. Microwave sideband techniques can be used to eliminate these atoms [30]. The key property for this is the bandgap E_G . **b** The band gap from Mathieu’s characteristic exponent a_r (full line), with the harmonic approximation (dashed) and the linear approximation (dotted). The regime change is at sixteen recoil energies. **c** The time required to lower to 1 E_R from the original 900 E_R for different adiabaticity goals. **d** The tunneling fraction as a function of lattice depth for the acceleration resulting from $\beta = 0.9$ as discussed in the text.

approximation is valid and $E_G^{(1)} \approx 2\sqrt{U \cdot E_R}$. For shallow lattices, the better approximation is the free particle and $E_G^{(2)} \approx U/2$ (see fig. 4.16b).

With the band gap established, we can turn towards adiabaticity. Adiabatic lowering means reducing the trap depth so slowly that the all states remain in their original band. The relative rate of lowering τ must be low enough that the band gap energy is always resolved according to the Heisenberg uncertainty relation:

$$\left| \frac{U}{\dot{U}} \right| = \tau \quad \tau \cdot E_G \geq \hbar \quad \Rightarrow \quad \frac{\hbar}{\tau E_G} = \eta \ll 1, \quad (4.23)$$

using a number η to specify our adiabaticity goal. Using the two different regimes of the bandgap, we find:

$$U(t)^{(1)} = \frac{4\hbar^2}{\eta^2 E_R t^2} \quad U(t)^{(2)} = \frac{2\hbar}{\eta t}. \quad (4.24)$$

We can now calculate the time required for lowering to be on the order of milliseconds depending on the adiabaticity goal (see fig. 4.16c).

Once in the weak lattice, we must accelerate the atoms strongly to induce Landau-Zener tunneling. There are two conditions on the acceleration: it

should shift the desired fraction of the states β into the next Brillouin zone, and it should let these states tunnel into the next higher band instead of being Bragg-reflected. The first condition is easy to evaluate: β is related to our previous acceleration number m by $\beta = m^{-1}$ and the formula for the required acceleration is

$$a(\beta, \tau) = \frac{8\pi\hbar\beta}{m_{Cs}\lambda\tau}, \quad (4.25)$$

where τ is the acceleration duration. The second condition is that the states pushed over the edge of the Brillouin zone must tunnel, so the tunneling fraction γ must be near-unity. It depends exponentially on the critical acceleration a_c [70]:

$$\gamma(a, U) = \exp\left(-\frac{a_c}{a}\right), \quad a_c = \frac{\lambda E_G^2}{8\hbar^2}. \quad (4.26)$$

We can calculate now whether the timescales and accelerations required are feasible. I set $\beta = 0.9$ to select a 10% slice of the Brillouin zone. The acceleration required is the higher the shorter the acceleration time is, allowing a larger tunneling fraction. However, the DDS shifts the frequency every 10 ns, so I set $\tau = 10 \mu s$ to guarantee a sufficient granularity of the acceleration ramp. The acceleration is then 624 m/s^2 , achieved by a lattice detuning of 14 kHz. The tunneling fraction depending on U can be calculated (see fig. 4.16d) and is sufficiently high for $U \leq 1E_R$. How long it takes to lower the lattice the trap from $900 E_R$ to the required $1 E_R$ depends on the demanded adiabaticity (see fig. 4.16c).

Lowering the lattice depth can be done by decreasing one or both lattice beams. If we ramp down both beams, each beam must be decreased by a factor 30, for a final power of $200 \mu W$. But atom temperature is a problem: at time scales of over $100 \mu s$, atoms begin to escape radially when ramping down the lattice so strongly. The alternative is to ramp down one lattice beam, creating a running wave trap with a weak lattice overlaid. To reach $1 E_R$, the lattice beam must ramp down by a factor thousand, for a final power of $6 \mu W$, which is more challenging to control but achievable.

Finally, can we detect the selected k states? The traditional method is a time-of-flight measurement: ramp the lattice down to activate tunneling, then let the atom propagate naturally for a controlled time. The maximum group velocity at $U = 1 E_R$ is about 5 sites per ms, and the RMS speed 3.5 sites per ms. Letting the atom expand for 20 ms will cause enough motion to detect the k -state clearly.

To summarize, the scheme for k -state selection seems fully viable. The main difficulties will be the control of the laser beam power at very low values and the reduced data rate from discarding 90% of the atoms, but performing quantum walks with selected k -states makes it worthwhile.

5 Conclusion

Recapitulation

As I opined in the introduction, a great deal of quantum mechanics is about phase. The same applies to my thesis, which features two large measurement campaigns revolving around coherent interference phenomena. The first of the two is the single atom interferometer. In an interferometer, phase is at its most accessible, since between the two arms of the interferometer there is only one phase and it is directly converted into population for easy measurement. In this regard, atom interferometers are much simpler than quantum walks and allow detailed interpretation of mechanism in quality as well as quantity. Our interferometer measurement were thoroughly analyzed regarding both phase and contrast. Comparing phase accumulation in different geometries allowed me to separate spin-symmetric and -antisymmetric potential gradients existing in our setup. The major discovery was that due to loading atoms away from the focus of the dipole trap, there is a spin-symmetric potential gradient of some 300 Hz per lattice site, whose magnitude could be determined with an accuracy of 0.3%. Furthermore, I was able to show that no significant spin-antisymmetric gradients exist, which would be extremely significant due to their ability to detune microwave operations depending on position. Analyzing the decay of contrast showed that our usual dephasing can be suppressed by repeated spin echo to raise the spin coherence time above 2 ms. The real limiting factor is actually the fidelity of π pulses, which are required at every transport step due to our EOM's technical limitations. While there are in principle several more mechanisms for contrast decay, these two make up the lion's share, and it does not seem possible from our data to properly quantize the others.

One advantage of doing interferometry trapped in a lattice is the ability to insert hold times. We have performed such measurements and found them to confirm our previous findings about potential gradients and decoherence existing in our system. Their best use, however, is to keep the atom stationary for some position-dependent effect, which our experiment was not currently equipped to apply. Instead, we demonstrated that external effects could be measured satisfactorily by applying a global acceleration to the atom and recording the phase in agreement with theoretical calculations. The interferometer data offer a wealth of information about our setup and our operations, but they also show what our experiment is not: it is not a purpose-built precision interferometry experiment, due to the compromises made to obtain high flexibility and single atom control. Using our experimental stability and comparatively low atom rate, we cannot reach relative accuracies of 10^{-9} as truly precision-focused experiments have before [39]. The point is rather to explore new physics: the electric quantum walks are an example of this.

The entire field of experimental quantum walks is quite young and is only beginning to progress from implementing walks to using them for specific purposes. Our electric walks are our first foray into using walks as a measurement tool and the research was therefore markedly different from the interferometry work. Instead of an in-depth analysis of a well-understood system, we tried to demonstrate for the first time what models were telling us to expect and were successful. Comparing theory and experiment in position space, we demonstrated Bloch oscillations both by contraction of the quantum walk and by interband tunneling which equalizes the effect of several very different accelerations. We also found that our simple two-parameter model of the quantum walk produces very satisfactory agreement with the data; compared to the first quantum walks measurements in 2009, our understanding of walks has become much deeper, concerning their distribution, spreading and decoherence. Nevertheless, one issue is still unconcluded, namely the coin angle error.

Apart from the proposed k -state selection, our intention is to advance the experiment by employing several new technologies. This is motivated by the experience of the electric quantum walk measurements: the actual measurements for electric walks are no different from the normal walks that were possible already in 2009, but the capability for applying well-controlled accelerations was missing, which became available once we installed the DDS setup. In other words, the progress in research was technology-driven. To repeat this progress, we already have two major technology upgrades in the pipeline: interferometric polarization synthesis and Raman cooling.

Interferometric polarization synthesis

Interferometric polarization synthesis (IPS) is a preliminary name for a new technique that our group has developed, used to modulate polarization with a Mach-Zehnder interferometer and two optical phase-locked loops (OPLL). The technique was evaluated in the thesis of Anna Hambitzer[72] in our laboratory. The basic idea is to split a laser beam with a polarizing beam splitter, then couple the two orthogonal polarizations through one AOM each and combine them again on another PBS. The output of this interferometer is composition of the two arms in orthogonal polarizations, frequency-shifted by the AOM. By setting up two beat notes with a common reference laser beam, we can put each of the two polarizations individually into phase-lock by monitoring the phase of the beat note and adjusting the signal frequency going to the AOM to stabilize it. The two overlapping OPLLs have already been shown to work, with a relative RMS phase stability of 1° and a crosstalk between the two loops of -68 dB, which should be sufficient for trapping atoms without exciting them [72].

By phase ramping the reference signal for the OPLL, the optical phase will be smoothly ramped. Of course, our state-dependent lattice depends on two *circular* polarizations that can be phase-shifted with regard to each other, but a waveplate can translate linear into circular polarization. Once in place, IPS will fully replace our EOM, eliminating problems such as polarization gradients due to crystal mounting from our setup. Moreover, in-

stead of being limited to a single lattice site shift, IPS can perform infinite shifting, similar to the conveyor belt technique, by detuning one chirality vs. the other. Using IPS, we expect to extend our shift ability to distances of over $100 \mu\text{m}$ as well dropping the requirement for alternating π pulses for long-distance shifting. This will allow for drastically larger interferometers, increasing phase sensitivity by orders of magnitude. It will also allow mapping our lattice gradients for several $100 \mu\text{m}$ around the imaging position, characterizing our optical trap almost to perfection. For the quantum walks, a coin is necessary every step anyway, but we nevertheless expect to benefit strongly from removing the EOM and its polarization effects. New challenges may arise, as the two chiralities are now represented by fully independent laser beams with individual beam profiles. These need to be smoothly overlapped at the atoms to a very high degree, or the atoms will experience major differential lights shifts with resulting dephasing. Also, the power stabilization of the two beams needs to be on a high level for the same reason. The setup has so far not been tested with atoms, but this will happen in the very near future.

Raman ground state cooling

The second upgrade, with possibly even larger significance, is Raman cooling into the motional ground state., which will allow atom-atom interactions by s-wave scattering. If two atoms are brought onto the same site, they are currently too hot and their probability densities too dilute to sense each other, but in the motional ground state, this will change and they will accumulate significant interaction phases from cohabitation of the same lattice site[73]. Using such interaction phases, one can realize quantum logic gates[8, 41]. The only requirement is to actually reach the ground state; for this, Raman cooling with two phase-locked lasers is a standard technique. The concept is very similar to our microwave sideband cooling: a spin state transition is driven on the cooling sideband with continuous repumping (compare 2.3.2). But the difference is in how this transition is performed: two diode lasers are detuned from the resonance by some hundreds of GHz, while stabilized at a frequency difference between them of 9.1 GHz. The two lasers can now drive a two-photon transition in a λ -scheme from $|F = 4, m_F = 4\rangle$ to $|F = 3, m_F = 3\rangle$; because of the large momentum of laser photons, if the two lasers come from different directions, the motional sidebands can be driven. In principle, the position displacement that allowed the transition in microwave cooling is replaced here by momentum displacement. However, some subtleties exist and two phase-locked lasers are not enough - although they have been build and have already demonstrated a non-sideband spin transition on our atoms[73]. The problem is that for our optical trap strength radial to the lattice axis, the recoil from the spontaneous decay in the cooling cycle will heat our atoms too much - the trap needs to be stiffened. We have set up an additional laser beam to provide additional confinement, in this case a blue-detuned donut beam. The ring crosssection of this beam is generated with a spiral phase plate, and the shape allows surrounding the existing attractive trap with this repulsive cas-

ing. The beam has also been tested independently and demonstrated an 8x increase in trap frequency, sufficient for Raman cooling [73]. What remains is to finish integrating the lasers into the setup and test them together - the project was paused for the duration of the quantum walk measurement and will likely be recommenced after the IPS setup is installed.

Our group has recently published a proposal for using atom-atom interactions in quantum walks to demonstrate a novel molecular binding mechanism [74]. If two adjacent atoms undergo a walk with on-site interaction between them, this can lead to binding between the atoms due to their mutual effect on phase accumulation, causing the atoms to exit the walk in correlated positions. This is particularly remarkable as there is no binding energy holding the atom pairs together. Furthermore, the walks of the two atoms can be recast as the walk of a molecule. The missing keystone to put this to the test in our laboratory is atom-atom interaction; ground-state cooling will provide it.

Scalability

Looking a little further into the future, we need to consider the scalability of our system. Ignoring near-term technical obstacles, there are still limits to how many atoms can be controlled and interrogated and how many operations can be performed on them. This will consider the setup of our successor experiment, which is employing a state-dependent 3D optical lattice with one layer of atoms imaged from the top.

The first thing to consider is detection: an EMCCD camera is usually limited to 512x512 pixels. Improved imaging optics reaching a numerical aperture larger than 0.8 have been developed in our group, vastly improving the sharpness of each atom. Nevertheless, for reliable separation of a large group of atoms, an atom-atom separation of at least 2 px seems absolutely necessary, making for about 200x200 atoms that could be maximally detected at once. The duration required for the image is reduced significantly if the point-spread functions of the atoms do not overlap and no fitting is required; basically, for each isolated site the algorithm only has to distinguish between one atom or no atom. This seems possible for about 100 ms imaging time. The lattice filling when loading from a MOT is at most 50%, and this can only be reached after loading the MOT for some time, probably a few 100 ms. The realistic maximum data rate of such a system then seems to be about 30,000 atoms per second, of course assuming significant technical progress. Adding additional cameras to extend the viewfield would be challenging but possible by dividing the fluorescence light into several tiles after the main imaging objective, then mapping each tile onto its own camera.

Besides detection, coherence time is another important limitation. It makes sense to think not of absolute times but of how many operations can be performed coherently. The now-dominant lattice effects can be suppressed strongly by improving the polarization state (which the IPS setup promises) and reducing thermal motion in the wells (by Raman cooling to the radial ground state). Magnetic field fluctuations, which are now limiting us to $T_2 \approx 500 \mu\text{s}$ will then come to the fore. They can also be suppressed signifi-

cantly by a feed-forward cancellation that is aligned using a spectroscopic signal from the atoms[75] and we may be able to improve T_2 up to maybe 50 ms. If we reach such a coherence time, the scattering rate arising from the lattice laser becomes significant. It is currently on the order of one in 100 ms and since we are fixed to the magic wavelength, this can only be improved by decreasing the lattice depth, to which the scattering is proportional. The downside is that the duration of excitation-free shifting will increase, since it is inversely proportional to trap frequency[10]. Because of the square-root relation between trap frequency and trap depth, it is actually advantageous to have a deep lattice and shift faster, allowing overall more shifts in the coherence time. It seems at the moment that the IPS setup may be able to perform a shift in 5 μ s, but no faster without replacing the AOMs by something else.

Of course, operations like microwave pulses do not become faster in deeper lattices. They can anyway be sped up by using Raman lasers for population transfer, which in a powerful beam with good focus can reach Rabi frequencies in the tens of MHz range[76]. So, while we can now perform maybe 200 coherent operations and retain a visible signal, with the above improvements, some tens of thousand can be ultimately expected.

Bibliography

- [1] G. Santarelli, P. Laurent, P. Lemonde, A. Clairon, A. Mann, S. Chang, A. Luiten, and C. Salomon, "Quantum projection noise in an atomic fountain: A high stability cesium frequency standard," *Physical Review Letters*, vol. 82, no. 23, pp. 4619–4622, 1999.
- [2] P. R. Berman, ed., *Atom Interferometry*. New York: Academic Press, 1997.
- [3] A. D. Cronin, J. Schmiedmayer, and D. E. Pritchard, "Optics and interferometry with atoms and molecules," *Rev. Mod. Phys.*, vol. 81, no. 3, pp. 1051–1129, 2009.
- [4] M. Riebe, K. Kim, P. Schindler, T. Monz, P. Schmidt, T. Körber, W. Hänsel, H. Häffner, C. Roos, and R. Blatt, "Process tomography of ion trap quantum gates," *Physical review letters*, vol. 97, no. 22, p. 220407, 2006.
- [5] D. Leibfried, B. DeMarco, V. Meyer, M. Rowe, A. Ben-Kish, J. Britton, W. Itano, B. Jelenković, C. Langer, T. Rosenband, *et al.*, "Trapped-ion quantum simulator: experimental application to nonlinear interferometers," *Physical review letters*, vol. 89, no. 24, p. 247901, 2002.
- [6] S. Lloyd, "Universal quantum simulators," *Science*, vol. 273, p. 1073, 1996.
- [7] I. Bloch, "Quantum coherence and entanglement with ultracold atoms in optical lattices," *Nature*, vol. 453, no. 7198, pp. 1016–1022, 2008.
- [8] D. Jaksch, H. J. Briegel, J. I. Cirac, C. W. Gardiner, and P. Zoller, "Entanglement of atoms via cold controlled collisions," *Phys. Rev. Lett.*, vol. 82, no. 9, pp. 1975–1978, 1999.
- [9] J. Kempe, "Quantum random walks: an introductory overview," *Contemporary Physics*, vol. 44, no. 4, pp. 307–327, 2003.
- [10] M. Karski, *State-selective transport of single neutral atoms*. PhD thesis, University of Bonn, 2010.
- [11] L. Förster, *Microwave control of atomic motion in a spin-dependent optical lattice*. PhD thesis, University of Bonn, 2010.
- [12] N. Spethmann, *Single impurity atoms immersed in an ultracold gas*. PhD thesis, University of Bonn, 2012.
- [13] W. Alt, "An objective lens for efficient fluorescence detection of single atoms," *Optik - International Journal for Light and Electron Optics*, vol. 113, no. 3, 2002.

- [14] L. Li and T. Speed, "Parametric deconvolution of positive spike trains," *Annals of Statistics*, vol. 28, no. 5, 2000.
- [15] K. Lewenberg, "A method for the solution of certain problems in least squares," *Quarterly Applied Mathematics*, vol. 2, 1944.
- [16] Andor Technology PLC., "Andor system performance booklet dv887 issue 1 rev 0 11/02."
- [17] A. Alberti *et al.*, "Methods for single-atom imaging in optical lattices with single-site resolution," *to be submitted*.
- [18] J. Zopes, "Einzelplatz-Detektion im optischen Gitter unterhalb des Beugungslimits," 2012. Bachelor thesis.
- [19] D. Döring, "Ein Experiment zum zustandsabhängigen Transport einzelner Atome," Master's thesis, University of Bonn, 2007.
- [20] R. Pizzo, "Re: Temperature dependence of half-wave voltage." E-Mail on 2012-03-09 with Conoptics Inc.
- [21] D. Schrader, S. Kuhr, W. Alt, M. Müller, V. Gomer, and D. Meschede, "An optical conveyor belt for single neutral atoms," *Appl. Phys. B*, vol. 73, p. 819, 2001.
- [22] M. Genske, "Electric quantum walks with individual atoms," Master's thesis, University of Bonn, 2012.
- [23] N. F. Ramsey, "A new molecular beam resonance method," *Phys. Rev.*, vol. 76, no. 7, pp. 996–996, 1949.
- [24] L. Allen and J. Eberly, *Optical resonance and two-level atoms*. Dover publications, 2987.
- [25] L. Vandersypen and I. Chuang, "Nmr techniques for quantum control and computation," *Reviews of modern physics*, vol. 76, no. 4, p. 1037, 2005.
- [26] S. Kuhr, W. Alt, D. Schrader, I. Dotsenko, Y. Miroshnychenko, A. Rauschenbeutel, and D. Meschede, "Analysis of dephasing mechanisms in a standing-wave dipole trap," *Phys. Rev. A*, vol. 72, no. 2, p. 023406, 2005.
- [27] M. Schlosshauer, *Decoherence and the quantum-to-classical transition*. Springer, 2008.
- [28] J. Bylander, S. Gustavsson, F. Yan, F. Yoshihara, K. Harrabi, G. Fitch, D. Cory, Y. Nakamura, J. Tsai, and W. Oliver, "Noise spectroscopy through dynamical decoupling with a superconducting flux qubit," *Nature Physics*, vol. 7, no. 7, pp. 565–570, 2011.
- [29] D. Nisperuza, G. Botero, and A. Bastidas, "Precise alignment of a longitudinal Pockels cell for Q-switch operation Nd:YAG laser," *Revista Cubana de Física*, vol. 27, no. 1, 2010.

- [30] L. Förster, M. Karski, J. M. Choi, A. Steffen, W. Alt, D. Meschede, A. Widera, E. Montano, J. H. Lee, W. Rakreungdet, J. H. Lee, W. Rakreungdet, and P. S. Jessen, "Microwave control of atomic motion in optical lattices," *Phys. Rev. Lett.*, vol. 103, no. 23, p. 233001, 2009.
- [31] A. Yariv and P. Yeh, *Optical waves in crystals*, vol. 5. Wiley New York, 1984.
- [32] M. Orszag, *Quantum optics*. Springer, 2000.
- [33] O. Carnal and J. Mlynek, "Young's double-slit experiment with atoms: A simple atom interferometer," *Physical review letters*, vol. 66, no. 21, pp. 2689–2692, 1991.
- [34] D. Keith, C. Ekstrom, Q. Turchette, and D. Pritchard, "An interferometer for atoms," *Physical review letters*, vol. 66, no. 21, pp. 2693–2696, 1991.
- [35] M. Arndt, O. Nairz, J. Vos-Andreae, C. Keller, G. van der Zouw, and A. Zeilinger, "Wave-particle duality of C 60 molecules," *Nature*, vol. 401, no. 6754, pp. 680–682, 1999.
- [36] J. Hudson, D. Kara, I. Smallman, B. Sauer, M. Tarbutt, and E. Hinds, "Improved measurement of the shape of the electron," *Nature*, vol. 473, no. 7348, pp. 493–496, 2011.
- [37] C. Bordé, "Atomic interferometry with internal state labelling," *Physics letters A*, vol. 140, no. 1, pp. 10–12, 1989.
- [38] P. Cladé, S. Guellati-Khélifa, F. Nez, and F. Biraben, "Large Momentum Beam Splitter Using Bloch Oscillations," *Physical review letters*, vol. 102, no. 24, p. 240402, 2009.
- [39] A. Peters, K. Chung, and S. Chu, "Measurement of gravitational acceleration by dropping atoms," *Nature*, vol. 400, no. 6747, pp. 849–852, 1999.
- [40] J. B. Fixler, G. T. Foster, J. M. McGuirk, and M. A. Kasevich, "Atom Interferometer Measurement of the Newtonian Constant of Gravity," *Science*, vol. 315, pp. 74–, Jan. 2007.
- [41] O. Mandel, M. Greiner, A. Widera, T. Rom, T. W. Hänsch, and I. Bloch, "Controlled collisions for multi-particle entanglement of optically trapped atoms," *Nature*, vol. 425, no. 6961, pp. 937–940, 2003.
- [42] P. Böhi, M. Riedel, J. Hoffrogge, J. Reichel, T. Hänsch, and P. Treutlein, "Coherent manipulation of Bose-Einstein condensates with state-dependent microwave potentials on an atom chip," *Nature Physics*, vol. 5, no. 8, pp. 592–597, 2009.
- [43] H. P. Myers, *Introductory solid-state physics*. CRC Press, 2002.

- [44] C. Cohen-Tannoudji, J. Dupont-Roc, and G. Grynberg, *Atom-photon interactions: Basic processes and applications*. Wiley-VCH, 2004.
- [45] D. Allan, "Time and frequency (time-domain) characterization, estimation, and prediction of precision clocks and oscillators," *Ultrasonics, Ferroelectrics and Frequency Control, IEEE Transactions on*, vol. 34, no. 6, pp. 647–654, 1987.
- [46] H. Müller, A. Peters, and S. Chu, "A precision measurement of the gravitational redshift by the interference of matter waves," *Nature*, vol. 463, no. 7283, pp. 926–929, 2010.
- [47] T. C. Briles, D. C. Yost, A. Cingöz, J. Ye, and T. R. Schibli, "Simple piezoelectric-actuated mirror with 180 kHz servo bandwidth," *Opt. Express*, vol. 18, no. 10, pp. 9739–9746, 2010.
- [48] L. Lovász, "Random walks on graphs: A survey," *Combinatorics, Paul erdos is eighty*, vol. 2, no. 1, pp. 1–46, 1993.
- [49] A. Ghoniem and F. Sherman, "Grid-free simulation of diffusion using random walk methods," *Journal of Computational Physics*, vol. 61, no. 1, pp. 1–37, 1985.
- [50] H. Berg, *Random walks in biology*. Princeton University Press, 1993.
- [51] P. Révész, *Random walk in random and non-random environments*. World Scientific Publishing Company Incorporated, 2005.
- [52] Y. Aharonov, L. Davidovich, and N. Zagury, "Quantum random walks," *Physical Review A*, vol. 48, no. 2, pp. 1687–1690, 1993.
- [53] N. Shenvi, J. Kempe, and K. Whaley, "Quantum random-walk search algorithm," *Physical Review A*, vol. 67, no. 5, p. 052307, 2003.
- [54] M. Mohseni, P. Rebentrost, S. Lloyd, and A. Aspuru-Guzik, "Environment-assisted quantum walks in photosynthetic energy transfer," *The Journal of chemical physics*, vol. 129, no. 17, p. 174106, 2008.
- [55] A. Childs, "Universal computation by quantum walk," *Physical review letters*, vol. 102, no. 18, p. 180501, 2009.
- [56] M. Karski, L. Förster, J. M. Choi, A. Steffen, W. Alt, D. Meschede, and A. Widera, "Quantum walk in position space with single optically trapped atoms," *Science*, vol. 325, no. 5937, pp. 174–177, 2009.
- [57] A. Schreiber, K. Cassemiro, V. Potoček, A. Gábris, P. Mosley, E. Andersson, I. Jex, and C. Silberhorn, "Photons walking the line: A quantum walk with adjustable coin operations," *Physical review letters*, vol. 104, no. 5, p. 50502, 2010.

- [58] A. Peruzzo, M. Lobino, J. Matthews, N. Matsuda, A. Politi, K. Poulios, X. Zhou, Y. Lahini, N. Ismail, K. Wörhoff, Y. Bromberg, Y. Silberberg, M. Thompson, and J. O'Brien, "Quantum walks of correlated photons," *Science*, vol. 329, no. 5998, pp. 1500-1503, 2010.
- [59] H. Schmitz, R. Matjeschk, C. Schneider, J. Glueckert, M. Enderlein, T. Huber, and T. Schaetz, "Quantum walk of a trapped ion in phase space," *Physical review letters*, vol. 103, no. 9, p. 90504, 2009.
- [60] A. Schreiber, A. Gábris, P. Rohde, K. Laiho, M. Štefaňák, V. Potoček, C. Hamilton, I. Jex, and C. Silberhorn, "A 2d quantum walk simulation of two-particle dynamics," *science*, vol. 336, no. 6077, pp. 55-58, 2012.
- [61] F. Bloch, "Über die Quantenmechanik der Elektronen in Kristallgittern," *Zeitschrift für Physik A Hadrons and Nuclei*, vol. 52, pp. 555-600, 1929. 10.1007/BF01339455.
- [62] W. Demtröder, *Experimentalphysik 3: Atome, Moleküle und Festkörper*. Springer, 2000.
- [63] T. Kitagawa, M. Rudner, E. Berg, and E. Demler, "Exploring topological phases with quantum walks," *Physical Review A*, vol. 82, no. 3, p. 033429, 2010.
- [64] M. Genske, W. Alt, A. Steffen, A. H. Werner, R. F. Werner, D. Meschede, and A. Alberti, "Electric quantum walks with individual atoms," *Phys. Rev. Lett.*, vol. 110, p. 190601, May 2013.
- [65] "AD9954: 400 MSPS, 14-Bit, 1.8 V CMOS, Direct Digital Synthesizer Data Sheet, Analog Devices Inc.," 05 2009. Data sheet rev. B.
- [66] M. Karski, L. Förster, J. M. Choi, W. Alt, A. Widera, and D. Meschede, "Nearest-neighbor detection of atoms in a 1D optical lattice by fluorescence imaging," *Phys. Rev. Lett.*, vol. 102, no. 5, p. 053001, 2009.
- [67] M. Karski, L. Förster, J. M. Choi, A. Steffen, N. Belmehri, W. Alt, D. Meschede, and A. Widera, "Imprinting patterns of neutral atoms in an optical lattice using magnetic resonance techniques," *New J. Phys.*, vol. 12, p. 065027, 2010.
- [68] M. Glück, A. R Kolovsky, and H. Korsch, "Wannier-stark resonances in optical and semiconductor superlattices," *Physics reports*, vol. 366, no. 3, pp. 103-182, 2002.
- [69] Q. Niu, X. Zhao, G. Georgakis, and M. Raizen, "Atomic landau-zener tunneling and wannier-stark ladders in optical potentials," *Physical review letters*, vol. 76, no. 24, pp. 4504-4507, 1996.
- [70] A. Alberti, *Coherent transport in driven optical lattices and applications to force measurements*. PhD thesis, University of Florence, 2010.

- [71] P. Louis, E. Ostrovskaya, C. Savage, and Y. Kivshar, "Bose-einstein condensates in optical lattices: Band-gap structure and solitons," *Physical Review A*, vol. 67, no. 1, p. 013602, 2003.
- [72] A. Hambitzer, "Direct synthesis of light polarization for state-dependent transport," Master's thesis, University of Bonn, 2012.
- [73] S. Hild, "Resolved raman sideband cooling in a doughnut-shaped optical trap," Master's thesis, University of Bonn, 2011.
- [74] A. Ahlbrecht, A. Alberti, D. Meschede, V. Scholz, A. Werner, and R. Werner, "Molecular binding in interacting quantum walks," *New Journal of Physics*, vol. 14, no. 7, p. 073050, 2012.
- [75] A. Smith, B. Anderson, S. Chaudhury, and P. Jessen, "Three-axis measurement and cancellation of background magnetic fields to less than $50 \mu\text{g}$ in a cold atom experiment," *Journal of Physics B: Atomic, Molecular and Optical Physics*, vol. 44, no. 20, p. 205002, 2011.
- [76] P. Hemmer, A. Turukhin, M. Shahriar, and J. Musser, "Raman-excited spin coherences in nitrogen-vacancy color centers in diamond," *Optics letters*, vol. 26, no. 6, pp. 361–363, 2001.